Utrecht University

Earth Sciences
Earth Structure & Dynamics

Lab induced earthquakes in the rotary shear apparatus

J.J.P. Beunen

August 31, 2023

Utrecht University

Supervisors:

Dr André Niemeijer
MSc Rens Elbertsen

1 Abstract

Frequency-magnitude distributions play a crucial role in the creation of probability seismic hazard analysis, providing valuable insights into the likelihood and severity of seismic events. However, obtaining accurate distributions can be challenging due to the scarcity of data, especially when the recurrence time between earthquakes is long. Because of this limitation, it is often difficult to correctly chose between the two main types of different frequency-magnitude distribution models: the Characteristic and the Gutenberg-Richter earthquake model.

To address this gap in knowledge, the focus of this thesis revolves around conducting a series of friction experiments using a rotary shear apparatus. The experiments aim to replicate natural conditions by utilizing analogs for materials found in the Earth's crust. The materials that are used in this thesis include glass beads of varying sizes, gypsum, and salt (KCl and NaCl).

Throughout the experiments, a constant normal stress was maintained, while parameters like grain size and velocity were systematically varied to observe their impact on the number and size of shear stress drops and acoustic emissions. The results obtained from this thesis demonstrate that the frequency-magnitude distribution differs for each material tested and even differs for the same materials sheared under the same conditions.

The experiments revealed that the slowest velocities correspond in the majority of the experiments to the largest recorded shear stress drops. Further, the different materials are not necessarily described by the two main frequency magnitude distributions: the Gutenberg-Richter or the characteristic earthquake model. The b-value of the Gutenberg-Richter earthquake model, which describes the proportion of small to large earthquakes, seems to be susceptible for changes in velocity. For glass beads, which are analogs for materials that show force chain behavior, the b-value, determined based on the acoustic emission data, seemed to decrease with increasing velocity, while the shear stress drops of NaCl only showed signs of the characteristic earthquake model on a small time scale. However, the effect of grain size distribution and deformation mechanisms might also be critical factors affecting the behavior of maximum shear stress drops and acoustic emission.

This thesis shows that determine between the two main types of frequency-magnitude models is not straightforward, as shear stress drops and acoustic emission do not necessarily show the same frequency-magnitude model. Different things need to be taken into account for the determination of them, including shear velocity, temperature, pressure and the properties of the material. This suggests that in nature, we might not expect solely the Gutenberg-Richter or the Characterstic earthquake model but also something in between.

2 Table of Contents

Contents

3 Introduction

Every region on the Earth's surface is subject to a specific set of natural hazards (Dragicevic et al., 2011). However natural disasters, such as tsunamis, tornadoes, floods, volcanic eruptions and earthquakes, remain unpredictable (Galkina and Grafeeva, 2019). Including one of the most dangerous and destructive phenomena: earthquakes (Elliott, 2020). On top of that, earthquakes can be a trigger for submarine and shoreline slope failure, causing tsunamis, land- and snowslides (Galkina and Grafeeva, 2019; Wright and Rathje, 2003). Earthquakes occur when the stress levels are reached that are necessary to overcome the friction of a fault. Then, a rupture along a fault patch, that was partially or fully locked for a period of time, can occur (Bollinger et al., 2004). Stress levels are being increased during interseismic periods on a patch of the fault that is predominantly locked and throughout the coseismic period, it slips along the weak zones accompanied by an energy release (Bollinger et al., 2004; Harris, 2017; Matsuzawa et al., 2002). During these interseismic periods, the stress buildups come from the tectonic driving forces of plate motion and are related to the deformation of the Earth's surface (Perfettini and Avouac, 2004).

By understanding the spatial distribution and the nature of earthquakes, treatments can be made to reduce risks. However, as detailed rheological properties and stress evolution on faults are still not fully known, forecasting of the timing and magnitudes of earthquakes remains enigmatic (Ben-Zion et al., 2003). As a consequence, predictions are still not very accurate, and can be many years off, possibly causing casualties and financial damages as people do not have enough time to prepare themselves adequately as earthquakes mostly happen without an explicit warning. (Rajabi et al., 2022; Rouet-Leduc et al., 2017). Therefore, the problem of earthquake forecasting becomes critical for human security, especially due to the growth of an exposed population in seismic active regions (Elliott, 2020). Nowadays, seismic hazard is based upon the likelihood of an earthquake to occur in a set period of time (Poulos et al., 2017; Sianko et al., 2020).

The evaluation of seismic hazard in a specific area can be accomplished through conducting probabilistic seismic hazard analysis (Budnitz et al., 1997). Different factors need to be taken into account when making a probability seismic hazard analysis, but one of the crucial factors is an empirical and statistical correlation that relates the distribution of numbers of earthquakes to a certain magnitude, a so called frequency-magnitude distribution (Doanh and Nguyên, 2023; Giardini et al., 1999). Two main types of these different earthquake distributions were proposed: the Characteristic and the Gutenberg-Richter earthquake model (Korkolis et al., 2021). To find the correct model, the recurrence time between earthquakes is needed. As the recurrence times for the largest earthquakes is long, sometimes hundreds of years, the number of earthquakes for a distribution becomes too small for the amount of data obtained (Abaimov et al., 2008; Korkolis et al., 2021; Meghraoui et al., 2012).

In laboratories, researchers create artificial seismic events within a controlled environment to simulate the complexities of natural seismic activity (Korkolis et al., 2021; McGarr, 1994). These experiments involve quasi-brittle fracture and stick-slip frictional failure experiments using analogue materials, which are commonly utilized as a proxy for earthquakes (Y. Jiang et al., 2017). Some of the materials used for these experiments include glass beads (e.g. Y. Jiang et al., 2017; Korkolis et al., 2021; Wu et al., 2017), quartz fault gouges (Niemeijer et al., 2008), and metallic glasses (Doanh and Nguyên, 2023). In these simulated seismic events, large amounts of total displacement can be achieved, in which the shear stress drops is considered to be a laboratory earthquake (Rouet-Leduc et al., 2017). During the experiments, thin layers of granular materials are placed between two solid blocks to mimic fault zones exhibiting stick-slip behavior. The results of these experiments reveal small friction drops under high normal stress, reproducing traditional statistical relationships such as the Gutenberg-Richter and Omori-Utsu law (Doanh and Nguyên, 2023; Korkolis et al., 2021). Moreover, these experiments enable the detection of acoustic emission signals, which are high-frequency stress waves resulting from the rapid release of strain energy within the materials (Terchi and Au, 2001; Zhang et al., 2019). This provides valuable insights

into the mechanics and characteristics of seismic events, further improving our understanding of earthquake behavior (Benabdallah and Aguilar, 2008).

This thesis tries to answer what the earthquake distribution of lab induced earthquakes in the rotary shear apparatus is. To do this, multiple experiments will be done in the rotary shear apparatus on different materials under a constant pressure of 8 MPa. These materials include glass beads varying in size, gypsum, KCl and NaCl. The materials are analogues that are related to the Earth's subsurface, in which earthquakes are likely to nucleate. The materials will be sheared with different velocities and the shear stress data as well as the acoustic emission data is analyzed to find possible frequency-magnitude distributions for lab-induced earthquakes. The final goal is to extent and improve the knowledge about earthquakes induced in the lab, including the better understanding of the behavior of earthquakes on different materials and their relationship to nature.

4 Frequency-Magnitude Distribution

4.1 Gutenberg-Richter earthquake model

In the 1944, Beno Gutenberg and Charles Francis Richter came up with the Gutenberg Richter law that shows a power law distribution between the relative frequency of seismic events larger than a certain magnitude (M) and is expressed as the following:

$$\log_{10} N = a - bM \tag{1}$$

where N is the number of earthquakes, M is the events magnitude and a and b are constants that show the amount of seismic activity in the region and the relative abundance of small and large earthquakes respectively (Gutenberg and Richter, 1944; Korkolis et al., 2021; Wesnousky, 1994). The relation holds for both natural as well as induced seismicity, including acoustic emissions (Lei and Ma, 2014). In nature, the Gutenberg-Richter law is recognized in certain earthquake groups with typical b-values that tend to vary for global seismicity (e.g. Monterroso and Kulhánek, 2003; Udias et al., 1976; Wesnousky, 1994), but are approximately equal to 1 when the magnitudes of the earthquakes are greater than 3 (Dahmen et al., 1998; Rundle, 1989).

The problem with the Gutenberg-Richter law is that the slope is only dependent on one parameter (the b-value) and therefore, the right hand tail does not have an upper bound. However, due to physics principles (e.g. conservation of energy), the Gutenberg-Richter law cannot be extrapolated to earthquakes with infinite magnitudes (Zöller, 2013). On Earth, magnitudes of earthquakes are limited with the largest one being the 9.5 Valdivia earthquake in Chile in 1960 (Dzierma et al., 2012), while in a laboratory, the largest magnitudes are controlled by the size of the sample and the amount of applied stress. Over the years, researchers have tried to improve on this problem and other earthquake models were proposed that have modified the Gutenberg-Richter law to a certain extent (Utsu, 1974). These models include the Gutenberg-Richter law with a sharp magnitude cut-off, the so called (doubly) truncated Gutenberg Richter law:

$$\left.\begin{array}{ll} \log n(M) = a - bM & \text{for} M \leq c \\ n(M) = 0 & \text{for } M > c \end{array}\right\} \tag{2}$$

The Gutenberg-Richter law with a sharp magnitude cutoff was criticized as a sharp magnitude cut-off seemed to be unphysical. Therefore, other models were suggested such as one by Tokuji Utsu (Riera and Iturrioz, 2012; Utsu, 1974):

$$\log n(M) = a - bM + \log(c - M) \tag{3}$$

Lomnitz and Neunhöfer (1964 and 1967, 1969) applied a lognormal distribution of energy to earthquakes and rockburst and came op with the form:

$$\log n(M) = a_1 + b_1 M - c_1 M2 \tag{4}$$

Săcuiu and Zorilescu (1970) concluded that the magnitude of earthquakes in Vrancea region has a lognormal distribution. This yields the formula in the form (Săcuiu and Zorilescu, 1970):

$$\log n(M) = a_2 + b_2 \log M - c_2(\log M)2 \tag{5}$$

Nevertheless, this review focuses solely on the Gutenberg-Richter law as the majority of existing literature is based on it, thereby disregarding other distributions.

4.2 Characteristic earthquake model

As mentioned, the Gutenberg-Richter relation is recognized in certain earthquake groups. The relation assumes that during the repeat time of an earthquake with a large magnitude, some fault slip is also accommodated by the occurrence of smaller earthquakes. However, not all fault systems show a power law distribution. Faults systems with a more regular geometry (presumably generated progressively with increasing cumulative slip) such as the San Andreas fault in California display power law distributions only for small events which occur in the time intervals between roughly quasi periodic earthquakes of a much larger 'characteristic' size which rupture the entire fault (Dahmen et al., 1998; Schwartz and Coppersmith, 1984). The faults have the tendency to generate earthquakes with maximum magnitudes in a narrow range (Schwartz and Coppersmith, 1984). The time between two of those earthquakes with maximum magnitude is characterized by generally quiescently period, with the exception of background noise and fore- and aftershocks. Therefore, there are practically no observed earthquakes of intermediate magnitudes on such geometrically regular fault systems. This kind of distribution is called the characteristic earthquake distribution (Dahmen et al., 1998).

Determining which model better describes the general character of seismicity of a particular fault zone is hampered because the historical and instrumental records of seismicity are generally too short to define the repeat time of the largest earthquakes, and hence, the shape of the magnitude frequency distribution cannot be defined confidently at the largest magnitudes (Kagan, 1993; Korkolis et al., 2021; Wesnousky, 1994). Moreover, to justify one of the two distributions (along with the formula), some interpretations and assumptions have to be done that are sometimes contradictory, as no formal testing can be done (Dahmen et al., 1998; Lomnitz, 1964). Further, previous works suggest that both of the types of distribution can be present along a heterogeneous fault zone (Dahmen et al., 1998).

5 Methodology

5.1 Materials tested

To induce lab earthquakes, I started shearing different materials under 8MPa normal stress. I have performed multiple experiments on different sample materials including: glass beads (r330, r333, r341, r343, r344, r346, r348 and r353), gypsum (r355), potassium chloride (r359 and r361) and sodium chloride (r363 and r365). For each of the materials, approximately 30.20 grams was used with the exception of r359, in which approximately 15.10g was used. The glass bead aggregates are spherical at first and have an initially grain size range that varies between 106-500 µm.

5.2 Rotary shear apparatus (RAP)

For this research, the rotary shear apparatus or ring shear apparatus (RAP), located in the Earth Simulation Laboratory at Utrecht University, was used to perform experiments on analogue materials. The RAP can produce significantly more shear displacements in a shorter time frame with respect to natural seismicity and can record acoustic emissions as well (Korkolis, 2017). The RAP at the Earth simulation laboratory consists of a torque reaction frame, manufactured by

Tevel Techniek bv, placed inside an Instron 8862 testing machine. The apparatus is equipped with a servo-controlled electromechanical actuator that can function in two modes: load control mode (with a range of ±100 kN and a resolution of 0.008 kN) or position control mode (with a range of ±50 mm and a resolution of 5 µm). To provide rotary motion to the driving plate, a Parker MH205 motor, along with a 1:160 harmonic drive gearbox, were assembled by VarioDrive. The precise control of the rotation (shear displacement) or the torque (shear stress) are controlled by the motor's onboard servo controller. The torque is measured by an in-line torque cell manufactured by HBM. The driving plate itself is equipped with two angular potentiometers (with a resolution of 0.001°or approximately 0.74 µm) that measure the rotation of the driving platter (Korkolis et al., 2021).

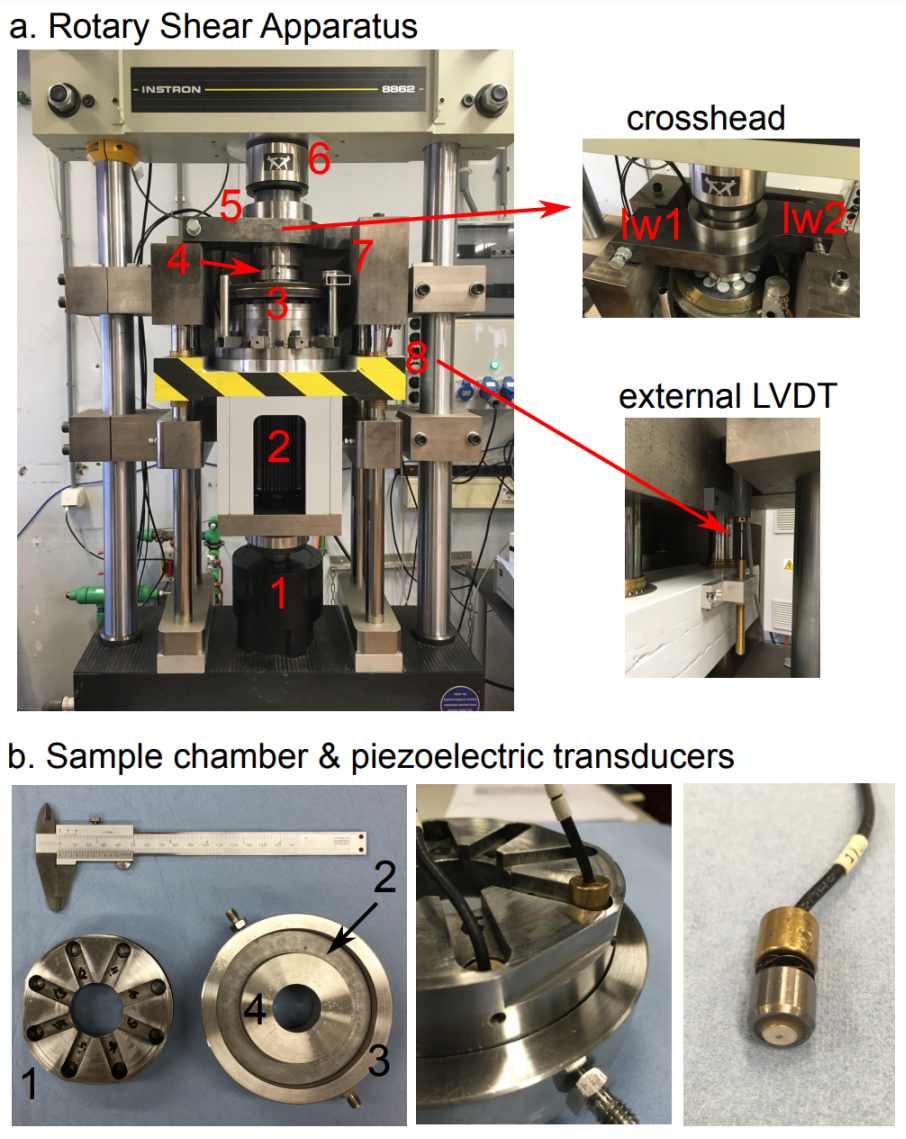

Figure 1: a) View of the rotary shear apparatus. 1: Instron actuator. 2: MH205 motor. 3: Harmonic drive and rotating platter. 4: Sample chamber. 5: Crosshead with two load cells. 6: Instron load cell. 7: Angular potentiometer. 8. LVDT. b, left) 1: Top piston. 2: Bottom piston. 3: Outer ring with fluid inlets. 4: Inner ring. b, middle) Assembled sample chamber with installed acoustic emission sensor. b, right) acoustic emission sensor (image from Korkolis et al., 2021)

.

5.3 Experimental procedure

First, two pair of O-rings were lubricated with the Molykote 111 Compound and placed in between the grooves in both the upper and lower piston to make sure that the inner and outer ring seal the sample. Then, the inner and outer confining rings are installed with the fluid inlets just above the teeth of the bottom piston. The fluid inlets are closed with screws (as all experiment are performed under dry conditions) and an annular cavity forms. In the annular cavity, the material is first positioned and flattened using a ring-shaped aluminum block. A spirit level is then placed on top of the aluminum block to check if the sample is horizontally aligned. If any deviation is observed, the aluminum block is taken out, and the material is adjusted and flattened once more to achieve maximum horizontal alignment. Once the sample is properly leveled, the aluminum block is removed, and the upper piston is installed, effectively closing the annular cavity. The upper and bottom piston have small teeth with a height of 200 µm and an average spacing of about 0.5 mm). Second, when the sample is finished, acoustic emission sensors, devices that generate an electrical signal in response to an acoustic wave, are installed. For all experiment, 8 acoustic emission sensors are used, (4 in the bottom and 4 in the upper piston) each positioned 90°from each other. An acoustic couplant, the aforementioned Molykote 111 Compound, is applied to the cap of the sensor, which is then positioned in the hole and pressed against the piston, the surface of which must be smooth and clean. A small screw is used to hold the acoustic sensor in position. When installed correctly, the acoustic emission sensors are at approximately 5 mm from the sample. Then, the sample is placed in the rotary shear apparatus, with the bottom piston interlocking with the driving platter and the AE sensors attached to the data receiver. The actuator is then moved upwards, lifting the driving platter and the sample, interlocking the top piston with the crosshead. After establishing contact axially and making sure that the crosshead is placed horizontally above the sample, the actuator was switched to load control mode and the 8 MPa (-31.394 kN) normal load was applied gradually. To make sure the AE sensors work and to check the response of the system, the sample is struck with a rubber hammer. An AE-sensor that is installed in the bottom piston is chosen to be the triggered sensor. If the set 0.005 mV trigger threshold is met in this triggered sensor, then the systems starts to record an acoustic event for 3 ms with a frequency of 1 Mhz, while the sampling rate of the RAP itself is set to be 1000 Hz for all the experiments. The clockwise rotation was applied via the MH205 motor at a constant rate until about 50.000 AE events were recorded or until a maximum of three hours had passed and the 50.000 events were not obtained. During the experiment, the velocity was changed from 0.001 to 0.064 rpm with the geometric sequence with common ratio 2 (0.006 to 0.384°). The parts of the experiments at a specific velocity are called (velocity) segments and after these velocity segments, the rotation is sometimes stopped to save the already obtained data. This is done to make the data set smaller in size, while the normal stress was not released during the experiment; only the recording was stopped. After all velocity segments were done, a small counter-clockwise rotation was performed until the shear stress was removed from the system, after which the normal stress was reduced gradually. During all the experiments, the temperature and air humidity were measured using a Siemens thermometer and a Fischer hygrometer.

5.4 Data processing

First of all, the points that mark the beginning and ending of the rotation were determined in the obtained data set. Therefore, the application of normal stress and final check ups (including little rotation to make sure that the load washer work) are excluded. Additionally, the AE-events that were recorded during these periods are excluded as well, making them crucial for a further smooth progress of the data analysis. Further, a uniform filter was used to filter out the background noise. This filter replaces one data point of the shear stress by the mean value of a time interval around this shear stress value. For the time interval, 2% of the sampling rate is used (e.g. 20 shear stress value points). This value was chosen as it does not affect the locations and heights of the stress drops significantly. As a result, the model is still capable to determine the peaks and associated valleys of the shear stress with much more precision along with a considerable decrease in model

running time.

As threshold for the shear stress drop, the minimum value of 0.02 V is chosen. This was done to make sure that all of the background noise is filtered out and therefore has no influence on the stress drops and thus on the b-value. As a consequence, the model cannot determine labquakes that have a value lower than this threshold. However, the threshold is small enough to make sure that precursors, that might initiate before the maximum stress drop, are identified. As mentioned, during the experiment, the 8 MPa normal stress was not removed until the experiment was fully completed, and thus the results from all the velocity segments were recorded. However, to decrease the file size, the recording of every single velocity segment stopped, to save all the data obtained. Therefore, the output of the model might show negative shear stresses during some velocity segments. To compensate for this, the last shear stress value before the interval in which the data is stored, is added to all the shear stress data of the next velocity segment. The intervals in which the data was stored is cropped and the shear stress is then directly linked to the next velocity, assuming that the final shear stress value is equal to the initial shear stress of the next velocity. Nevertheless, the negative shear stress does not affect the results of the b-value of the shear drop, as only the difference between the peak and valley of the shear stress drop data is needed. To determine the b-value of the acoustic emission data, the absolute value of the maximum or minimum amplitude of the AE-data was regarded as the magnitude for the labquake. For the threshold of the AE-data, the minimum value of 0.005 V is chosen. As the triggered sensor was most of the time the sensor with one of the largest amplitudes, it happened that the amplitude of the other sensors remained smaller during a labquake. Therefore, dataset of non-triggered sensors might be smaller than the dataset of the triggered sensors when the amplitude of the acoustic emission did not exceed the threshold. Further, to determine the b-value in the Gutenberg-Richter law $N = 10^{a-bM}$, I used the curve_fit toolbox. This optimization tool finds the best parameter for the function that matches the obtained experimental data. For the determination of the b-value of the median acoustic emissions throughout the experiment, a sliding window that contained 1000 acoustic emissions that surpassed the 0.005 V threshold was used, which is shifted by 100 events, in which therefore 900 events overlap each time.

5.5 Measuring size of AE events

During one trigger event, the absolute value of the minimum or maximum amplitude of that event was taken as the characteristic amplitude. So for one event, eight different characteristic amplitudes were observed (for every single AE-sensor, a single amplitude). From all the eight events, both the median and maximum were used in this thesis.

5.6 Post-experimental analysis

After the experiment, the sheared sample material was collected and used for grain sizes analysis using the Mastersizer S laser diffraction particle sizer.

6 Results

The result section is subdivided into four different subsections. The first one focuses on the glass bead experiments, the second one on the gypsum experiment, the third one on the KCl experiment and the last one on the NaCl experiment. This result section only consists of the experiments with enough AE data points for every single velocity. Therefore, experiments without enough data points per velocity were excluded. For glass beads, six different experiments (r330, r333, r341, r346, r348, r353) have done the full cycle of experiments (from 0.001 to 0.064 rpm) of which r353 was rotated from fast to slow velocity (from 0.064 to 0.001 rpm). For gypsum, only one experiment (r355) was done. For KCl, experiment (r361) did a full cycle of experiments and for NaCl, experiments (r363 and r365) did a full cycle of experiments. The general information of the experiment, along with the main information about both the shear stress drops and the acoustic

data, can be found in Table 1, 2, 3 and 4. A more detailed description of every experiment is given below. For the determination of a reliable earthquake distribution, at least 1000 data points are necessary (Chernick, 1999). If this amount was not reached, b-values were not considered to be reliable, but might be determined.

Experiment	Initial grain size (in µm)	Pressure	Torsional stiffness	Weight (in g)	Temperature (in °C)	Air humidity	Velocity (rpm; °/min)	Total displacement (in rotation)	Number of stress drop	Number of AE events for b-value	Maximum shear stress drop (in MPa)	Maximum median AE (in V)	Maximum maximum AE (in V)	b-value stress drop	R^2 value ss	b-value max AE	R^2 max	b-value median AE	R^2 median AE
R330	425-500	8MPa	High	30.20	21.5	33.5%	0.001	0.072	1077	41764	0.536	0.964	5.079	0.873	0.978	0.649	0.949	1.057	0.992
							0.002	0.074	1354	53613	0.427	0.438	3.118	0.952	0.962	0.703	0.968	1.169	0.997
							0.004	0.071	1042	50263	0.396	0.526	3.053	0.928	0.951	0.862	0.983	1.296	0.998
							0.008	0.079	1245	51397	0.359	0.671	3.005	1.053	0.970	0.907	0.982	1.361	0.999
							0.016	0.092	899	50322	0.270	0.609	2.742	0.879	0.945	0.942	0.981	1.419	0.999
							0.032	0.120	987	49835	0.255	0.540	2.883	0.934	0.934	0.937	0.981	1.335	0.999
							0.064	0.328	862	57230	0.449	1.594	5.079	0.562	0.832	0.897	0.984	1.294	0.998
R333	180-212	8 MPa	High	30.21	21.6	38%	0.001	0.084	598	51613	0.491	2.796	4.825	0.627	0.959	0.671	0.971	0.990	0.995
							0.002	0.090	771	58223	0.194	0.490	0.969	1.380	0.977	0.651	0.963	0.987	0.991
							0.004	0.086	388	50118	0.136	0.299	0.579	1.955	0.976	0.670	0.960	1.090	0.988
							0.008	0.099	87	50274	0.084	0.604	0.190	1.609	0.926	0.672	0.951	1.103	0.985
							0.016	0.124	231	50227	0.070	0.317	1.207	1.787	0.933	0.654	0.922	1.046	0.986
							0.032	0.142	576	49970	0.089	0.277	0.772	2.258	0.961	0.658	0.926	0.984	0.984
							0.064	0.137	622	37503	0.285	1.522	2.980	1.608	0.981	0.641	0.929	0.914	0.976
R341	106-125	8MPa	High	30.27	21.4	42%	0.001	0.068	578	51778	0.486	1.163	1.226	0.636	0.977	0.649	0.949	1.057	0.992
							0.002	0.050	469	50087	0.346	0.471	1.153	1.341	0.981	0.703	0.968	1.169	0.997
							0.004	0.051	420	49987	0.128	0.250	1.319	1.847	0.972	0.862	0.983	1.296	0.998
							0.008	0.063	502	50164	0.155	0.276	1.517	1.420	0.963	0.907	0.982	1.361	0.999
							0.016	0.079	621	50908	0.150	0.391	1.912	0.974	0.969	0.942	0.981	1.419	0.999
							0.032	0.107	923	50566	0.167	0.417	1.591	0.951	0.902	0.937	0.981	1.335	0.999
							0.064	0.197	1657	51201	0.210	0.669	2.060	1.092	0.856	0.897	0.984	1.294	0.998
R346	425-500	8MPa	High	30.20	21.5	37.5%	0.001	0.059	799	51907	0.573	1.457	2.964	0.924	0.983	0.750	0.995	0.882	0.999
							0.002	0.060	887	50965	0.407	1.085	3.300	1.034	0.979	0.758	0.996	0.844	0.999
							0.004	0.056	857	59235	0.435	1.085	3.641	0.925	0.963	0.748	0.995	0.838	0.998
							0.008	0.055	514	50361	0.420	1.367	4.083	1.005	0.941	0.692	0.995	0.794	0.999
							0.016	0.076	883	54651	0.369	1.406	4.558	0.734	0.943	0.626	0.994	0.754	0.999
							0.032	0.100	843	51166	0.320	1.504	5.079	0.940	0.900	0.541	0.979	0.700	0.998
							0.064	0.181	1185	50359	0.244	1.255	5.079	1.046	0.852	0.497	0.962	0.626	0.991
R348	300-355	8MPa	High	30.20	21.4	58%	0.001	0.075	1084	51749	0.565	1.195	4.881	0.836	0.978	0.680	0.988	0.832	0.998
							0.002	0.056	796	50306	0.505	1.176	5.079	0.960	0.970	0.718	0.995	0.859	0.998
							0.004	0.061	955	57487	0.477	1.153	2.805	0.909	0.971	0.950	0.995	1.010	0.995
							0.008	0.057	816	50335	0.434	0.911	3.729	0.915	0.970	0.650	0.991	0.811	0.998
							0.016	0.070	811	50682	0.326	1.160	2.620	0.867	0.952	0.587	0.987	0.752	0.997
							0.032	0.097	650	51641	0.538	1.361	3.014	0.723	0.809	0.525	0.981	0.689	0.994
							0.064	0.183	1089	51787	0.248	1.464	4.043	0.763	0.843	0.480	0.959	0.617	0.982
R353	425-500	8MPa	High	30.20	21.4	58%	0.001	0.037	514	50155	0.338	0.341	2.530	1.100	0.973	1.119	0.988	1.055	0.998
							0.002	0.061	815	69838	0.359	0.343	2.725	1.079	0.984	1.039	0.994	1.050	0.998
							0.004	0.093	1216	86330	0.458	0.560	2.661	0.955	0.969	0.884	0.999	1.027	0.998
							0.008	0.070	766	50280	0.425	0.483	3.520	0.835	0.956	0.809	0.996	1.057	0.999
							0.016	0.097	905	50861	0.418	0.428	3.059	0.751	0.931	0.744	0.993	1.006	0.999
							0.032	0.149	1024	52942	0.385	0.690	2.782	0.669	0.889	0.679	0.994	0.929	0.999
							0.064	0.242	1427	54666	0.295	0.661	2.759	0.731	0.871	0.592	0.992	0.846	0.998

Table 1: Data from the glass beads experiments, subdivided per velocity.

Experiment	Initial grain size (in µm)	Pressure	Torsional stiffness	Weight (in g)	Temperature (in °C)	Air humidity	Velocity (rpm; °/min)	Total displacement (in rotation)	Number of stress drop	Number of AE events for b-value	Maximum shear stress drop (in MPa)	Maximum median AE (in V)	Maximum maximum AE (in V)	b-value stress drop	R^2 value ss	b-value max AE	R^2 max	b-value median AE	R^2 median AE
R355	-	8MPa	High	30.20	21.6	49%	0.001-0.032	1.780	143	747	1.017	0.207	0.402	-	-	-	-	-	-

Table 2: Data from the gypsum experiment.

Experiment	Initial grain size (in µm)	Pressure	Torsional stiffness	Weight (in g)	Temperature (in °C)	Air humidity	Velocity (rpm; °/min)	Total displacement (in rotation)	Number of stress drop	Number of AE events for b-value	Maximum shear stress drop (in MPa)	Maximum median AE (in V)	Maximum maximum AE (in V)	b-value stress drop	R^2 value ss	b-value max AE	R^2 max	b-value median AE	R^2 median AE
R361	-	8MPa	High	30.24	21.0	53%	0.001	0.059	-	833	-	-	-	-	-	-	-	-	-
							0.002	0.152	-	2182	-	-	-	-	-	-	-	-	-
							0.004	0.065	1	3011	0.043	0.008	0.015	-	-	-	-	-	-
							0.008	0.309	-	23293	-	0.016	0.036	-	-	2.658	0.996	4.493	0.993
							0.016	0.541	4	42635	0.079	0.038	0.050	-	-	2.700	0.998	3.025	0.993
							0.032	0.514	5	50016	0.191	0.014	0.032	-	-	2.826	0.996	5.994	0.988
							0.064	0.616	4	53543	0.079	0.020	0.034	-	-	2.986	0.996	5.045	0.992

Table 3: Data from the KCL experiment, subdivided per velocity.

Experiment	Initial grain size (in µm)	Pressure	Torsional stiffness	Weight (in g)	Temperature (in °C)	Air humidity	Velocity (rpm; °/min)	Total displacement (in rotation)	Number of stress drop	Number of AE events for b-value	Maximum shear stress drop (in MPa)	Maximum median AE (in V)	Maximum maximum AE (in V)	b-value stress drop	R^2 value ss	b-value max AE	R^2 max	b-value median AE	R^2 median AE
R363	-	8MPa	High	30.20	21.8	39%	0.001	0.034	14551	84	0.312	-	-	2.997	0.938	-	-	-	-
							0.002	0.142	4764	10210	0.404	0.034	0.126	0.541	0.356	0.842	0.893	1.263	0.617
							0.004	0.392	19519	19519	0.419	0.095	0.266	3.897	0.901	1.046	0.900	0.802	0.765
							0.008	0.278	14558	50058	0.312	0.200	0.524	2.826	0.919	1.283	0.879	0.524	0.724
							0.016	0.407	2	50374	0.200	0.025	0.087	0.741	0.915	2.458	0.967	2.845	0.987
							0.032	0.353	-	53310	-	0.023	0.079	-	-	3.024	0.932	2.519	0.974
							0.064	0.664	4	53138	0.121	0.027	0.045	1.404	0.955	4.825	0.752	5.865	0.990
R365		8 MPa	High	30.21	21.6	43%	0.001	0.046	-	30	-	-	-	-	-	-	-	-	-
							0.002	0.046	-	9	-	-	-	-	-	-	-	-	-
							0.004	0.155	4920	67254	0.5516	0.166	0.567	0.573	0.374	1.563	0.955	0.503	0.917
							0.008	0.273	9081	50066	0.206	0.104	0.298	2.038	0.508	1.470	0.971	0.427	0.632
							0.016	0.351	21136	50263	0.193	0.069	0.211	2.174	0.926	0.854	0.967	1.042	0.730
							0.032	0.436	-	49958	-	0.027	0.161	-	-	1.140	0.991	2.518	0.997
							0.064	0.625	-	51045	-	0.044	0.143	-	-	0.847	0.913	2.368	0.997

Table 4: Data from the NaCl experiments, subdivided per velocity.

A general overview of the shear stress data for all the experiments is shown in this result section, with more detailed figures supplemented in the appendix for specific velocity segments.

6.1 Glass Beads

6.1.1 Experiment 330

For experiment 330, the initial grain size ranges between 425-500 µm. After the rotation started, the shear stress increases almost immediately to about 2.5 MPa, and stick-slips start to occur. A

small increase in shear stress follows, followed by decrease in maximum shear stress that continues until about the 0.016 rpm velocity, after which the maximum shear stress increases to about 3.0 MPa (Figure 2). Between 862 and 1354 shear stress drops was determined per velocity segment, with an overall decreasing trend of the maximum shear stress drop with increasing velocity. For the slowest velocity segment, the b-value through the shear stress drops, plotted against their normal cumulative count is 0.87317 (Figure 12). b-values for the velocities 0.002, 0.004, and 0.008 rpm are 0.952, 0.928, 1.053 respectively and have associated R-squared values of 0.962, 0.951, 0.970. While velocities 0.001, 0.016, 0.032, and 0.064 rpm did not have more than 1000 shear stress drops recorded while being sheared. When tried to improve on the R-squared value, and a maximum cut-off is used, the R-squared value remains about the same for all the velocity segments. With increasing velocity, the time before and after every stress drop decreases from a maximum of about 25 seconds to a minimum of 0.5 seconds (Figure 13, 14). Further, the sizes of the shear stress drop throughout a single velocity segment do not cluster at one specific value (Figure 15).

About 50.000 acoustic emissions are being recorded for every sensor for every velocity segment. For all the acoustic emissions that surpassed the 0.005 V threshold, the b-value was calculated through these points when plotted against the normal cumulative count (Figure 12). The median and maximum b-value for every single experiment at a specific velocity show variations throughout experiment r330. Sensor 4 is being excluded as the minimum shear stress of this sensor lies far above the threshold. For the determined b-values, the R-squared values do not drop below 0.94 for every velocity segment. The amount of time that passes by before 10% of the total amount of acoustic data points is recorded is nearly constant during each velocity segment (Figure 16). However, the recurrence time, determined with respect to the previous acoustic emission, is not constant and therefore shows no clustering independent on the velocity (Figure 17).

When looked at the variations of the median b-value throughout experiment r330 by using a sliding window, it can be observed that the b-value decreases with increasing velocity, with the largest b-values (between 0.85 to 1.15) in the beginning, and the smallest b-values (between 0.70 and 0.86) at the 0.064 rpm velocity (Figure 18, 20). Per velocity, a small stepwise decrease in the b-value of the acoustic emissions is noticeable (compare Figure 19 and 20). The R-squared of the b-value in the sliding window remains relatively high and does not drop below 0.95.

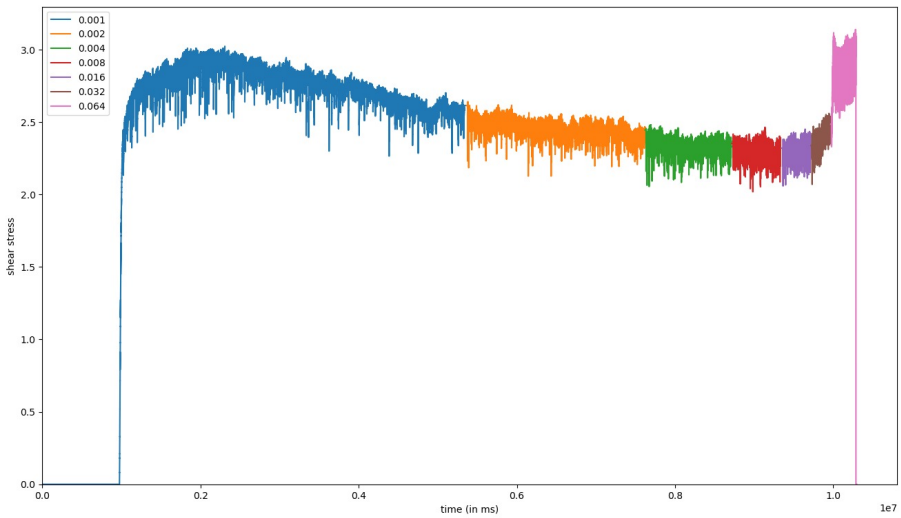

Figure 2: Glass beads experiment with shear stress drops.

6.1.2 Experiment r333

Experiment r333 has a initial grain size varying from 180-212 µm. After the rotation started, the shear stress increases sharply to about 2.0 MPa and large shear stress drops start to form (Figure 3). The amount of large shear stress drops along with their sizes, with a maximum of 0.491 MPa, significantly decreases during the 0.001 segment and never reaches the same size again during the whole experiment. The largest stress drop that were noted after the 0.001 rpm velocity segment are in the very last section of the 0.064 rpm segment, in which a sudden period with very large shear stress drops occurred, and reached a maximum size of 0.285 MPa. The total amount of stress drops that were determined are 2735, varying from 85 to 620 per velocity segment. Therefore, there are not enough stress drops determined for the model to give a reliable b-value along with an associated R^2. During the last part of the 0.001 and the 0.002 rpm velocity segments, the time before and after every shear stress drop appears to roughly cluster, while the later part is more chaotic. However for the faster velocities, 0.016, 0.032, and 0.064, the time before and after every shear stress drop seems to approximately cluster during the first part of the experiment (compare Figure 21 and 22).

The b-value that was fitted through the data points for the acoustic emissions that surpasses the 0.005 V threshold for the median data points changes per velocity segment only slightly and varies between 0.914 and 1.103 (Figure 23). The median AE b-values are for the 0.001 and 0.002 almost equal to 1 and both have R^2 values of 0.995 and 0.991, after which the b-value slightly increases to about 1.10 for velocities 0.004, 0.008, and 0.016 after a decrease to 0.914 follows. For these b-values, the R^2 does not drop below a value of 0.976. The b-values vary during the velocity segment when using a sliding window, but remain to have significant high R^2 values (Figure 24). No sudden de- or increase can be observed at places with the largest shear stress drops or acoustic emissions. However, the 0.064 rpm velocity segment has a sudden period of very large shear stress drops and acoustic emissions. This has a significant influence on the b-value during the velocity segment as it decreases immediately (Figure 25). The time before 10% of the acoustic data was observed remains almost constant, with no more than 10% of the mean, during the whole experiment (Figure 26).

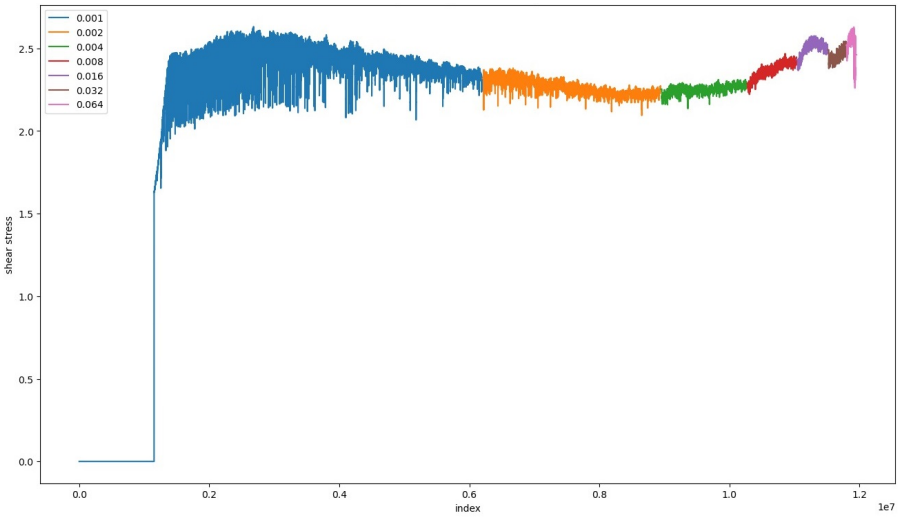

Figure 3: Glass beads experiment with shear stress drops.

6.1.3 Experiment r341

During this experiment, the initial grain size ranged between 106-125 µm. After the rotation started, an initial increase to about 2.5 MPa is observed (Figure 4). Per velocity segment, the

height of the maximum shear stress increases. The maximum shear stress drops can be observed during the 0.001 rpm velocity segment after which it decreases. Between 418 and 1527 shear stress drops are being determined with a total of 5028 during the full experiment. As the 0.064 rpm velocity is the only one with more than 1000 data points, the only reliable b-value can be determined from this experiment and has a value of 1.092 with an R^2 of 0.856 (Figure 27). For improving the b-value of 0.064 rpm, a minimum cut-off can better be used to increase the R^2 value. For example, a minimum cut-off of 0.04 (instead of 0.02) gives a b-value of 2.111 and a R^2 of 0.941. What can be observed is that during the first part of the 0.001 experiment, the largest shear stress drops are present, as well as during the 0.064 rpm experiment, where the recovery in shear stress took place after a sudden drop. For both velocities, the time in which these largest shear stress drops occurred, differ with respect to the rest of the experiment (Figure 28, 30). For the other velocity segment, the time before and after the shear stress drop along with the size of the shear stress drop before and after the shear stress drop remains quite chaotic and does not cluster (Figure 29).

The time before 10% of all the acoustic emissions were recorded does not deviate with more than 10% of the mean with the exception of the first period of the 0.001 experiment and three periods in the 0.064 rpm experiment as they did not record any acoustic emissions during the experiment (due to a problem with the recording) (e.g. Figure 31). b-values show an increase and subsequent decrease with increasing velocity from 0.001 to 0.016 with median AE b-values of 1.057 (Figure 32), 1.169, 1.296, 1.361, and 1.419 to 1.335, and 1.294 for the velocities from 0.032, to 0.064 rpm. All b-values have an R^2 value that is greater than 0.992. In addition, the recurrence time, determined with respect to the previous acoustic emission, is not constant and therefore shows no clustering independent on the velocity (Figure 33).

After the start of the experiment, the b-value of the acoustic emissions during the 0.001 rpm velocity segment decreases significant (Figure 34). As can be seen for the b-value during the velocity segment at 0.064 rpm, the b-value drops after the sudden drop in shear stress. However, b-values also significantly increase during the recovery phase (Figure 35).

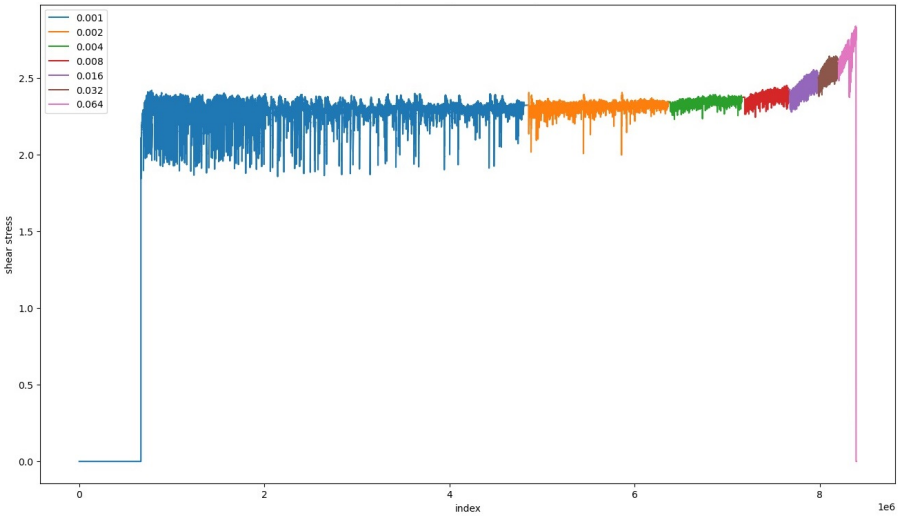

Figure 4: Glass beads experiment with shear stress drops.

6.1.4 Experiment r346

This experiment is a repeat of experiment r330 and is performed under the same conditions. It has a grain size varying from 425-500 µm. The shear stress after the start of the rotation increases to about 1.8 MPa and during the first part of the 0.001 rpm velocity segment to about 2.7 MPa

after which it gradually decreases during the 0.001 velocity segment (Figure 5). At the start of the 0.002 rpm velocity segment, a sharp decrease of shear stress can be noticed after which it slightly increases until 0.032 rpm and decreases again. Overall, the size of the shear stress drops decrease with increasing velocity, with 0.002 rpm the only exception. For velocity 0.064 rpm, enough shear stress drop data is available to determine a reliable b-value. This value is 1.046 (Figure 36), with an associated R^2 value of 0.852. The velocity changes do not have an effect on the clustering of the time intervals (e.g. Figure 38), nor does the size of the shear stress drop cluster at one specific value (Figure 37).

For the acoustic emissions, the median AE b-values are 0.882, 0.844, 0.838, 0.794, 0.754, 0.700 (Figure 39), and 0.626, with associated R^2 values of 0.999, 0.999, 0.998, 0.999, 0.999, 0.998, and 0.991 respectively for the velocities 0.001, 0.002, 0.004, 0.008, 0.016, 0.032, and 0.064 rpm. The b-values for the all the acoustic data show a decrease, while R^2 values do not drop below 0.95. The time before 10% of the acoustic emission data is recorded changes slightly during the experiment but does not deviate with more then 10% from the mean (Figure 40), with the exception of the run in period of the experiment and 0.064, as also in this experiment, something went wrong with the recording of the data during the 0.064 rpm velocity segment (Figure 41). In contrast to the size of the shear stress drops, the maximum size of the acoustic emissions increase with increasing velocity.

When looking at the change of the median AE b-value during each velocity segment, we can see that at first, during the run in period, the b-value is significantly lower compared to the rest of the experiment (Figure 42). We can sometimes notice a small stepwise decrease in b-value, between the experiments, while the R^2 does not drop below 0.980 (compare Figure 42 and Figure 43). As can be seen in Figure 41, there does not seem to be a correlation between the largest shear stress drops or acoustic emissions and a sudden in- or decreases of the b-value.

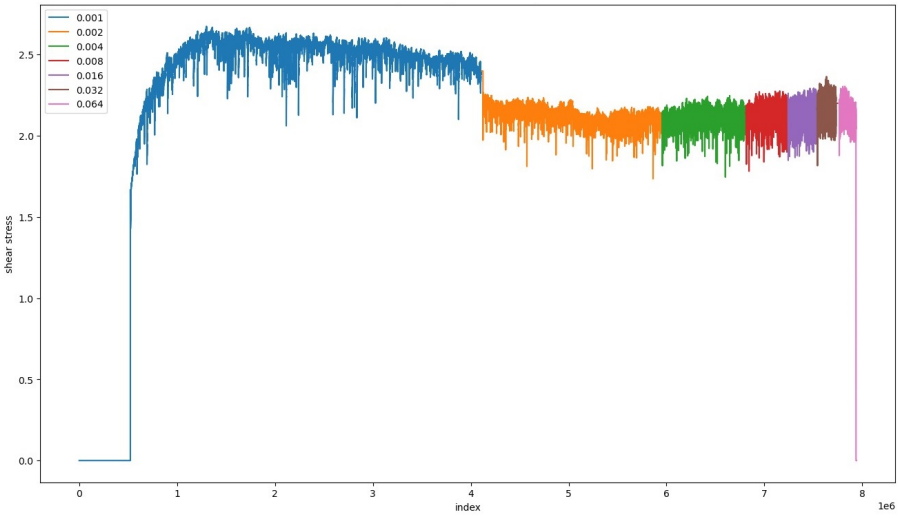

Figure 5: Glass beads experiment with shear stress drops.

6.1.5 Experiment r348

For experimerent r348, the grain size ranges between 300-355 µm. After the start of the rotation, the shear stress data increases to about 1.5 MPa after which shear stress drops start to form. The shear stress further increases to about 2.5 MPa, which remained the maximum shear stress throughout the whole experiment (Figure 47). The shear stress envelope decreases later in the experiment with the highest shear stress drops at the 0.001 rpm velocity. Only during the 0.001 and the 0.064 rpm velocity, enough shear stress drops were determined for reliable b-values. These

are 0.836 (Figure 44) and 0.763 with associated R^2 of 0.978 and 0.843 respectively. A maximum cut-off does not significantly increase these values. Moreover, recurrence times for shear stress drops do not cluster but show a wide spread (Figure 45).

The b-values of the acoustic emissions during this experiment remain about the same for the 0.001, 0.002, 0.004, and 0.008 rpm velocity segments with median b-values of 0.832, 0.859, 0.835, and 0.811. After this, the b-value values starts to decrease with values of 0.752, 0.689, and 0.617 for the velocities 0.016, 0.032, and 0.064 rpm and R^2 values that are never smaller than 0.998 (Figure 46). Also during the 0.064 rpm velocity segment, something went wrong with the recording at the fastest velocity; there are periods where no acoustic emissions were recorded. Because of this, during this experiment, there are periods where the time is more than 10% off the mean in which 10% of the acoustic data was recorded. For the rest of the experiment however, 10% of the acoustic data is recorded in about the same time frame (Figure 47). The only exception is the run in period of the 0.001 rpm velocity.

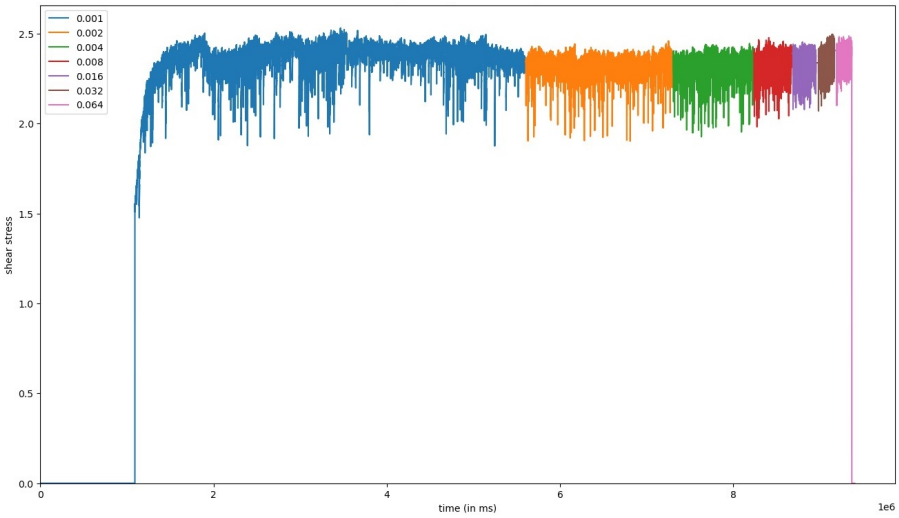

Figure 6: Glass beads experiment with shear stress drops.

6.1.6 Experiment r353

This experiment is comparable to experiment r330 and r346. The only significant difference is that during this experiment, the velocity was set to go from fast (0.064 rpm) to slow (0.001 rpm) (instead from slow to fast). During the experiment, a small increase in shear stress can be observed during the full experiment (Figure 7). The biggest stress drop was recorded during the 0.004 rpm velocity segment. 6464 stress drops were observed during the whole experiment, varying from minimal 512 to a maximum of 1336 per velocity segment. Velocities with more than 1000 shear stress drops are 0.004, 0.032, and 0.064 rpm. The b-values for the shear stress drop are 0.955, 0.669, and 0.731 (Figure 48) and become larger for every decrease in velocity, with the exception of 0.064 rpm. However, the two fastest velocities do not have a R^2 that is greater than 0.90. When a maximum cut-off of 0.2 MPa for shear stress drop is used, R^2 values increase to just above 0.90 and b-values go to 0.607 and 0.388. When this is done, all the b-values increase with decreasing velocity. The velocity changes do not have an effect on the clustering of the time intervals (Figure 49), nor does the size of the shear stress drop cluster at one specific value (Figure 50). Both remain chaotic.

For the acoustic data points that were recorded, b-values were determined. All with R^2 values greater than 0.988. The b-values are therefore considered to be reliable and vary for the median acoustic data between 0.592 (Figure 51) and 1.119 and for the maximum acoustic data between

0.846 (Figure 51) and 1.055, all with decreasing b-value when velocity is increased. When b-values are determined throughout the experiment, some minor changes can be observed (no more than 10% variation with respect to mean), but all R^2 values remain quite large (Figure 52). Recurrence time for these acoustic emissions does not show a clustering (Figure 53), just as the pre and next acoustic emission (Figure 54).

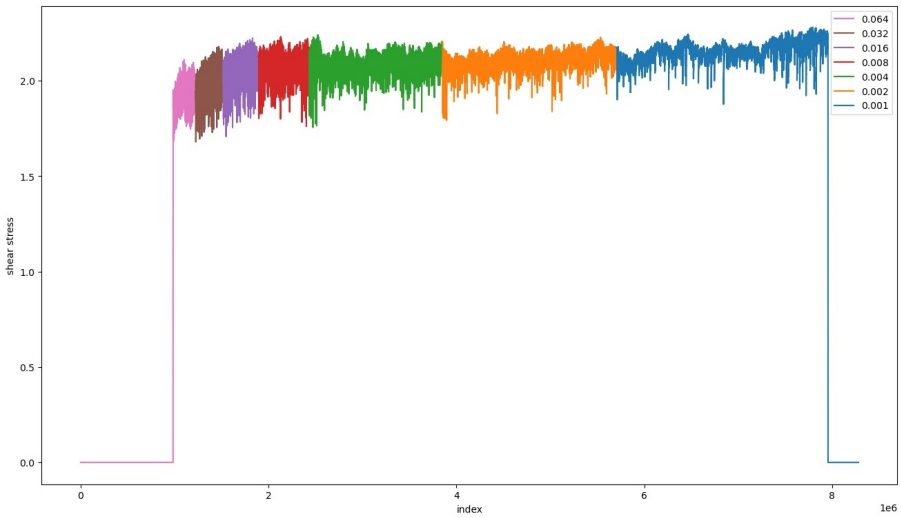

Figure 7: Glass beads experiment with shear stress drops.

6.2 Gypsum

6.2.1 Experiment r355

For experiment r355, the velocity was increased throughout the experiment without stopping of the recording. As can be seen, a first gradual increase, with some stress drops, can be observed when the experiment is started, reaching a maximum value of about 6.2 MPa, after which a decrease in shear stress drop can be seen without any shear stress drops that overcome the threshold (Figure 8). After the velocity was increased further to 0.002, 0.004, 0.008, 0.016, and 0.032 rpm, a small but sharp increase in shear stress can be seen at the point where the velocity is changed, but no shear stress drops that are large enough were registered anymore. The amount of data points to determine reliable b-values for stress drops is therefore too small. For the acoustic emissions, a total of 747 were record for the complete experiment, with the majority, and the overall largest ones, during the shear stress build (Figure 55). Further, after the maximum shear stress value was reached, also the amount of acoustic emissions significantly decreased. During the remaining part of the 0.001 rpm and the 0.002 rpm velocity segment, only a handful of acoustic emissions were recorded. When velocity was further increased, the amount of acoustic emissions increased, with most acoustic emissions recorded during the 0.016 rpm segment and the largest of the whole experiment during the 0.032 rpm velocity segment. Just as for the shear stress drops, not enough acoustic emission data is recorded to determine any reliable b-value.

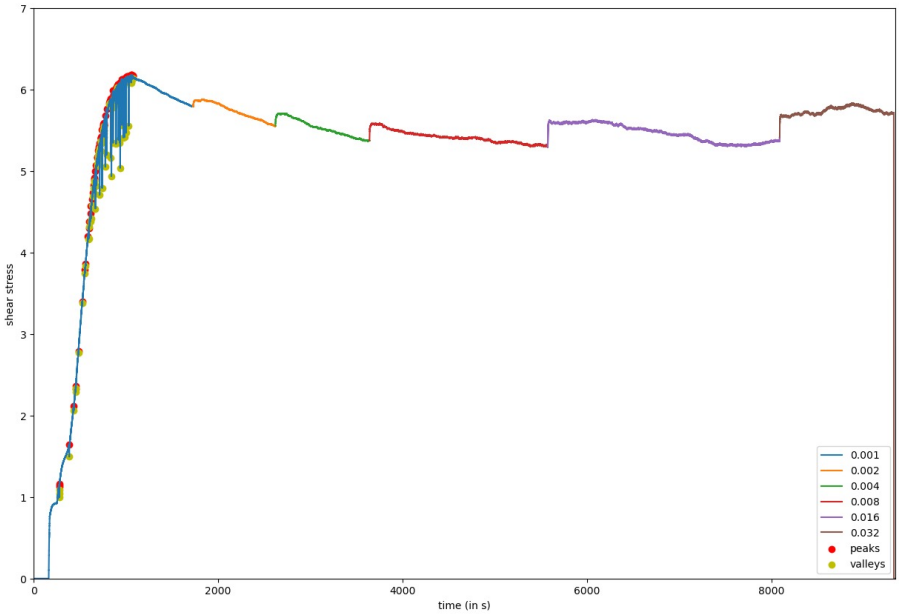

Figure 8: Gypsum experiment with shear stress drops.

6.3 KCl

6.3.1 Experiment r361

For the KCl experiment, the experiment and recording were not stopped after the increase from 0.001 rpm to 0.002 rpm and from 0.002 rpm to 0.004 rpm. However, after that, the experiment was stopped after each velocity segment for an indefinite period of time. When started again, a sharp decrease was noticed followed by a large sharp increase and another decrease in shear stress. During the whole experiment, no stick-slip behavior was observed and only a handful of stress drops were observed that are larger than the set 0.02 MPa threshold (Figure 9). b-values for shear stress were therefore not determined.

The largest acoustic emissions were recorded in periods with lots of acoustic emissions, which were alternated by periods with none to almost none acoustic emissions (Figure 56). Because of this, periods in which 10% of the acoustic emissions are recorded vary substantially throughout every constant velocity segment (Figure 57). Maximum acoustic emissions are relative small with respect to glass beads and therefore not all sensors surpass the 0.005 V threshold for every event. The median b-value can therefore only be determined for the 0.008, 0.016, 0.032 (Figure 58, 59), and 0.064 rpm experiment and have values of 3.634, 2.208, 7.401, and 7.766 respectively, all with relative high R^2 values. Because of the aforementioned reason, the development of the median b-values during the experiment could not be determined. Moreover, the recurrence time of the acoustic emissions seems to cluster in specific humps (Figure 60).

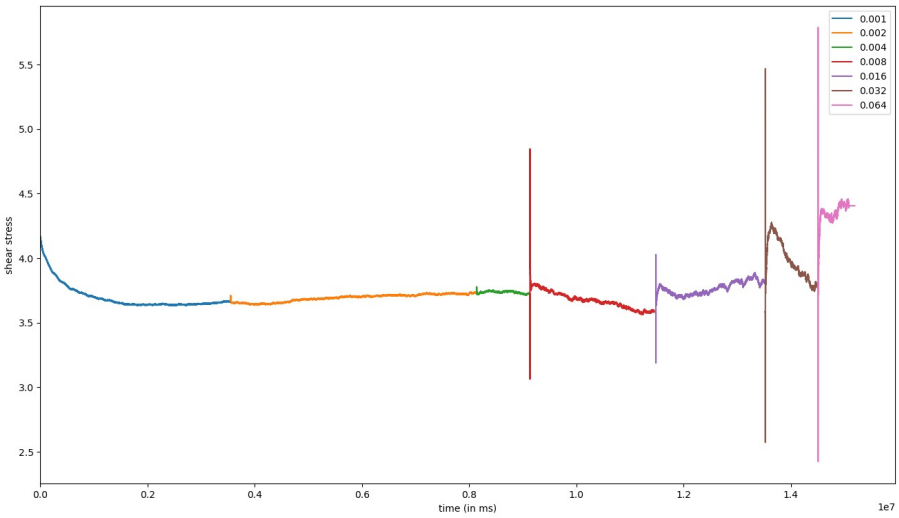

Figure 9: KCl experiment without shear stress drops.

6.4 NaCl

6.4.1 Experiment r363

Experiment r363 shows a clear immediate increase in shear stress with a subsequent sharp decrease to about 1.1 MPa. After every velocity increase, the experiment was stopped for a variable period of time. When the experiment resumed, a small decrease followed by a significant increase in shear stress drop is noticed after which a decrease follows again (Figure 10). The 0.001, 0.002, 0.004, and 0.008 rpm velocity segment show very regular stick slip behavior with a maximum stress drop of 0.419. At higher velocities, the shear stress becomes larger and no more shear stress drops can be examined. Only for the slowest velocities, enough data points are available to determine reliable b-values. Those vary between 0.5 and 3.9 (e.g. Figure 61), but have relative small R^2 values, not greater than 0.919. Recurrence time for the stress drops seem to cluster in one specific areas or on a certain line (Figure 62).

More than 1000 acoustic emissions were determined for all velocities with the exception of 0.001 rpm. b-values determined show some significant variations with very low R^2 values (Figure 63). The R^2 values do not improve substantially when a minimum or maximum cut-off is used. On top of that, the distribution of acoustic emissions throughout every single velocity controlled experiment is very irregular (Figure 64). Periods with no acoustic emissions are being alternated with periods with lots of acoustic emissions, because of that, periods in which 10% of the acoustic emissions are recorded show substantial variation (Figure 65).

When the pre-stress drop is plotted against the next stress drop, the shear stress drop might plot on a line or in a specific areas (Figure 66). However, when this is done for the acoustic emissions, more than one single cluster forms (Figure 67).

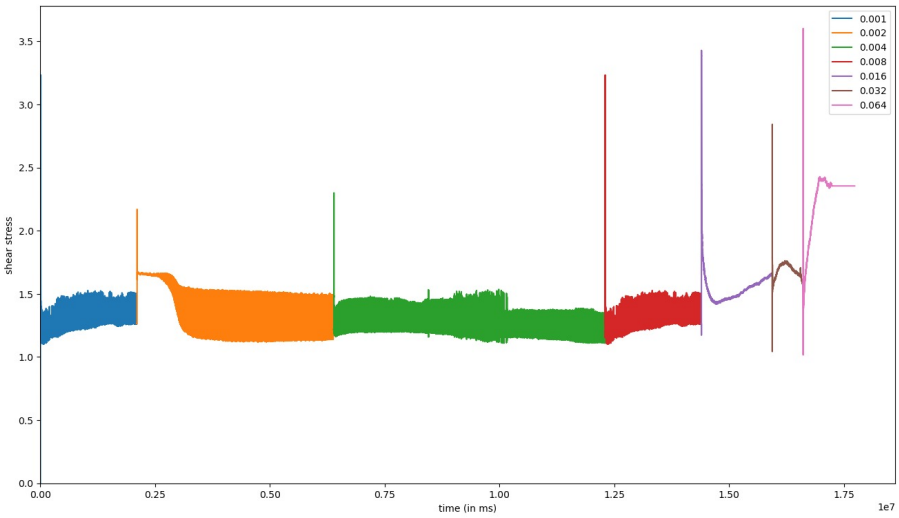

Figure 10: NaCl experiment with shear stress drops.

6.4.2 Experiment r365

Experiment r365 is performed under the same conditions as experiment r363. Also during this experiment, rotation was stopped after each velocity segment, with the exception after velocity segment 0.001 rpm. After the start of the rotation, it can be seen that the shear stress increases to about the same values as the ones that were observed in experiment r363. However, after this, a gradual decrease during the 0.001 and 0.002 rpm velocity segment is observed after which a sharp drop can be seen at the start of the 0.004 rpm experiment. Shear stress drops that exceed the threshold can only be determined during the velocities 0.004 rpm, 0.008 rpm, and 0.016 rpm, with a maximum of 0.516 MPa for the 0.004 rpm velocity segment (Figure 11). The recurrence time for the stress drops seems to cluster in one specific area or on a certain line (Figure 68). b-values for the shear stress drops data show some variations between 0.573 and 2.175 and have relatively small R^2 values (Figure 69).

More than 1000 median acoustic emissions were only recorded for the velocities greater or equal than 0.004 rpm. Maximum acoustic emissions tend to decrease with increasing velocity. For the b-values of the acoustic emissions, they tend to vary quite significant between 0.658 and 4.844 for median and 0.465 and 4.529 for maximum (Figure 70) with relatively small R^2 values associated. On top of that, the distribution of acoustic emissions throughout every single velocity controlled experiment is very irregular. Periods with no acoustic emissions are being alternated with periods with lots of acoustic emissions, and periods with small acoustic emissions sizes are being alternated with periods with large acoustic emission sizes. b-value through time varies therefore significant (Figure 71).

When plotting the pre-stress drop against the next stress drop, the shear stress drops exhibit a linear trend (Figure 72). However, when performing the same analysis for the acoustic emissions, multiple distinct clusters appear (Figure 73).

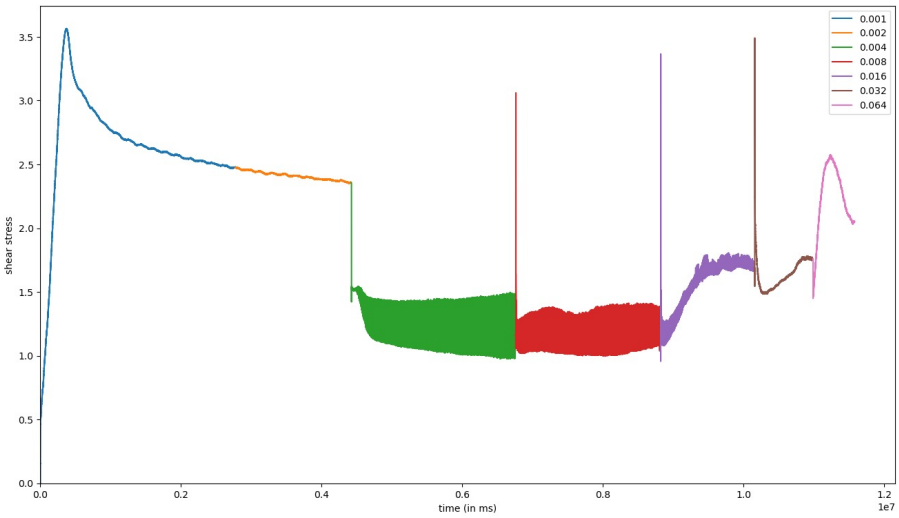

Figure 11: NaCl experiment with shear stress drops.

7 Discussion

This thesis seeks to understand the distribution of earthquakes that occur as a result of laboratory-induced conditions in the rotary shear apparatus. The focus is on earthquakes specifically generated or simulated within the controlled environment of the rotary shear apparatus.

For all the experiments, there is a direct initial increase in shear stress to a specific value, after which a pattern of shear stress drops starts to form for specific materials, including glass beads, gypsum and NaCl. During an experiment, the height of these shear stress drops might significantly in- or decrease indicating that strain hardening and softening can be observed.

Generally applies to the glass beads that the shear stress sharply increases after the start of the rotation. For the glass beads experiments, the maximum reached shear stress varies between about 2.2 and 3.2 MPa. After the rotation started, a direct increase to about this maximum value might occur, while other glass beads experiments show a more gradual increase or reach the maximum shear stress at faster velocities. The maximum shear stress can remain almost constant during the whole experiment, while gradual or sudden in- or decreases might appear. The maximum friction values for this experiment vary therefore between about 0.3 and 0.4 and are very similar to values obtained during experiments in the ring shear apparatus (Korkolis et al., 2021), but also in a biaxial testing apparatus (Johnson et al., 2013). The shear stress drops in glass beads, that happen after the breakage of a force chain (Scuderi et al., 2014), vary per experiment and can become smaller or bigger per experiment and per velocity. All of the stress drops were partial; the shear stress never became zero during the experiment. For the glass beads experiments, the largest shear stress drops took place during the first part of the experiment, when the glass beads are sheared at the slowest velocity (0.001 rpm), consistent with Bolton et al. (2021). However, it does not show a decreasing trend, as it suggested by Bolton et al. (2021) (Bolton et al., 2021). The only exception is experiment r353. During this experiment, the largest shear stress drop is recorded when sheared at 0.004 rpm. In experiment r348 and partially experiment r341, the shear stress envelope becomes narrower during the experiment, which is independent on the velocities. However, other glass beads experiments do not show this feature. Johnson et al. (2008) states that the maximum stress drop is about 10-30% of the maximum shear stress during experiments performed under constant shearing (Johnson et al., 2008). This is not completely in line with the data found during these experiments as the maximum stress drops are relatively much smaller and never reach about 30% of the maximum shear stress that was obtained during the experiment. The maximum shear stress drop is recorded in experiment r348 at the 0.001 rpm velocity (Table

1) and is about 20% of the maximum shear stress. On top of this, during other velocity segments, the maximum shear stress drop does not even exceed 5% of the maximum shear stress. All the stress drops in the glass beads are accompanied with an acoustic emission, despite the fact that it is sometimes difficult to actually correlate the shear stress drop to an acoustic emission due to the background noise in the data set. However, the time of occurrence for the stress drop and the acoustic emissions are not synchronous; the stress drops are, just as for the NaCl experiment, before the acoustic emission. This is not in line with Jiang et al. (2009) and Jiang et al. (2017) whose results state that the acoustic emissions including the largest ones predate the stress drop (X. Jiang et al., 2009; Y. Jiang et al., 2017). For the experiments in this thesis, the largest acoustic emissions are not necessarily related to the largest stress drops, which is also in contrast to Bolton et al. (2021) (Bolton et al., 2021). The only periods of quiescence for the acoustic emissions are related to stress build ups. However, also during these stress build ups, acoustic emissions, that are possibly precursors, can be recorded. The amount of acoustic emissions recorded tend to become more when the shear stress almost reaches failure. Johnson et al. (2013) suggest that those precursors are prior to a large earthquake (stress drop) and associated with a microslip. These microslips can be attributed to the grain rearrangements within the shearing layer (Johnson et al., 2013). These grain rearrangements observed can be attributed to the resistance of glass beads during slow slip by the formation of force chains (Y. Jiang et al., 2017). This resistance leads to local failures, generating precursors, and ultimately resulting in a catastrophic failure in the form of a large stick-slip event (Ferdowsi et al., 2014). In addition, Lei & Ma (2014) suggested that the acoustic emission data is related to certain phases: primary, secondary, nucleation, dynamic, aftershock, and stick-slip phases in the experiment, which can be established by looking at the acoustic emission data (Lei and Ma, 2014). However, such trend cannot be observed in the acoustic emissions for glass beads.

For gypsum, shear stress drops only form during the period to the maximum shear stress, until the maximum shear stress reaches 6 MPa and the friction is equal to 0.75. This friction value is quite low compared to Poppe et al. (2021) who state that their friction value for gypsum powder is 0.96±0.008 (Poppe et al., 2021). When this value is reached, no further shear stress drops were recognized and the shear stress started to decrease. Barberini et al. (2005) states that after the maximum shear stress was reached during a shear experiment at 127°C and various pressures, the shear stress dropped with a value of about 30-40% (Barberini et al., 2005). This did not happen during these experiments in the rotary shear apparatus, despite the fact that also after reaching the maximal shear stress a decrease was noticeable. However, as velocity is increased during the experiment, it is impossible to say to what extent this decrease might have continued. The movement of gypsum under 8 MPa normal stress with velocities ranging from 0.001 to 0.032 rpm appears to be mainly attributed to stable sliding, consistent with earlier findings (Muhuri et al., 2003) However, according to Xu et al. (2022), environmental changes such as variations in temperature, water content or humidity could affect the properties of gypsum. Especially when exposed to water, the internal microstructure of gypsum rock undergoes damage, leading to a corresponding deterioration in its mechanical properties (Xu et al., 2022). This might potentially lead to (greater) stress drops and associated acoustic emissions (Muhuri et al., 2003).

For KCl, friction initially increased to about 0.5 and remained at about 0.45 for the whole experiment. No shear stress drops were recognized throughout the experiment with the exception of the ones right after the start of the shearing. These shear stress drops are accompanied by an acoustic emission, but the correlation between the acoustic emission to the shear stress drop is complex. Because of the changes between none to a lot of acoustic emissions in a very short period of time, it is expected that KCl can switch between stick slip behavior and stable sliding on a very short time scale. This might be due to the change in chemical reaction in KCl while being sheared, as Betteridge et al. (1981) showed that acoustic emissions might be omitted when shearing a solution of solid hydrogen carbonate and KCl (Betteridge et al., 1981). Further, the fault healing of KCl is remarkable. After the storage of the data, a significant barrier must be overcome before KCl goes back to the shear stress value before the storage of the data. This might be related to dynamic recrystallisation or static recrystallisation (Ohl et al., 2020) or to thermally activated mechanisms

that weld back the asperity contacts on the surface of the fault (McLaskey et al., 2012).

As for NaCl, the initial increase to about 3.2 or 3.5 MPa is considerably lower than predicted by Bos & Spiers (2002) at 8 MPa normal pressure (Bos and Spiers, 2002), after which a sudden decrease might occur, dependent on the velocity. The stress drops that occur have a linear build up, which suggests that no precursors prior to the shear stress drops have taken place. For the acoustic emissions, the highest AE are being recorded almost directly after the maximum stress drop, as well as the smaller acoustic events. Also for salt, the shear stress drop will come first, after which an acoustic emission signal is recorded. The acoustic emission that follows right after a stress drop is not necessarily the largest one and is in most of the cases followed by one or multiple other acoustic emissions. However, as can be seen in experiment r363 with velocity 0.001 rpm, not all stress drop are necessarily accompanied by an acoustic emission. During this velocity segment, over 10.000 shear stress drops were recorded while no more than 84 acoustic emissions were observed. On the other hand, when the velocity was increased to a specific value, no stress drops were recorded anymore. Therefore, in these experiments, the velocity was crucial for the stability of the fault motion, as is also shown by Shimamoto (1986) (Shimamoto, 1986). Other researchers have shown that, during experiments on salt, progressively disappearing stick-slip regime can eventually go into a stable sliding regime with accumulative displacement (Chester, 1988; Voisin et al., 2005). Acoustic emissions on the other hand were still recorded. Explanations for this might be related to volume decreases or to the type of cracks responsible for the producing of the acoustic emissions (Alkan et al., 2007; Manthei, 2005).

7.1 Gutenberg-Richter or characteristic earthquake model?

For the determination of a b-value for a specific material, enough determined shear stress drops or acoustic emissions should be available. The larger the data set, the more precise the estimation of the b-value in a certain region will be (Geffers et al., 2022). Therefore, we use as much data points as possible, but at least 1000 for the best representation of the b-value to limit the error (Chernick, 1999), however, smaller data sets for the determination of b-values were used as well (Dong et al., 2022; Shi and Bolt, 1982). When data sets are greater than 1000 data points, they are considered to be reliable enough to make a distinction between the different frequency-magnitude distribution. Moreover, the goodness of the fit (R^2 value) can be used to evaluate the fitting reliability of the determined b-values (Dong et al., 2022; X. Ma et al., 2018). To proclaim that a specific b-value is reliable enough for a specific material at a specific velocity, an R^2 value of at least 0.95 is used before considering it to be a reliable Gutenberg-Richter frequency-magnitude distribution. Therefore, the only materials in which reliable b-values were observed are the acoustic emissions of the glass beads and the KCl experiments. In a perfect set-up, the median, as well as the maximum b-value should give approximately the same value and show the same trend in between the different velocities and experiments. However, the b-value of the median and maximum are in the majority of the cases not equal to each other and the trend sometimes behaves differently. Suggested is that this is because the b-values of the maximum acoustic emission size are related to one or two specific acoustic emission sensors (i.e. the ones with the largest AE sizes). However, the median acoustic emission value levels out all the points and is better for tendencies because it gives the center of the data set as it neglects outliers. On top of that, median acoustic emissions have, in the great majority of the glass beads experiment, higher R^2 values with respect to the b-value determined for the maximum acoustic emissions and never drop below 0.975. Drawback is that the median acoustic emission also must surpass the threshold. If this does not happen, the amount of data points of the median acoustic emission size might be (significantly) lower compared to the amount of data points from the maximum acoustic emission size.

The b-values that were obtained during the KCl experiments are relatively high when compared to the glass beads experiments. Those b-values vary between 2.6 and 3.0 for maximum and between 3.0 and 6.0 for median acoustic emissions (all with R^2 values greater than 0.98). b-values for nature are significantly smaller and normally vary around 0.9-1.0 (Jenatton et al., 2007)(UTSU, 1972), just as the b-values in volcanic active regions, where they are between 1 and 2 due to the length

and slenderness of the faults (Rundle, 1989). Also friction experiments from shallow volcanic regions show that b-values are not expected to exceed 2-3 (Berg, 1968). Therefore, KCl is not representative for any material on Earth in which earthquakes are likely to nucleate and because of this, KCl is not a representative analog for earthquake behavior. b-values for the acoustic emissions of glass beads on the other hand, that vary between 0.5 and 1.8 come much closer to values that can be expected in nature. The range of b-values determined in nature is between 0.45 and 1.8 (Köhler et al., 2009), which is very similar to the b-values found for glass beads. Further, experiments on rocks, such as granites, showed that during triaxial shear experiments, b-values from acoustic emission data ranges between 1-2 (Dong et al., 2022) and, in addition, multi-level cyclic loading testing also shows that b-values from acoustic emission range from about 0.7 to 2.2 for granites (Wang et al., 2021). Because of this, glass beads might be a representative analog for faults observed in nature.

When looked at the shear stress drops from the NaCl data, enough data points were collected for specific velocities to say something about the frequency magnitude distribution that should be present in this material. As mentioned, the shear stress drops in the NaCl experiment consist of an almost linear build up to the point of where the shear stress drops occur. During this period, no pre-shocks or pre-acoustic emissions can be observed. When looked at all the velocity segments, some experiments showed b-values with R^2 that are high enough to be considered to correspond to a reliable b-value. However, when looked at other AE sensors, R^2 values are low and by looking at the histograms, this tendency is doubtful as specific peaks at specific AE sizes can be observed. Maghsoudi et al (2014). also showed that b-values in a salt mine range from 1.5 to 2.81, but the acoustic emissions data from this salt mine shows deviations from the Gutenberg-Richter behavior as well (Maghsoudi et al., 2014). Explanations for this might be related to the inactive period before the formation of macro fractures or to the period of fracture growth (Köhler et al., 2009). As mentioned, not all the different shear stress drops or acoustic emission sizes cluster at the same size (e.g. Figure 66), making it unlikely to state that NaCl behaves as a characteristic earthquake model on the long time scale. However, on the short time scale, so only during parts of the velocity segments, NaCl does seem to produce earthquakes that behave in a way similar to the characteristic earthquake model. Therefore, suggested is that NaCl behaves on short term in a way similar to the characteristic earthquake model, while does not show a Gutenberg-Richter, nor characteristic earthquake model on the long term. This is in contrast to other author who do state that the frequency magnitude distribution of salt can be described by the Gutenberg-Richter model, sometimes with extremely high b-values (Köhler et al., 2009; Lei et al., 2019).

Due to the limited number of data points for shear stress drops and acoustic emissions, it is not possible to draw any conclusions about the frequency-magnitude distribution for gypsum. The experiment did not yield sufficient data points for shear stress or acoustic emissions to derive a representative value for the b-value. The movement of gypsum under 8 MPa normal stress with velocities ranging from 0.001 to 0.032 rpm appears to be mainly attributed to stable sliding, consistent with other findings (e.g. Muhuri et al., 2003). Further, Leclère et al. (2016) suggest that stick-slips in gypsum mostly occur at slower velocities, higher confining pressures and on the completion of the dehydration reaction of gypsum (Leclère et al., 2016).

7.2 Effect of velocity on the b-value

Only the b-values determined for the acoustic emission of glass beads and KCl are assumed to be reliable, as they have enough data points and the R^2, exceeds 0.95. The data display that there is an inverse relationship between velocity and the b-value for the relative bigger grain sizes. The experiments r330, r346 and r348, with a grain size larger than 300 µm, show an overall decreasing trend for the median as well as the maximum b-value with increasing velocity. The median and maximum b-values are for some of the smallest velocities more or less equal to each other and only start notably decreasing at the faster velocities, especially for the smallest grain size experiments, while the largest grain size experiments show a more stepwise decrease in b-value between the different velocities. The median and maximum b-values from experiment r341, the experiment

with the smallest grain size, do not show a real trend. They tend to in- and then decrease with increasing velocity. Moreover, experiment r353, that started with the fastest velocity and ended with the slowest velocity, shows the same inverse relationship as determined for the larger grain sizes; an increase for b-value with decreasing velocity. This rules out that an increase in b-value can solely be attributed to grain size reduction or increased grain size distribution. I would therefore suggest that the velocity has an inverse influence on the behavior of the b-value, which relationship was also established by Bolton et al. (2021) but is in contrast to Nishikawa & Ide (2014), as they state that the b-value only has a weakly correlation with the convergence rate and the upper plate velocity (Bolton et al., 2021; Nishikawa and Ide, 2014).

KCl on the other hand shows an increasing trend for the maximum b-value with increasing velocity. However, this trend can only be observed in the maximum b-value as the median deviates much more. On top of that, the differences between the determined maximum b-values are fairly small and the b-value for only four velocities were determined. Therefore, the influence of velocity on the b-value of KCl might be based on a coincidence.

7.3 Effect of grain size

As can be seen for the glass beads, the slowest velocities have the highest shear stress drops. When the velocity is increased, the shear stress drops decrease, which is in line with Mair et al. (2002) (Mair et al., 2002). This might suggest that the slowest velocity is responsible for the largest shear stress drops in glass beads. However, when the velocity is decreased during the experiment, the shear stress drop for the slowest velocity is not the largest anymore (Table 1). Suggested is therefore that not only velocity, but also the grain size distribution might have an influence on the size of a shear stress drop (Korkolis et al., 2021). During experiments at 8 MPa, the glass beads break and crumble and the angularity of the new grains will make them even more vulnerable to breakage (Klaas et al., 2005; Yan and Shi, 2014). Therefore, particle size distribution will increase, just as the shear stress (Fulton and Rathbun, 2011). A different consequence of the increase in particle size distribution, is that the shear stress drops will become smaller as smaller particle size distributions exhibit unstable stick slip behavior, while a larger distribution of particles will rather display stable sliding (Mair et al., 2002). This is because the energy releases during the stick-slips are larger as the particles will roll along each other, while angular particles face hindrance to rolling and will slide more to accommodate the strain (Fulton and Rathbun, 2011). No explanation however could be given for the sudden large stress drops that can be determined at the end of some experiments (e.g. r330 or r333). However, these phenomena have been observed more often in similar experiments (e.g. p1964 (Niemeijer et al., 2010)).

7.4 Comparison with natural seismicity

First of all, faults in nature behave in a more complex way than faults in a confined space in the laboratory. Tectonic fault zones consist of numerous subfaults, making predictions considerably more difficult. Although precursors are often detected in laboratory studies, their reliable observation in natural faults remains uncertain. On top of that, seismic cycles in the Earth on a larger scale are significantly slower (Lubbers et al., 2018). More parameters in the laboratory need to be considered as well, including: pore fluids, temperature, and chemical processes (Korkolis et al., 2021 and references therein). Furthermore, a fault is never comprised of the same material with a specific grain size nor with round grain shapes (Mair et al., 2002). Faults in nature might show changes in b-value that can be attributed to an upcoming large earthquake (e.g. El-Isa and Eaton, 2014; Hirata, 1989; SHI et al., 2018). However, the results of this study do not substantiate these findings. Important is to note that changes in b-value also happen per velocity segment. On top of that, we cannot see a relationship between an in- or decrease of the b-value of the median acoustic emission and the pattern of large shear stress drops during the different velocity segments. However, the amount of acoustic emissions do seem to increase as a stress drops is coming. These b-values are considered to be reliable as R^2 values remain often (much) greater than 0.95 and as

precisely 1000 data points were used for the determination. b-value changes during the seismic cycle were observed in other experiments as well. Rivière et al. (2018) for example shows that their b-values vary between 1.0 and 1.8 during a 4 MPa experiment using a double-direct shear configuration (Rivière et al., 2018). However, these changes are significantly larger than the ones that were found during these experiments, were they tend to vary no more than about 10% with respect to the b-value determine for the full experiment.

Sudden increases in velocity might be expected in nature, when a fault undergoing slow slip becomes unstable or when an earthquake rupture front comes from elsewhere (S. Ma et al., 2014). Our results therefore suggest that significant changes in b-value can definitely be observed when this might happen.

7.5 Limitations

This research is subject to potential limitations, which could introduce biases and confounding factors that might have influenced the model outputs. The majority of these limitations can be attributed to the experimental set-up and data processing part.

Possible issues may have arisen during the leveling process of the material in the annular cavity and ensuring uniform leveling of the sample. In cases where the leveling was not done accurately, a specific section of the sample might have received a disproportionate amount of normal stress, leading to an increased pressure on those grains while leaving another part of the sample relatively untouched. This uneven distribution of stress within the material could have affected the experimental results and subsequently impacted the model outputs.

Additionally, there are variations or discrepancies among sensors, leading to differences in their output amplitudes even when triggered by the same stimulus. This lack of consistency can be attributed to various factors, including manufacturing tolerances, environmental conditions, or sensor calibration issues. The placement of these sensors involves positioning them into holes in both the upper and lower piston, until they touch the end of the hole and are in close proximity to the sample (about 5 mm). However, this process is manually executed, leading to variations in the distance of the acoustic emission sensors from the material. Consequently, the amplitudes of individual events may exhibit considerable differences due to these variations in sensor placement. This inconsistency in sensor positioning hinders the direct comparison of amplitudes between different sensors and experiments. Moreover, since the triggered sensor is mostly selected based on one of the highest amplitudes recorded, there is a possibility that events surpassing the 0.005 V threshold on other sensors may go unnoticed if they fail to surpass the threshold on the triggered sensor. These limitations in the installation and positioning of the acoustic emission sensors can introduce uncertainties in the recorded data, potentially influencing the accuracy and comparability of the results. Implementing more standardized and precise methods for sensor placement could enhance the reliability and consistency of the acoustic emission data.

Moreover, a brief initial run was conducted to ensure the proper placement of the sample and functioning of the apparatus. During this preliminary phase, some small stress drops and acoustic emissions were observed but were not included in the analysis. As this is essential for a further smooth progress of the experiment, it is difficult to improve on this. However, Korkolis et al. (2021) states that a pre-compaction phase before an experiment is needed, making any potential effects from this phase are likely to be minimal (Korkolis et al., 2021).

The accurate determination of the trigger time is crucial for calculating the recurrence time between shear stress drops and acoustic emissions. If the trigger time is too short, it may result in recording the same event multiple times, leading to different values for the recurrence time between two acoustic emissions and potentially develop a bias towards only the largest magnitude earthquakes, as they were selected as the characteristic amplitude. As a result, the b-values could exhibit significant differences, given the increased influence of larger earthquakes or acoustic emissions in the dataset. However, if the trigger time is too long, the smallest events might not be

recorded at all, also having a bias towards more large shear stress drops and acoustic emissions in the dataset. To avoid such biases and ensure robust analysis, it is of crucial importance to set an appropriate trigger time that effectively distinguishes between individual acoustic emissions. By carefully selecting the trigger time, that might vary per experiment, it is possible to obtain a more accurate representation of the recurrence time distribution and to determine b-values to a higher precision.

It is crucial to acknowledge these limitations to ensure a comprehensive understanding of the experimental outcomes and to explore ways to improve on frequency-magnitude distribution for materials that can be used as analogs for earthquakes in nature. Addressing and minimizing these limitations would be crucial to enhance the validity and reliability of these research findings. Careful attention to the experimental procedures, particularly in terms of proper leveling and stress distribution, could help reduce potential biases and enhance the overall robustness of the study.

7.6 Future research

As there is no consensus on the minimum number of data points required to obtain a reliably accurate frequency-magnitude distribution, uncertainty remains about the accuracy of the current b-value calculation. This is critical considering the need for a significant number of shear stress drops, not only in the laboratory, but also in nature, to minimize the over- or underestimation of the b-value (Geffers et al., 2022). In light of this, it becomes crucial to emphasize the point when a b-value can be considered as truly reliable.

To see what the influence of the grain size distribution is on frequency-magnitude distributions, more experiments are needed. It cannot be said with certainty, solely based on this research, if the influence of the grain size distribution on the change in b-value is greater or smaller for the relative smaller grain sizes and to what extent. Moreover, it cannot be said with certainty if the smallest velocity is responsible for the highest magnitude shear stress drops or if the grain size distribution plays also a crucial role in this.

To gain deeper insights into the behavior of materials under various experimental conditions, which are also prevalent in natural settings, such as temperature, pressure, and fluid interactions, it is essential to conduct further data collection and analysis. Also exploring the effects of these different environmental factors and their influence on stress drops and acoustic emissions would contribute significantly to comprehensively understanding the Earth's material's behavior.

8 Conclusion

The objective of this research is to investigate the frequency-magnitude distribution of earthquakes induced in the laboratory. To address this question, multiple experiments were conducted in the Earth Simulation Laboratory, utilizing the rotary shear apparatus. Subsequent data analysis was carried out to gain insights into the distribution patterns.

The findings reveal that different materials exhibit distinct types of unstable or stick-slip behavior, resulting in varying frequency-magnitude distributions for both shear stress drops and acoustic emissions. Glass beads and KCl, when sheared with the rotary shear apparatus, display a strong tendency to exhibit Gutenberg-Richter behavior in their acoustic emissions. This behavior is possibly also shown by the shear stress drops of glass beads. However, the results for NaCl are different, showing characteristic earthquake behavior only during specific time periods and only for specific velocities for the shear stress drops, while no clear frequency-magnitude distribution can be attributed to its acoustic emissions. As for the shear stress drops of gypsum and KCl, and the acoustic emissions of gypsum, the data collected did not provide enough information to draw conclusive observations. Therefore, no definitive conclusions can be made for these materials.

The effect of velocity on the frequency-magnitude distribution on the acoustic emissions can be seen on the larger grain sizes for the glass beads, the median and maximum b-values of the acoustic emission data has a preference to decrease with increasing velocity, as also is the case for the b-value of the maximum acoustic emission data of the KCl. With sudden increasing velocity, decreasing steps in b-value can clearly be observed. For NaCl on the other hand, increasing velocity seems to have an influence on the transition between stick-slip behavior to stable sliding behavior.

The influence of grain size distribution on frequency magnitude distribution remains yet enigmatic. Especially as this only could be established in glass beads. It is very difficult to actually attribute sizes of stress drops or acoustic emissions and changes in b-value to changes in grain size. Results suggest that grain size distribution might have an influence on the size of the shear stress drops and acoustic emissions. However, other factors, including velocity changes and changes in internal structure, might play a role as well.

It can be further concluded that labquake experiments are a very simple version of earthquakes, as the conditions in the lab are significantly different compared to the ones that can be found in nature, including things such as time scale, variations in pressure, temperature and fluid content. However, to determine frequency-magnitude distributions and its behavior, it is the ideal way to do it, as thousands of labquakes can be generated in a relative short time span of only a couple of hours. On top of that, particles in a rotary shear apparatus experience same orders of normal stress, similar to the ones that can be found in the lithosphere, and the intermittent nature of deformation, with periods of activity followed by periods of relative quiescence is also similar to stress-build ups in nature.

The enhancements made in earthquake characteristics, including a better understanding of frequency-magnitude distributions, b-value, and the sizes of shear stress drops and acoustic emissions, along with its relationship to velocity changes and grain size distribution hold the potential to improve probability seismic hazard analysis. By even further refining these parameters, the ability to assess and mitigate earthquake risks can be significantly improved.

References

Abaimov, S., Turcotte, D., Shcherbakov, R., Rundle, J. B., Yakovlev, G., Goltz, C., & Newman, W. I. (2008). Earthquakes: Recurrence and interoccurrence times. *Earthquakes: Simulations, Sources and Tsunamis*, 777–795.

Alkan, H., Cinar, Y., & Pusch, G. (2007). Rock salt dilatancy boundary from combined acoustic emission and triaxial compression tests. *International Journal of Rock Mechanics and Mining Sciences*, *44*(1), 108–119.

Barberini, V., Burlini, L., Rutter, E., & Dapiaggi, M. (2005). High-strain deformation tests on natural gypsum aggregates in torsion. *Geological Society, London, Special Publications*, *245*(1), 277–290.

Benabdallah, H., & Aguilar, D. (2008). Acoustic emission and its relationship with friction and wear for sliding contact. *Tribology Transactions*, *51*(6), 738–747.

Ben-Zion, Y., Eneva, M., & Liu, Y. (2003). Large earthquake cycles and intermittent criticality on heterogeneous faults due to evolving stress and seismicity. *Journal of Geophysical Research: Solid Earth*, *108*(B6).

Berg, E. (1968). Relation between earthquake foreshocks, stress and mainshocks. *Nature*, *219*(5159), 1141–1143.

Betteridge, D., Joslin, M. T., & Lilley, T. (1981). Acoustic emissions from chemical reactions. *Analytical Chemistry*, *53*(7), 1064–1073.

Bollinger, L., Avouac, J., Cattin, R., & Pandey, M. (2004). Stress buildup in the himalaya. *Journal of Geophysical Research: Solid Earth*, *109*(B11).

Bolton, D. C., Shreedharan, S., Rivière, J., & Marone, C. (2021). Frequency-magnitude statistics of laboratory foreshocks vary with shear velocity, fault slip rate, and shear stress. *Journal of Geophysical Research: Solid Earth*, *126*(11), e2021JB022175.

Bos, B., & Spiers, C. J. (2002). Frictional-viscous flow of phyllosilicate-bearing fault rock: Microphysical model and implications for crustal strength profiles. *Journal of Geophysical Research: Solid Earth*, *107*(B2), ECV–1.

Budnitz, R., Apostolakis, G., & Boore, D. M. (1997). *Recommendations for probabilistic seismic hazard analysis: Guidance on uncertainty and use of experts* (tech. rep.). US Nuclear Regulatory Commission (NRC), Washington, DC (United States). Div ...

Chernick, M. R. (1999). Bootstrap methods: A practitioner's guide. *(No Title)*.

Chester, F. M. (1988). The brittle-ductile transition in a deformation-mechanism map for halite. *Tectonophysics*, *154*(1-2), 125–136.

Dahmen, K., Ertaş, D., & Ben-Zion, Y. (1998). Gutenberg-richter and characteristic earthquake behavior in simple mean-field models of heterogeneous faults. *Physical Review E*, *58*(2), 1494.

Doanh, T., & Nguyên, T. (2023). Unexpected departure from seismic laws with largest labquakes on model granular materials. *Soil Dynamics and Earthquake Engineering*, *172*, 108010.

Dong, L., Zhang, L., Liu, H., Du, K., & Liu, X. (2022). Acoustic emission b value characteristics of granite under true triaxial stress. *Mathematics*, *10*(3), 451.

Dragicevic, S., Filipovic, D., Kostadinov, S., Ristic, R., Novkovic, I., Zivkovic, N., Andjelkovic, G., Abolmasov, B., Secerov, V., & Djurdjic, S. (2011). Natural hazard assessment for land-use planning in serbia.

Dzierma, Y., Thorwart, M., Rabbel, W., Siegmund, C., Comte, D., Bataille, K., Iglesia, P., & Prezzi, C. (2012). Seismicity near the slip maximum of the 1960 mw 9.5 valdivia earthquake (chile): Plate interface lock and reactivation of the subducted valdivia fracture zone. *Journal of Geophysical Research: Solid Earth*, *117*(B6).

El-Isa, Z. H., & Eaton, D. W. (2014). Spatiotemporal variations in the b-value of earthquake magnitude–frequency distributions: Classification and causes. *Tectonophysics*, *615*, 1–11.

Elliott, J. (2020). Earth observation for the assessment of earthquake hazard, risk and disaster management. *Surveys in geophysics*, *41*(6), 1323–1354.

Ferdowsi, B., Griffa, M., Guyer, R. A., Johnson, P. A., Marone, C., & Carmeliet, J. (2014). Three-dimensional discrete element modeling of triggered slip in sheared granular media. *Physical Review E*, *89*(4), 042204.

Fulton, P. M., & Rathbun, A. P. (2011). Experimental constraints on energy partitioning during stick–slip and stable sliding within analog fault gouge. *Earth and Planetary Science Letters*, *308*(1-2), 185–192.

Galkina, A., & Grafeeva, N. (2019). Machine learning methods for earthquake prediction: A survey. *Proceedings of the Fourth Conference on Software Engineering and Information Management (SEIM-2019), Saint Petersburg, Russia*, *13*, 25.

Geffers, G., Main, I., & Naylor, M. (2022). Biases in estimating b-values from small earthquake catalogues: How high are high b-values? *Geophysical Journal International*.

Giardini, D., Grünthal, G., Shedlock, K. M., & Zhang, P. (1999). The gshap global seismic hazard map.

Gutenberg, B., & Richter, C. F. (1944). Frequency of earthquakes in california. *Bulletin of the Seismological society of America*, *34*(4), 185–188.

Harris, R. A. (2017). Large earthquakes and creeping faults. *Reviews of Geophysics*, *55*(1), 169–198.

Hirata, T. (1989). A correlation between the b value and the fractal dimension of earthquakes. *Journal of Geophysical Research: Solid Earth*, *94*(B6), 7507–7514.

Jenatton, L., Guiguet, R., Thouvenot, F., & Daix, N. (2007). The 16,000-event 2003–2004 earthquake swarm in ubaye (french alps). *Journal of Geophysical Research: Solid Earth*, *112*(B11).

Jiang, X., Shu-chun, L., Yun-qi, T., Xiao-jun, T., & Xin, W. (2009). Acoustic emission characteristic during rock fatigue damage and failure. *Procedia Earth and Planetary Science*, *1*(1), 556–559.

Jiang, Y., Wang, G., & Kamai, T. (2017). Acoustic emission signature of mechanical failure: Insights from ring-shear friction experiments on granular materials. *Geophysical Research Letters*, *44*(6), 2782–2791.

Johnson, P. A., Ferdowsi, B., Kaproth, B. M., Scuderi, M., Griffa, M., Carmeliet, J., Guyer, R. A., Le Bas, P.-Y., Trugman, D. T., & Marone, C. (2013). Acoustic emission and microslip precursors to stick-slip failure in sheared granular material. *Geophysical Research Letters*, *40*(21), 5627–5631.

Johnson, P. A., Savage, H., Knuth, M., Gomberg, J., & Marone, C. (2008). Effects of acoustic waves on stick–slip in granular media and implications for earthquakes. *Nature*, *451*(7174), 57–60.

Kagan, Y. (1993). Statistics of characteristic earthquakes. *Bulletin of the Seismological Society of America*, *83*(1), 7–24.

Klaas, N., Marcus, K., & Kellock, C. (2005). The tribological behaviour of glass filled polytetrafluoroethylene. *Tribology International*, *38*(9), 824–833.

Köhler, N., Spies, T., & Dahm, T. (2009). Seismicity patterns and variation of the frequency-magnitude distribution of microcracks in salt. *Geophysical Journal International*, *179*(1), 489–499.

Korkolis, E. (2017). *Rotary shear experiments on glass bead aggregates: Stick-slip statistics and parallels with natural seismicity*.

Korkolis, E., Niemeijer, A. R., Paulssen, H., & Trampert, J. (2021). A laboratory perspective on the gutenberg-richter and characteristic earthquake models. *Journal of Geophysical Research: Solid Earth*, *126*(8), e2021JB021730.

Leclère, H., Faulkner, D., Wheeler, J., & Mariani, E. (2016). Permeability control on transient slip weakening during gypsum dehydration: Implications for earthquakes in subduction zones. *Earth and Planetary Science Letters*, *442*, 1–12.

Lei, X., & Ma, S. (2014). Laboratory acoustic emission study for earthquake generation process. *Earthquake Science*, *27*, 627–646.

Lei, X., Wang, Z., & Su, J. (2019). Possible link between long-term and short-term water injections and earthquakes in salt mine and shale gas site in changning, south sichuan basin, china. *Earth and Planetary Physics*, *3*(6), 510–525.

Lomnitz, C. (1964). Estimation problems in earthquake series. *Tectonophysics*, *1*(2), 193–203.
Lubbers, N., Bolton, D. C., Mohd-Yusof, J., Marone, C., Barros, K., & Johnson, P. A. (2018). Earthquake catalog-based machine learning identification of laboratory fault states and the effects of magnitude of completeness. *Geophysical Research Letters*, *45*(24), 13–269.
Ma, S., Shimamoto, T., Yao, L., Togo, T., & Kitajima, H. (2014). A rotary-shear low to high-velocity friction apparatus in beijing to study rock friction at plate to seismic slip rates. *Earthquake Science*, *27*, 469–497.
Ma, X., Westman, E., Slaker, B., Thibodeau, D., & Counter, D. (2018). The b-value evolution of mining-induced seismicity and mainshock occurrences at hard-rock mines. *International Journal of Rock Mechanics and Mining Sciences*, *104*, 64–70.
Maghsoudi, S., Hainzl, S., Cesca, S., Dahm, T., & Kaiser, D. (2014). Identification and characterization of growing large-scale en-echelon fractures in a salt mine. *Geophysical journal international*, *196*(2), 1092–1105.
Mair, K., Frye, K. M., & Marone, C. (2002). Influence of grain characteristics on the friction of granular shear zones. *Journal of Geophysical Research: Solid Earth*, *107*(B10), ECV–4.
Manthei, G. (2005). Characterization of acoustic emission sources in a rock salt specimen under triaxial compression. *Bulletin of the Seismological Society of America*, *95*(5), 1674–1700.
Matsuzawa, T., Igarashi, T., & Hasegawa, A. (2002). Characteristic small-earthquake sequence off sanriku, northeastern honshu, japan. *Geophysical Research Letters*, *29*(11), 38–1.
McGarr, A. (1994). Some comparisons between mining-induced and laboratory earthquakes. *Pure and Applied Geophysics*, *142*(3-4), 467–489.
McLaskey, G. C., Thomas, A. M., Glaser, S. D., & Nadeau, R. M. (2012). Fault healing promotes high-frequency earthquakes in laboratory experiments and on natural faults. *Nature*, *491*(7422), 101–104.
Meghraoui, M., Aksoy, M. E., Akyüz, H. S., Ferry, M., Dikbaş, A., & Altunel, E. (2012). Paleoseismology of the north anatolian fault at güzelköy (ganos segment, turkey): Size and recurrence time of earthquake ruptures west of the sea of marmara. *Geochemistry, Geophysics, Geosystems*, *13*(4).
Monterroso, D. A., & Kulhánek, O. (2003). Spatial variations of b-values in the subduction zone of central america. *Geofısica Internacional*, *42*(4), 575–587.
Muhuri, S. K., Dewers, T. A., Scott Jr, T. E., & Reches, Z. (2003). Interseismic fault strengthening and earthquake-slip instability: Friction or cohesion? *Geology*, *31*(10), 881–884.
Niemeijer, A., Marone, C., & Elsworth, D. (2010). Frictional strength and strain weakening in simulated fault gouge: Competition between geometrical weakening and chemical strengthening. *Journal of Geophysical Research: Solid Earth*, *115*(B10).
Niemeijer, A., Spiers, C., & Peach, C. (2008). Frictional behaviour of simulated quartz fault gouges under hydrothermal conditions: Results from ultra-high strain rotary shear experiments. *Tectonophysics*, *460*(1-4), 288–303.
Nishikawa, T., & Ide, S. (2014). Earthquake size distribution in subduction zones linked to slab buoyancy. *Nature Geoscience*, *7*(12), 904–908.
Ohl, M., Plümper, O., Chatzaras, V., Wallis, D., Vollmer, C., & Drury, M. (2020). Mechanisms of fault mirror formation and fault healing in carbonate rocks. *Earth and Planetary Science Letters*, *530*, 115886.
Perfettini, H., & Avouac, J.-P. (2004). Stress transfer and strain rate variations during the seismic cycle. *Journal of Geophysical Research: Solid Earth*, *109*(B6).
Poppe, S., Holohan, E. P., Rudolf, M., Rosenau, M., Galland, O., Delcamp, A., & Kervyn, M. (2021). Mechanical properties of quartz sand and gypsum powder (plaster) mixtures: Implications for laboratory model analogues for the earth's upper crust. *Tectonophysics*, *814*, 228976.
Poulos, A., de la Llera, J. C., & Mitrani-Reiser, J. (2017). Earthquake risk assessment of buildings accounting for human evacuation. *Earthquake Engineering & Structural Dynamics*, *46*(4), 561–583.

Rajabi, M. S., Taghaddos, H., & Zahrai, S. M. (2022). Improving emergency training for earthquakes through immersive virtual environments and anxiety tests: A case study. *Buildings*, *12*(11), 1850.

Riera, J. D., & Iturrioz, I. (2012). The gutenberg-richter and similar laws and their relation with numerical and experimental laboratory results. *15th World Conf. on Earth. Eng., Paper*, *5827*.

Rivière, J., Lv, Z., Johnson, P., & Marone, C. (2018). Evolution of b-value during the seismic cycle: Insights from laboratory experiments on simulated faults. *Earth and Planetary Science Letters*, *482*, 407–413.

Rouet-Leduc, B., Hulbert, C., Lubbers, N., Barros, K., Humphreys, C. J., & Johnson, P. A. (2017). Machine learning predicts laboratory earthquakes. *Geophysical Research Letters*, *44*(18), 9276–9282.

Rundle, J. B. (1989). Derivation of the complete gutenberg-richter magnitude-frequency relation using the principle of scale invariance. *Journal of Geophysical Research: Solid Earth*, *94*(B9), 12337–12342.

Săcuiu, I., & Zorilescu, D. (1970). Statistical analysis of seismic data on earthquakes in the area of the vrancea focus. *Bulletin of the Seismological Society of America*, *60*(4), 1089–1099.

Schwartz, D. P., & Coppersmith, K. J. (1984). Fault behavior and characteristic earthquakes: Examples from the wasatch and san andreas fault zones. *Journal of Geophysical Research: Solid Earth*, *89*(B7), 5681–5698.

Scuderi, M. M., Carpenter, B. M., & Marone, C. (2014). Physicochemical processes of frictional healing: Effects of water on stick-slip stress drop and friction of granular fault gouge. *Journal of Geophysical Research: Solid Earth*, *119*(5), 4090–4105.

SHI, H., MENG, L., ZHANG, X., CHANG, Y., YANG, Z., XIE, W., Hattori, K., & HAN, P. (2018). Decrease in b value prior to the wenchuan earthquake (m s 8.0). *Chinese Journal of Geophysics*, *61*(5), 1874–1882.

Shi, Y., & Bolt, B. A. (1982). The standard error of the magnitude-frequency b value. *Bulletin of the Seismological Society of America*, *72*(5), 1677–1687.

Shimamoto, T. (1986). Transition between frictional slip and ductile flow for halite shear zones at room temperature. *Science*, *231*(4739), 711–714.

Sianko, I., Ozdemir, Z., Khoshkholghi, S., Garcia, R., Hajirasouliha, I., Yazgan, U., & Pilakoutas, K. (2020). A practical probabilistic earthquake hazard analysis tool: Case study marmara region. *Bulletin of earthquake engineering*, *18*, 2523–2555.

Terchi, A., & Au, Y. (2001). Acoustic emission signal processing. *Measurement and Control*, *34*(8), 240–244.

Udias, A., Arroyo, A. L., & Mezcua, J. (1976). Seismotectonic of the azores-alboran region. *Tectonophysics*, *31*(3-4), 259–289.

UTSU, T. (1972). Aftershocks and earthquake statistics (3): Analyses of the distribution of earthquakes in magnitude, time and space with special consideration to clustering characteristics of earthquake occurrence (1). *Journal of the Faculty of Science, Hokkaido University. Series 7, Geophysics*, *3*(5), 379–441.

Utsu, T. (1974). A three-parameter formula for magnitude distribution of earthquakes. *Journal of Physics of the Earth*, *22*(1), 71–85.

Voisin, C., Renard, F., Grasso, J., & Stiers, F. (2005). Transition from stick-slip to stable sliding due to asperities aging: Experimental evidence on a simulated fault. *AGU Fall Meeting Abstracts*, *2005*, T21B–0471.

Wang, Y., Han, J., Song, Z., & Zhu, C. (2021). Macro-meso failure behavior of pre-flawed hollow-cylinder granite under multi-level cyclic loads: Insights from acoustic emission and post-test ct scanning. *Engineering Fracture Mechanics*, *258*, 108074.

Wesnousky, S. G. (1994). The gutenberg-richter or characteristic earthquake distribution, which is it? *Bulletin of the Seismological Society of America*, *84*(6), 1940–1959.

Wright, S., & Rathje, E. (2003). Triggering mechanisms of slope instability and their relationship to earthquakes and tsunamis. *Pure and Applied Geophysics*, *160*, 1865–1877.

Wu, K., Pizette, P., Becquart, F., Remond, S., Abriak, N., Xu, W., & Liu, S. (2017). Experimental and numerical study of cylindrical triaxial test on mono-sized glass beads under quasi-static loading condition. *Advanced Powder Technology*, *28*(1), 155–166.

Xu, X., Zhou, Y., Chen, W., Gao, Y., Fu, Q., Liu, X., & Feng, C. (2022). Macro-microscopic deterioration behavior of gypsum rock after wetting and its constitutive model based on acoustic emission. *Minerals*, *12*(9), 1168.

Yan, W., & Shi, Y. (2014). Evolution of grain grading and characteristics in repeatedly reconstituted assemblages subject to one-dimensional compression. *Géotechnique Letters*, *4*(3), 223–229.

Zhang, Y., Feng, X.-T., Yang, C., Zhang, X., Sharifzadeh, M., & Wang, Z. (2019). Fracturing evolution analysis of beishan granite under true triaxial compression based on acoustic emission and strain energy. *International Journal of Rock Mechanics and Mining Sciences*, *117*, 150–161.

Zöller, G. (2013). Convergence of the frequency-magnitude distribution of global earthquakes: Maybe in 200 years. *Geophysical Research Letters*, *40*(15), 3873–3877.

9 Appendix

9.1 Figures glass beads

9.1.1 Experiment r330

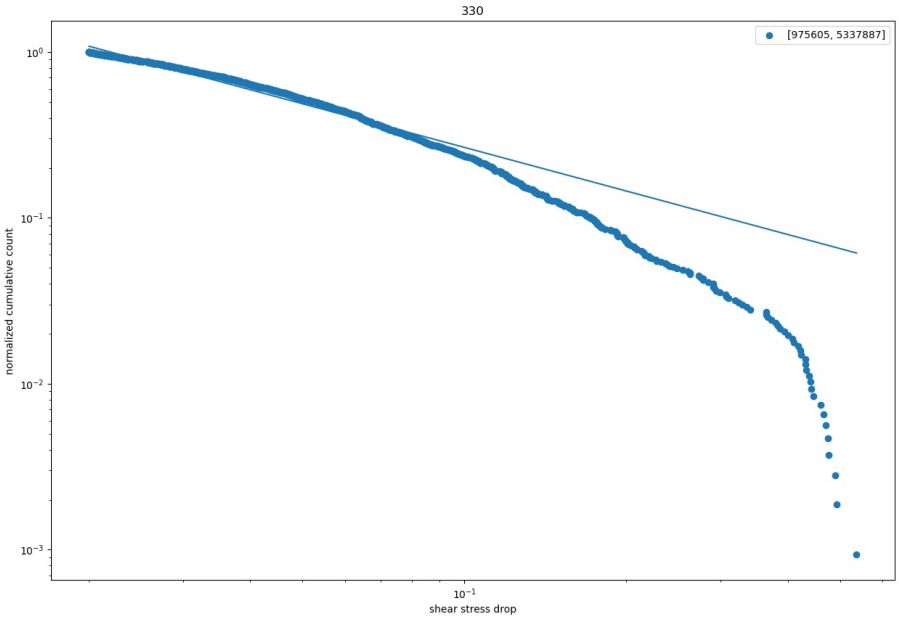

Figure 12: Glass beads experiment with b-value determined for shear stress drop data for velocity 0.001 rpm.

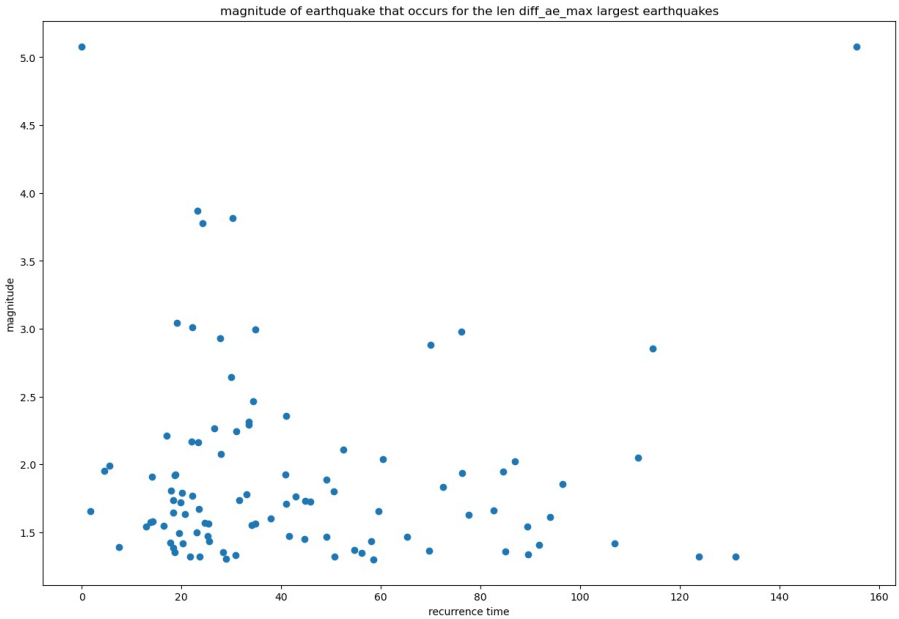

Figure 13: Glass beads experiment with recurrence time for shear stress drops for velocity 0.001 rpm.

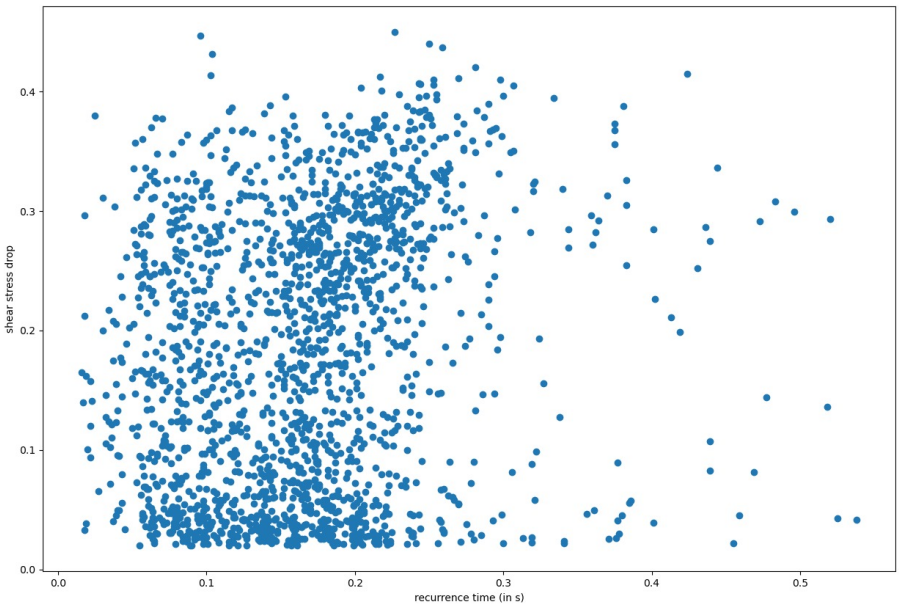

Figure 14: Glass beads experiment with recurrence time for shear stress drops for velocity 0.064 rpm.

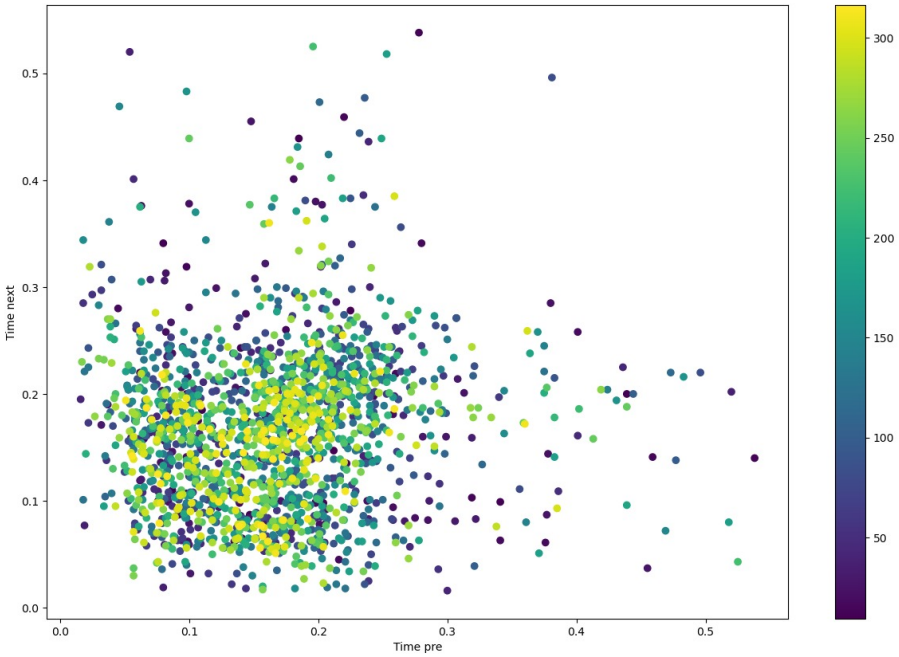

Figure 15: Glass beads experiment with time of pre- and next shear stress drop for velocity 0.064 rpm.

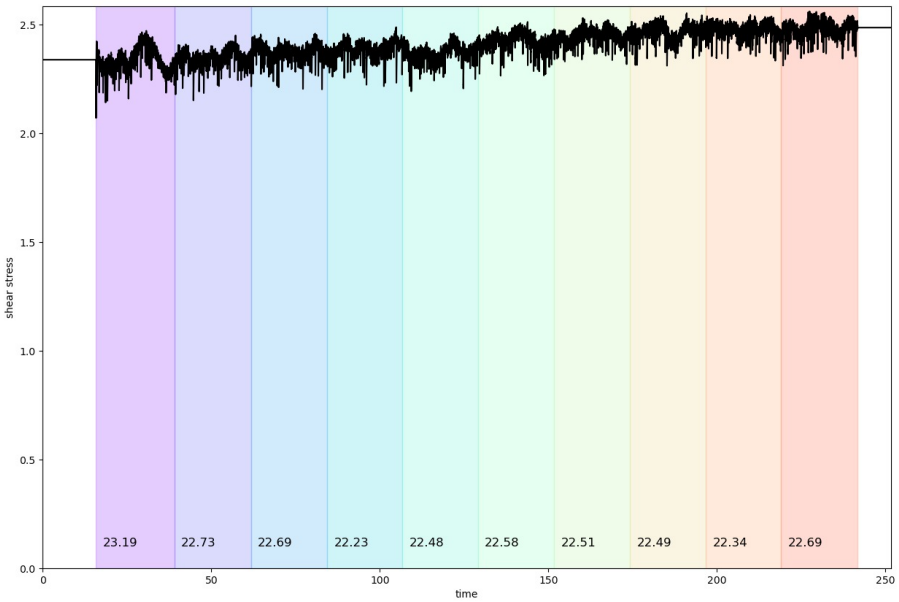

Figure 16: Glass beads experiment with 10% of the recorded acoustic emission data per colored column for velocity 0.064 rpm.

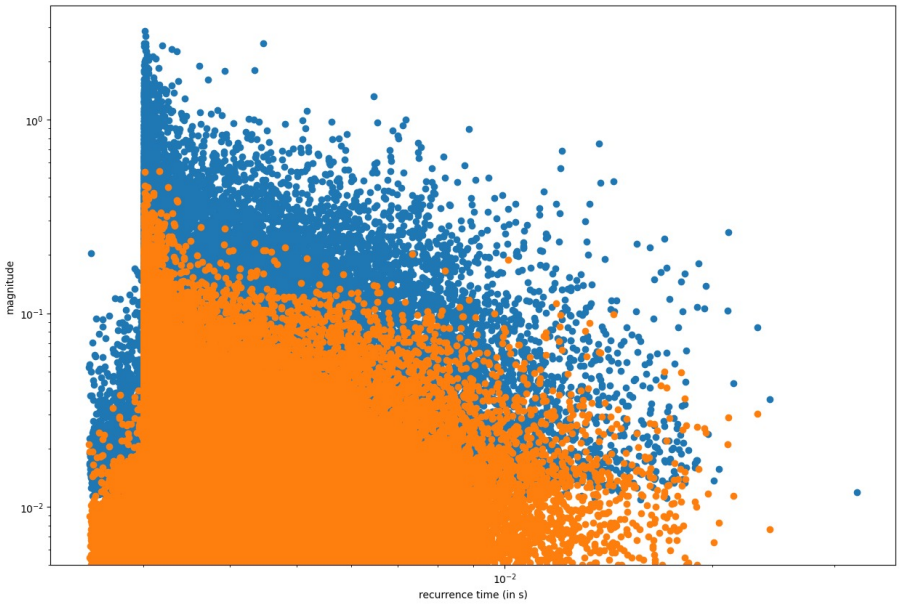

Figure 17: Glass beads experiment with recurrence time of median and maximum AE data for velocity 0.032 rpm.

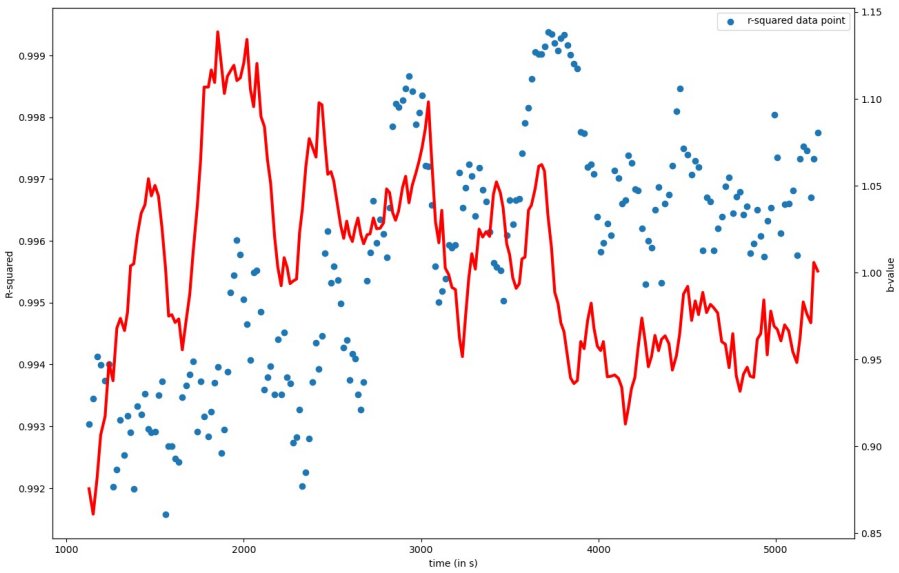

Figure 18: Glass beads experiment with median b-value through time along with R^2 for velocity 0.001 rpm.

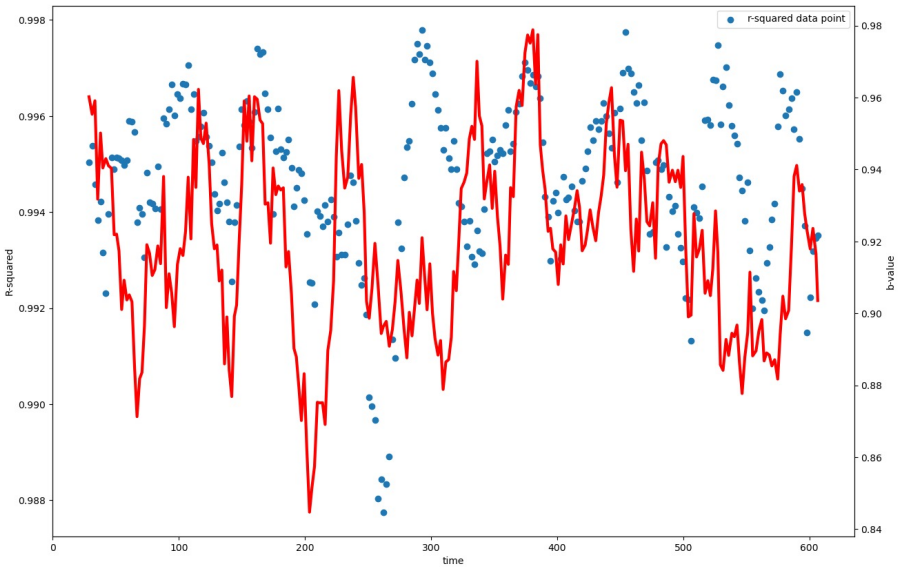

Figure 19: Glass beads experiment with median b-value through time along with R^2 for velocity 0.032 rpm.

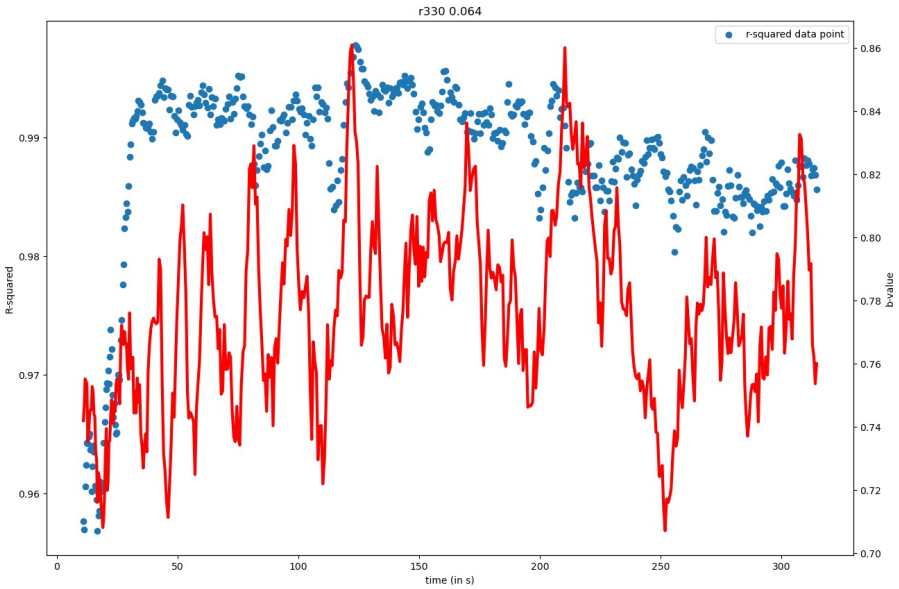

Figure 20: Glass beads experiment with median b-value through time along with R^2 for velocity 0.064 rpm.

9.1.2 Experiment r333

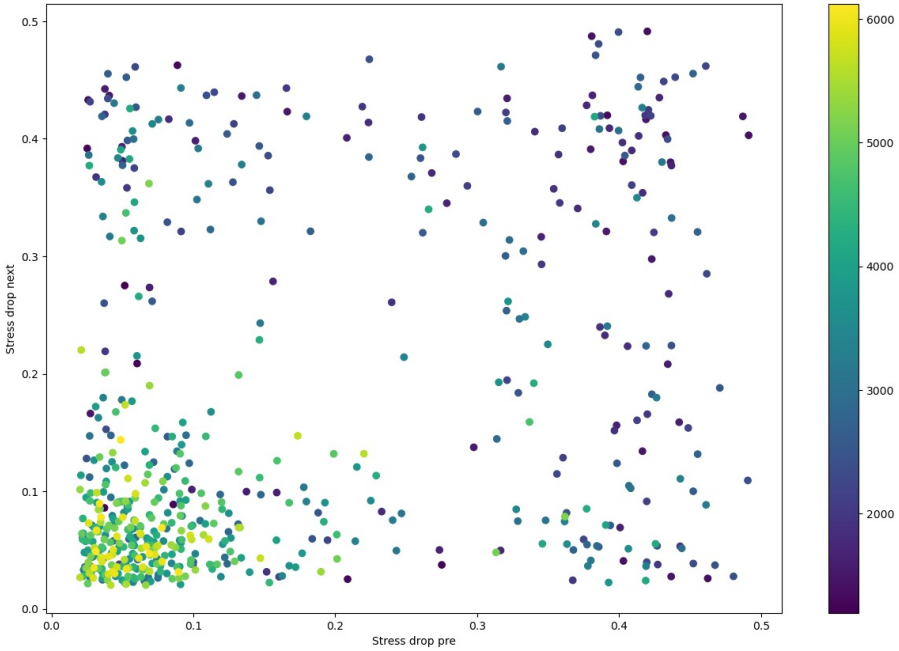

Figure 21: Glass beads experiment with pre- and next shear stress drop for velocity 0.001 rpm.

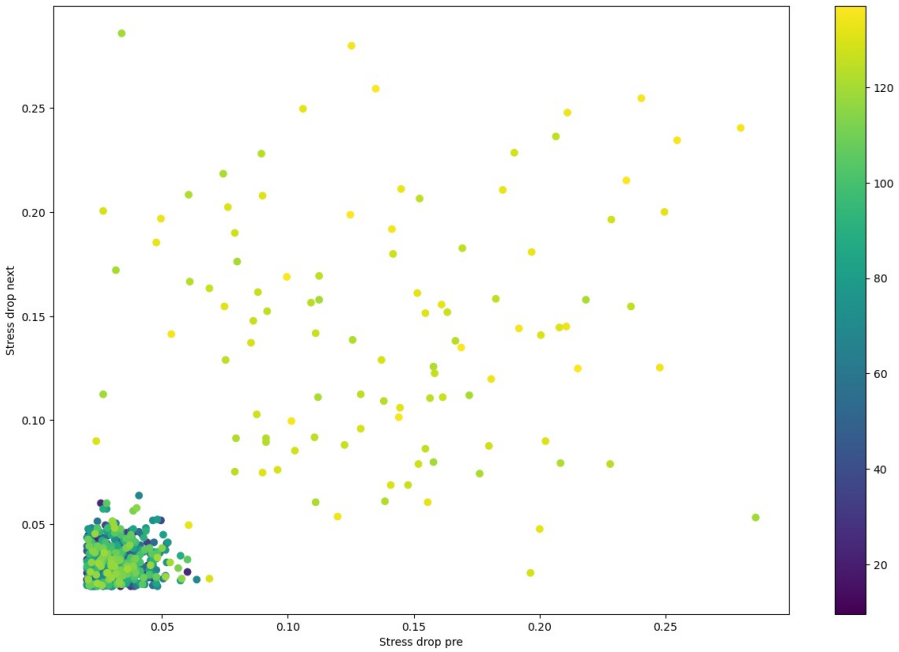

Figure 22: Glass beads experiment with pre- and next shear stress drop for velocity 0.064 rpm.

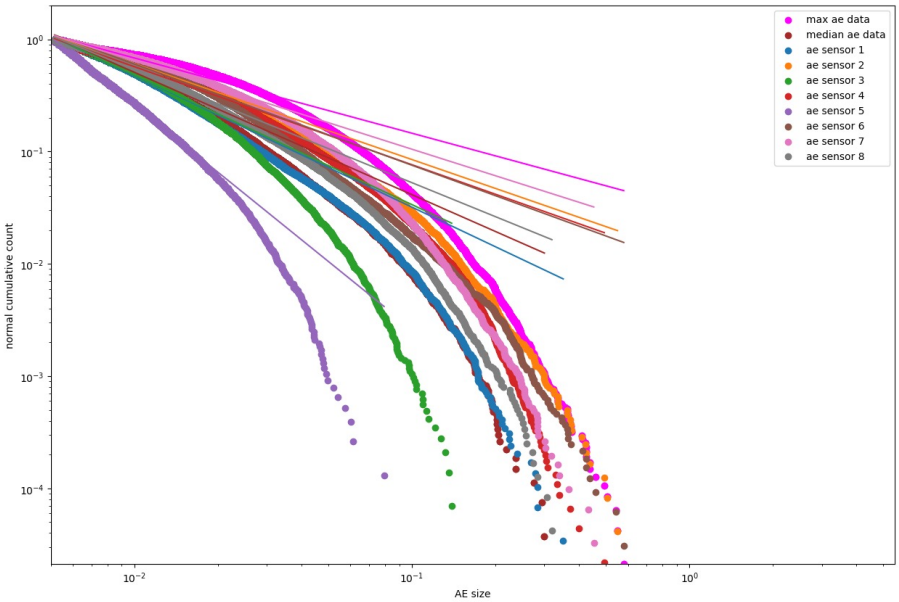

Figure 23: Glass beads experiment with b-value determined for AE data for velocity 0.008 rpm.

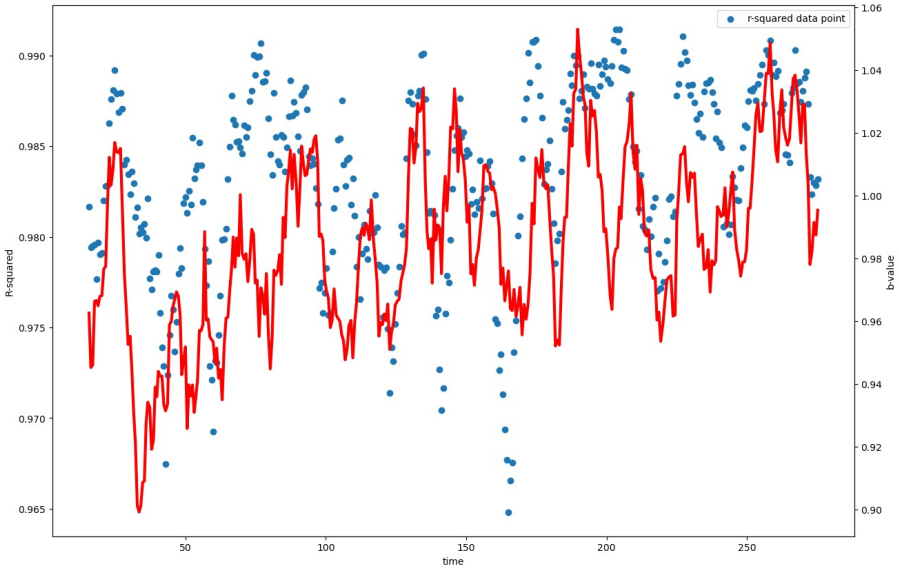

Figure 24: Glass beads experiment with median b-value through time along with R^2 for velocity 0.032 rpm.

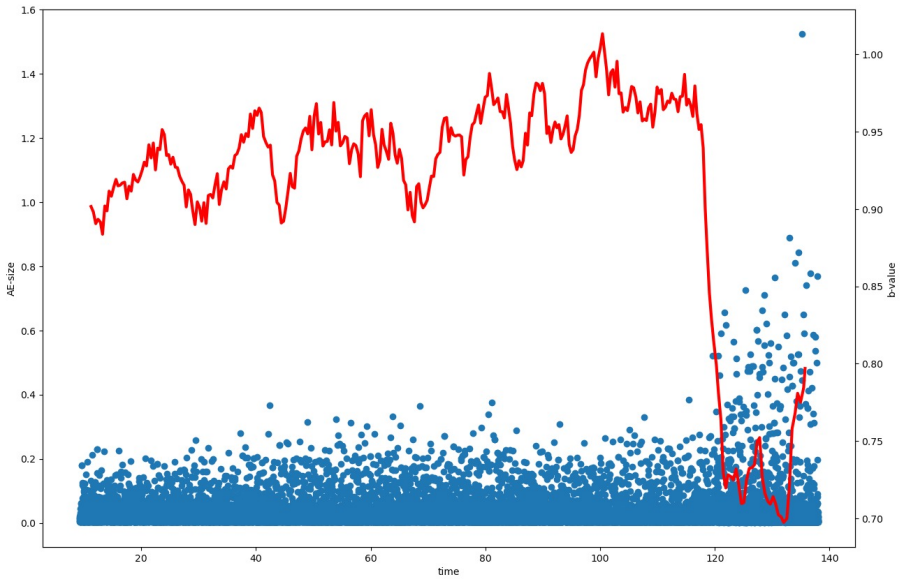

Figure 25: Glass beads experiment with median b-value through time along with median acoustic emissions for velocity 0.064 rpm.

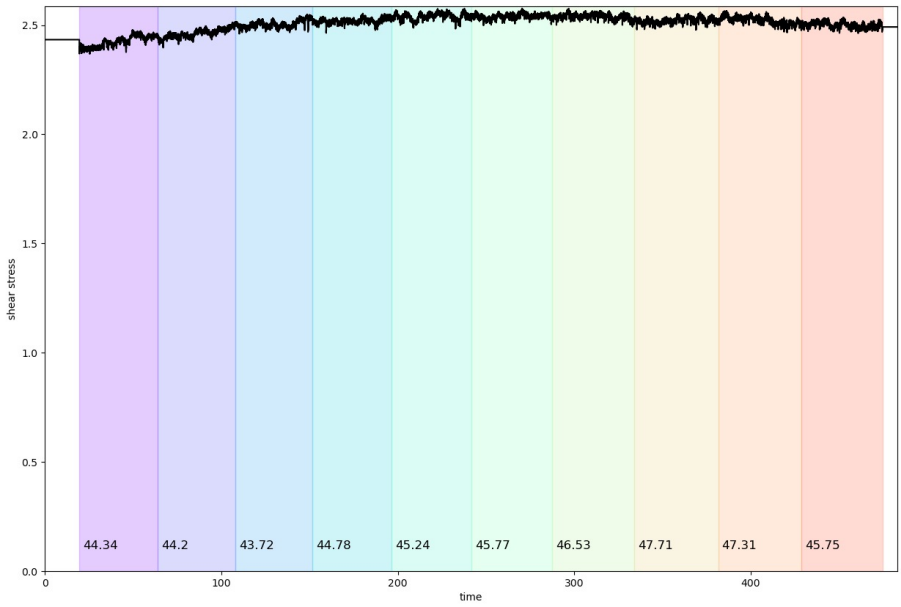

Figure 26: Glass beads experiment with 10% of the recorded acoustic emission data per colored column for velocity for velocity 0.016 rpm.

9.1.3 Experiment r341

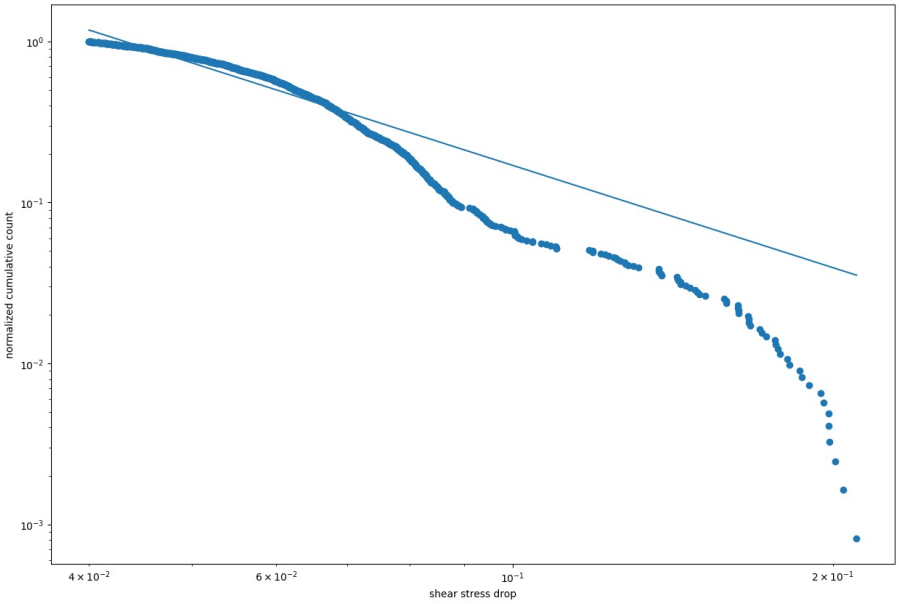

Figure 27: Glass beads experiment with b-value determined for shear stress drop data for velocity 0.064 rpm.

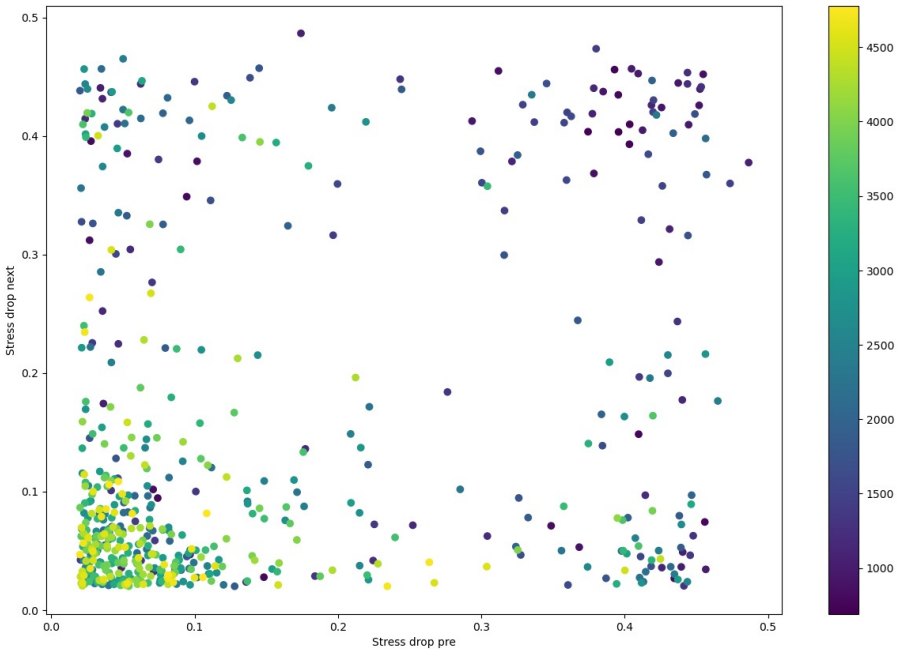

Figure 28: Glass beads experiment with pre- and next shear stress drop for velocity 0.001 rpm.

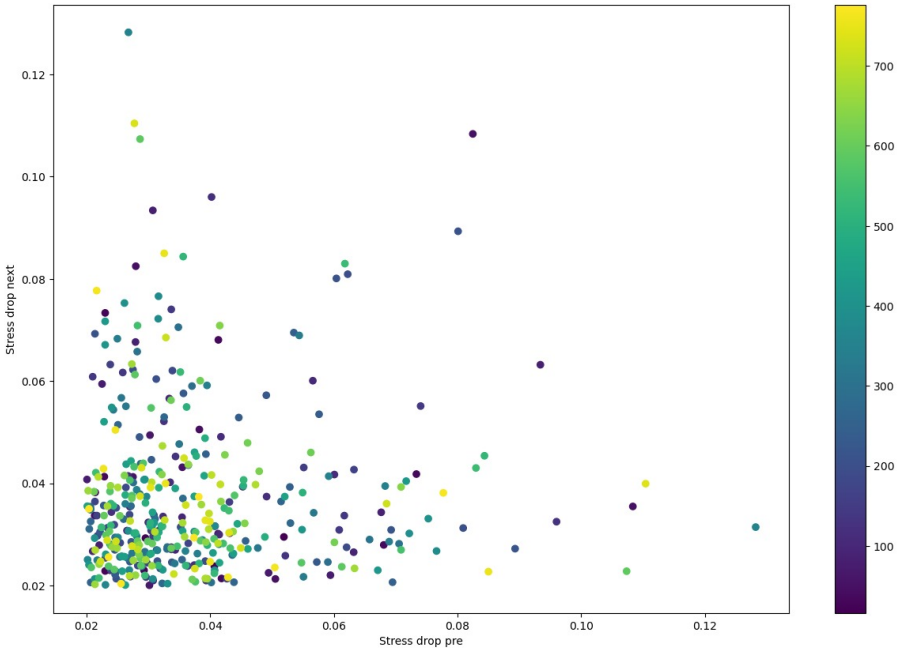

Figure 29: Glass beads experiment with pre- and next shear stress drop for velocity 0.004 rpm.

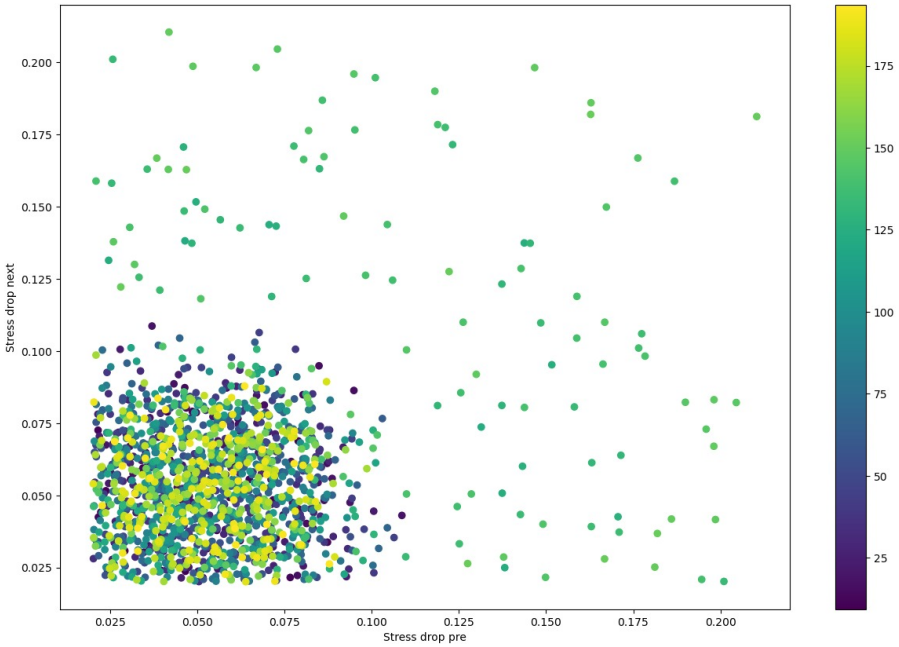

Figure 30: Glass beads experiment with pre- and next shear stress drop for velocity 0.064 rpm.

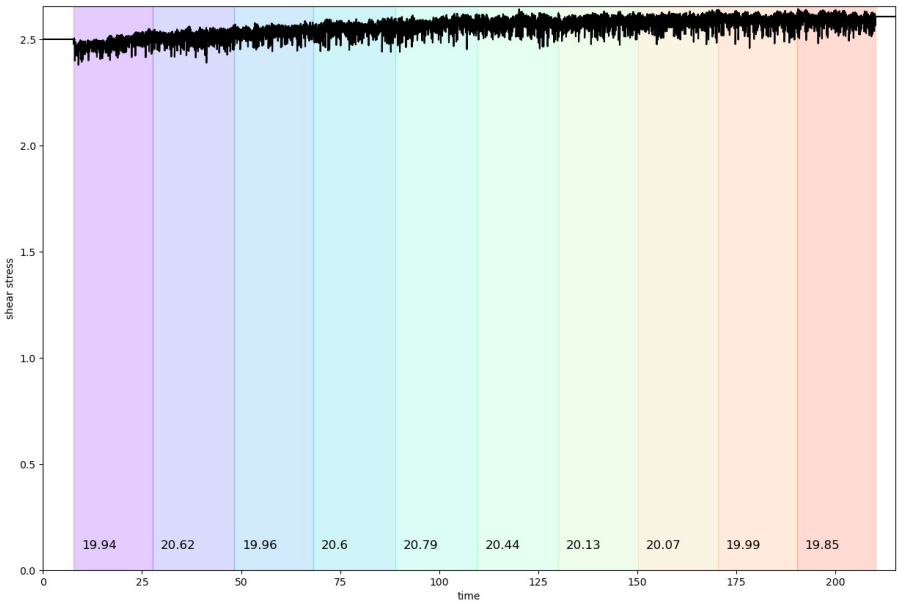

Figure 31: Glass beads experiment with 10% of the recorded acoustic emission data per colored column for velocity 0.032 rpm.

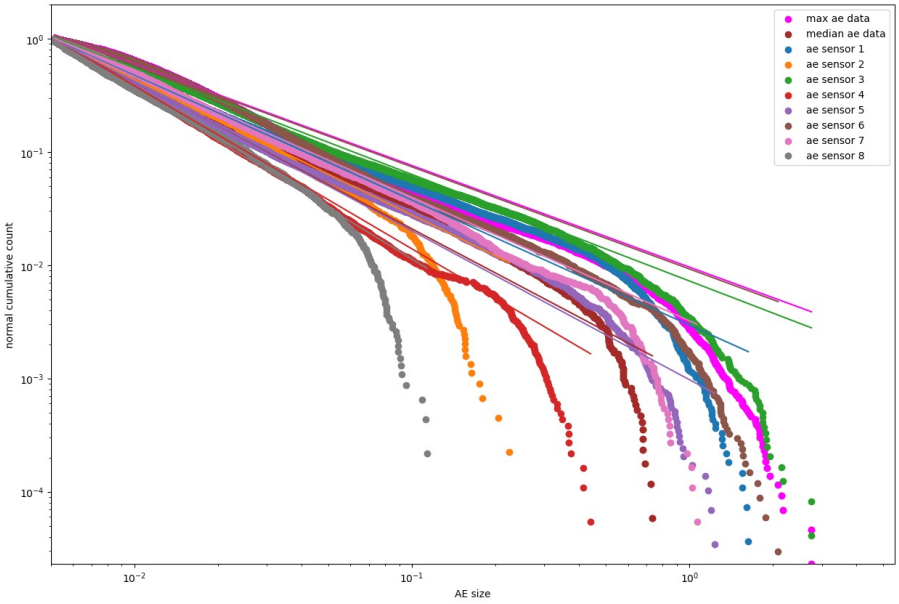

Figure 32: Glass beads experiment with b-value determined for AE data for velocity 0.001 rpm.

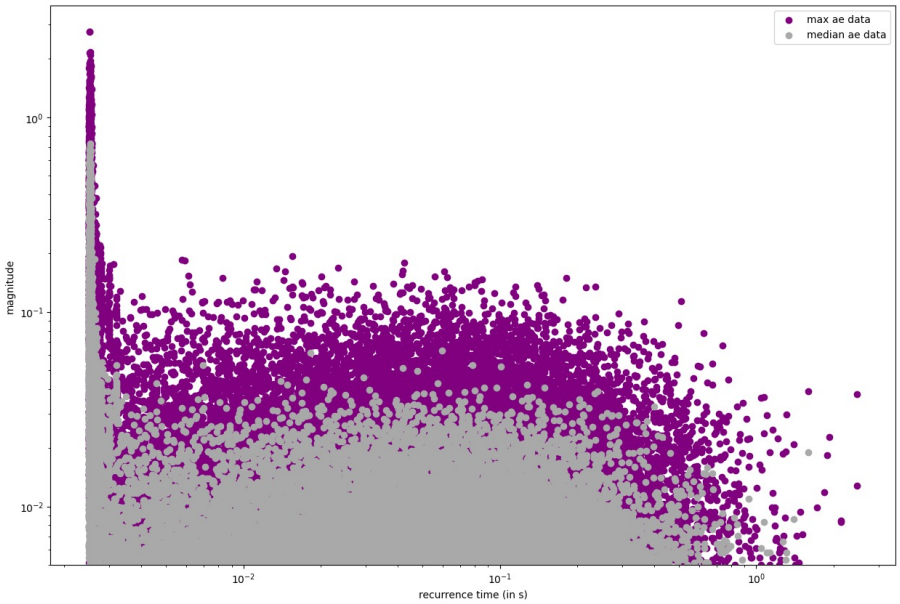

Figure 33: Glass beads experiment with recurrence time of median and maximum AE data for velocity 0.001 rpm.

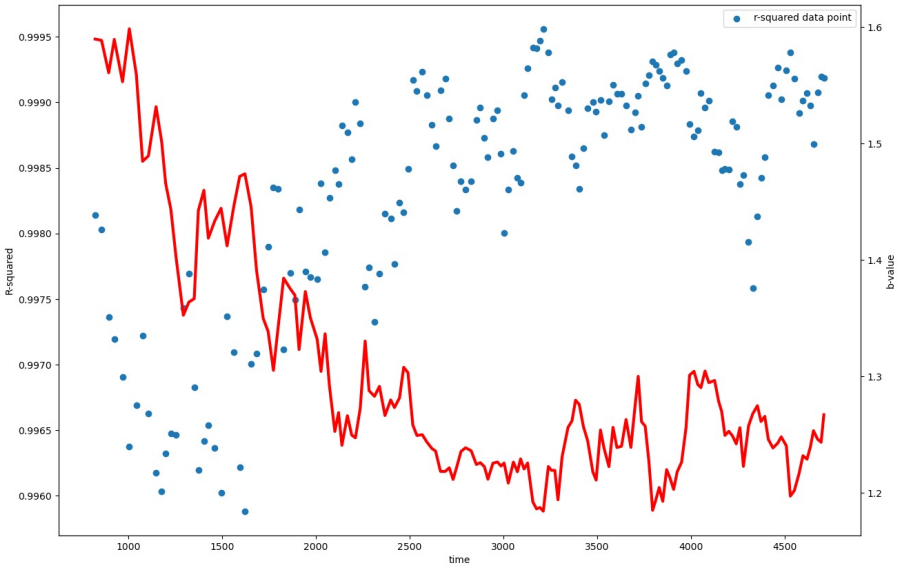

Figure 34: Glass beads experiment with median b-value through time along with R^2 for velocity 0.001 rpm.

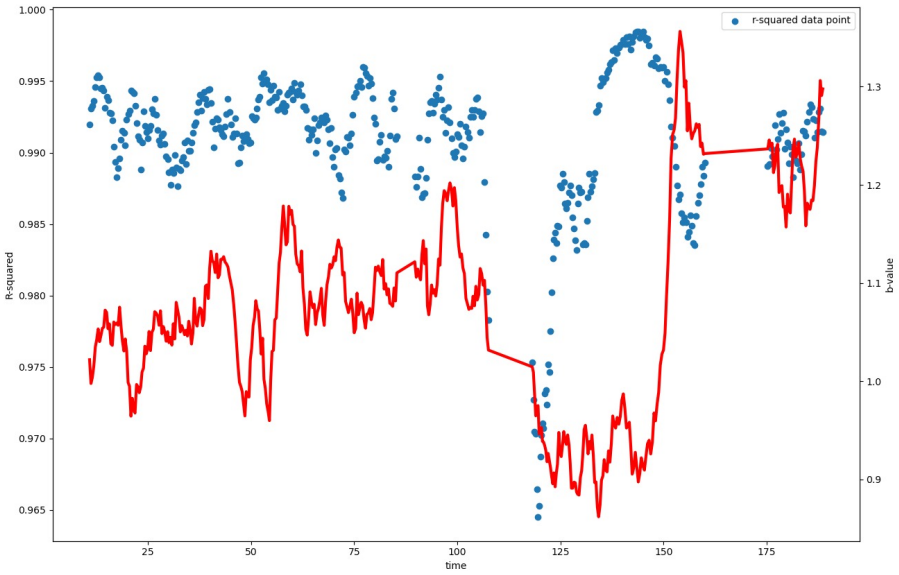

Figure 35: Glass beads experiment with median b-value through time along with R^2 for velocity 0.064 rpm.

9.1.4 Experiment r346

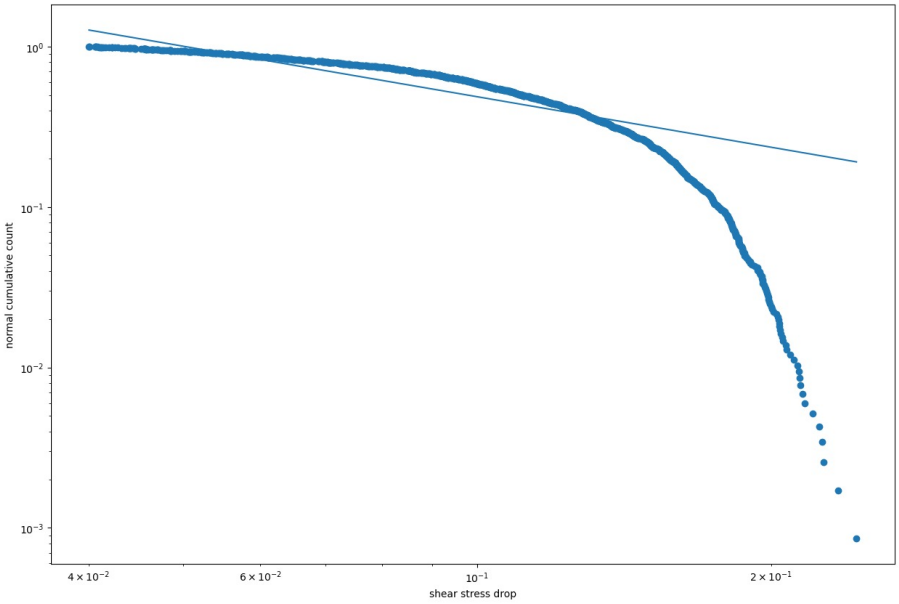

Figure 36: Glass beads experiment with b-value determined for shear stress drop data for velocity 0.064 rpm.

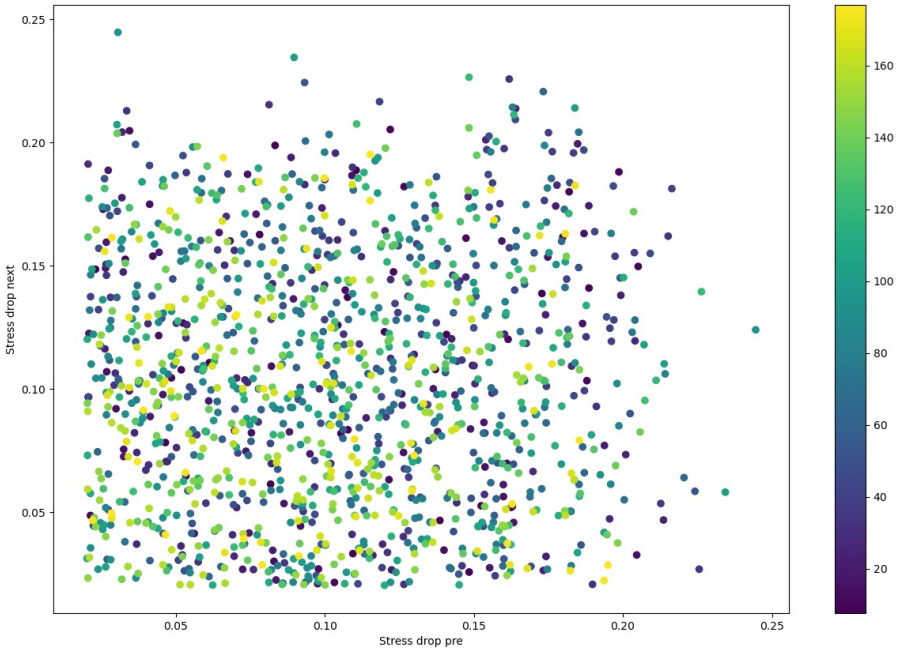

Figure 37: Glass beads experiment with pre- and next shear stress drop for velocity 0.064 rpm.

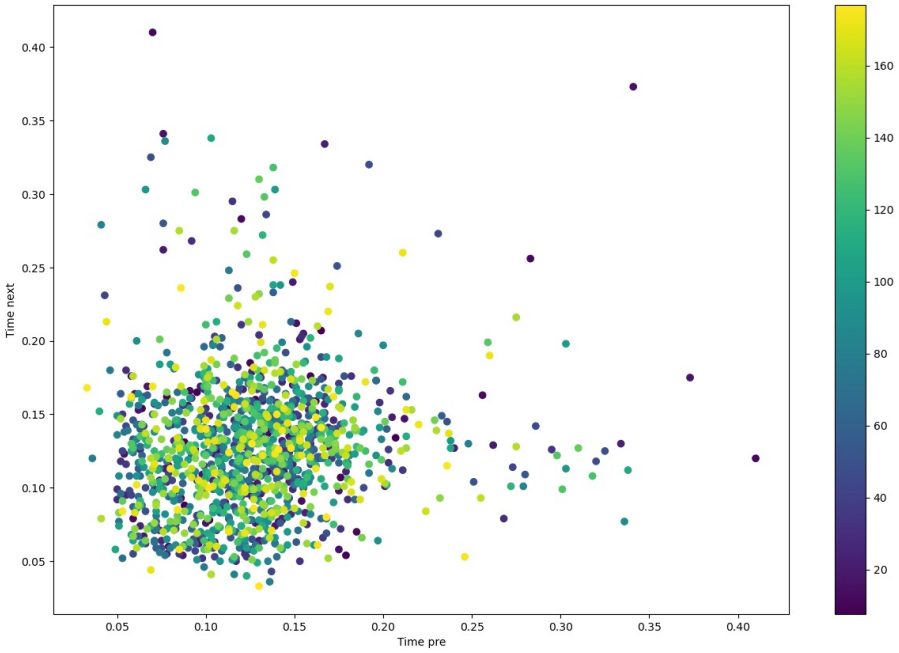

Figure 38: Glass beads experiment with time of pre- and next shear stress drop for velocity 0.064 rpm.

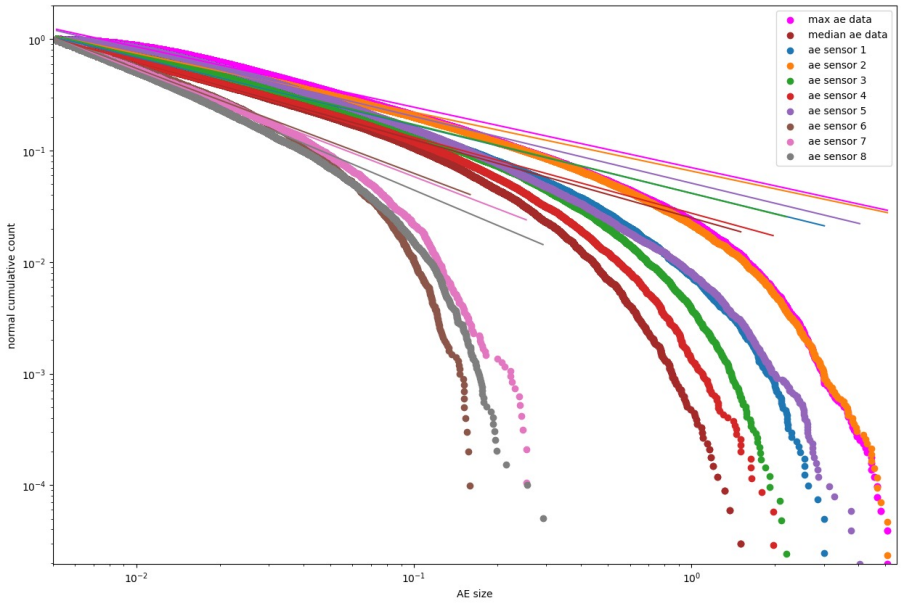

Figure 39: Glass beads experiment with b-value determined for AE data for velocity 0.032 rpm.

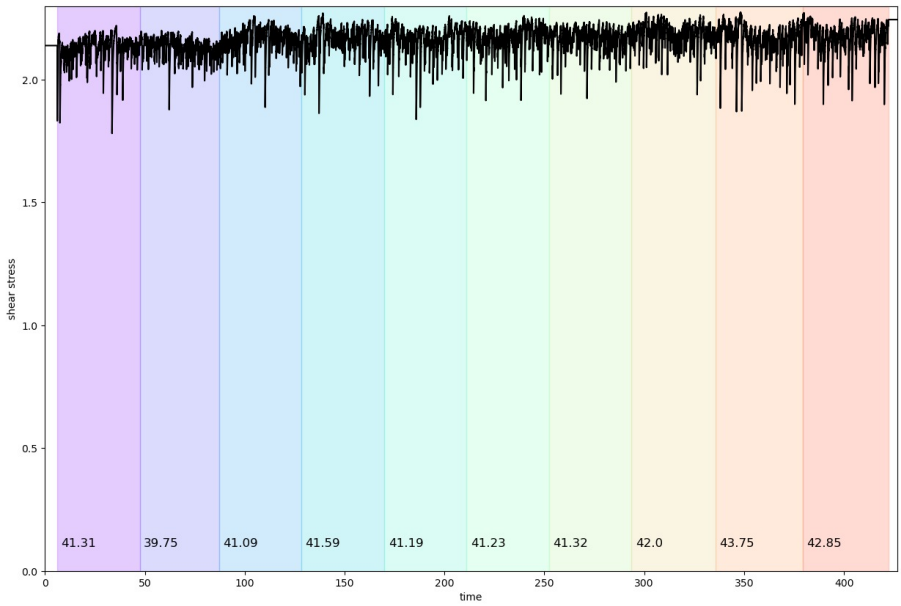

Figure 40: Glass beads experiment with 10% of the recorded acoustic emission data per colored column for velocity 0.008 rpm.

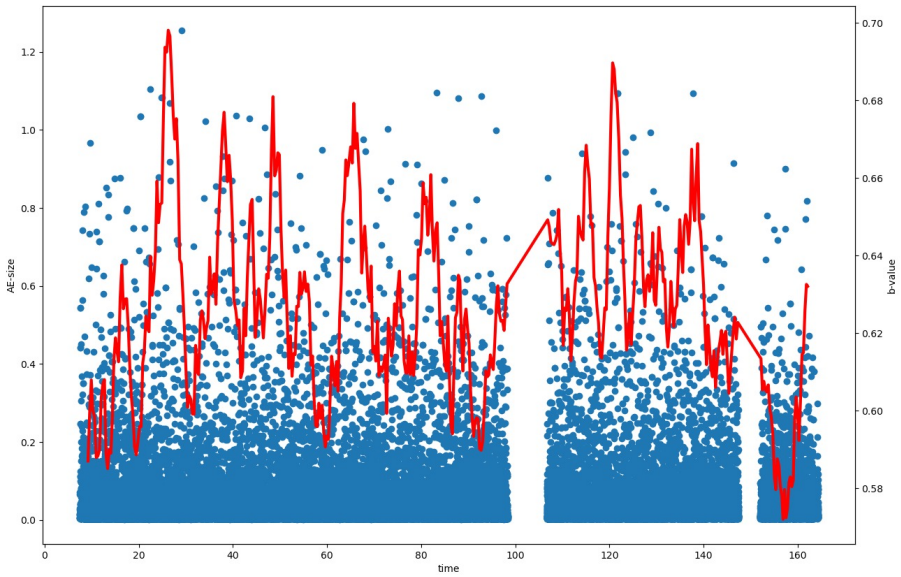

Figure 41: Glass beads experiment with median b-value through time along with median acoustic emissions for velocity 0.064 rpm.

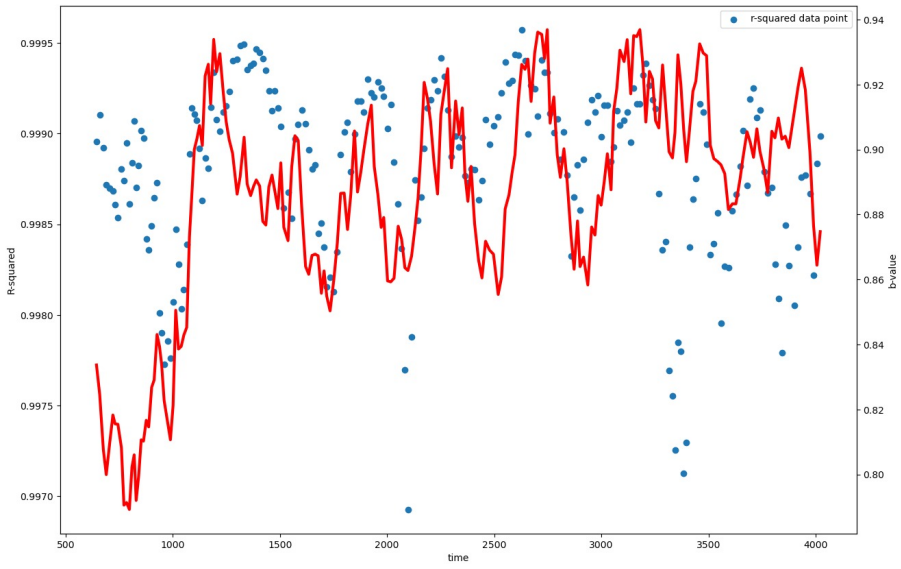

Figure 42: Glass beads experiment with median b-value through time along with R^2 for velocity 0.001 rpm.

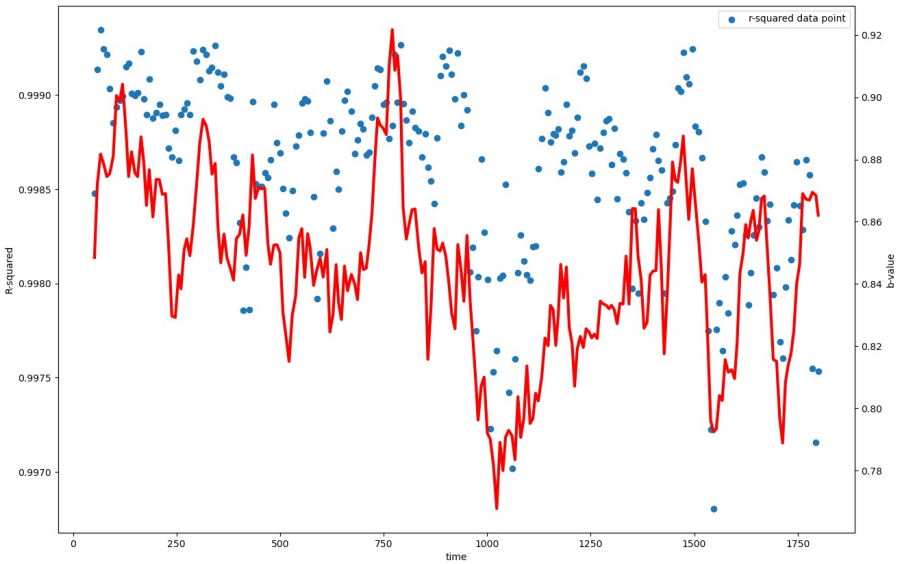

Figure 43: Glass beads experiment with median b-value through time along with R^2 for velocity 0.002 rpm.

9.1.5 Experiment r348

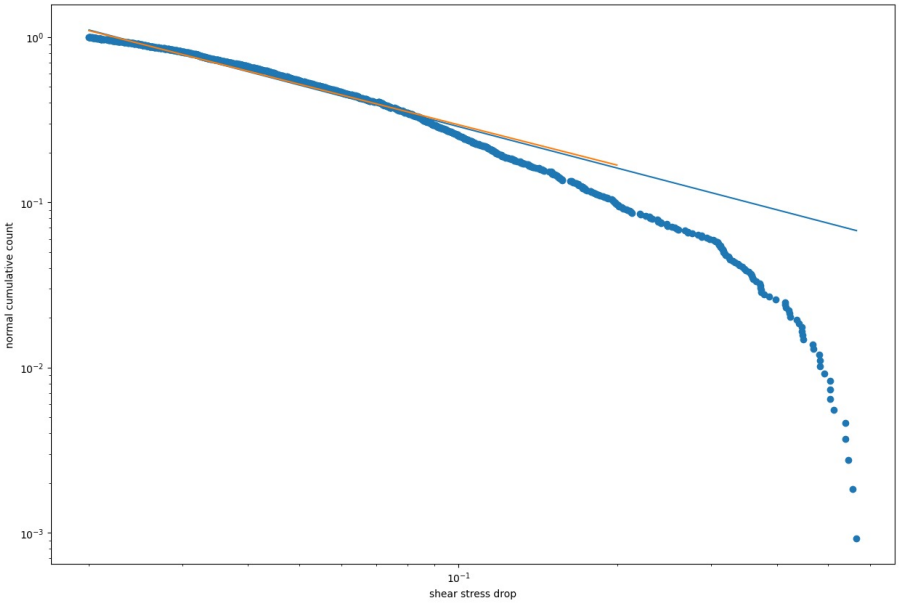

Figure 44: Glass beads experiment with b-value determined for shear stress drop (with (orange) and without (blue) cut-off) data for velocity 0.001 rpm.

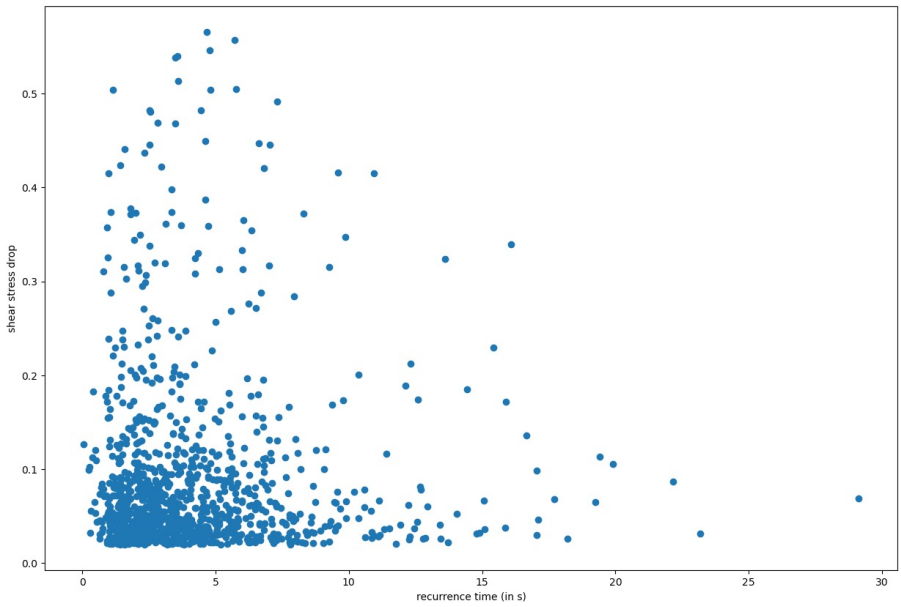

Figure 45: Glass beads experiment with recurrence time for shear stress drops for velocity 0.064 rpm.

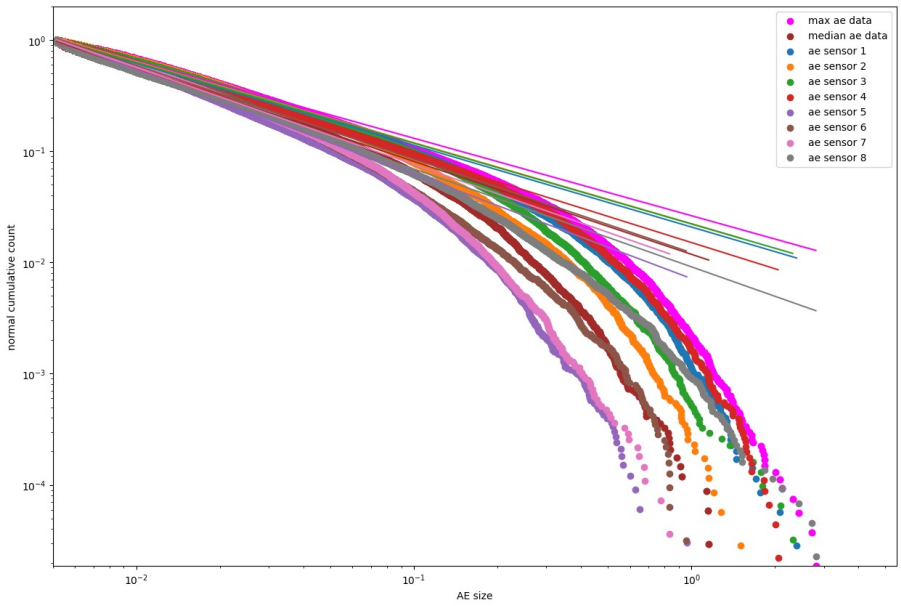

Figure 46: Glass beads experiment with b-value determined for AE data for velocity 0.004 rpm.

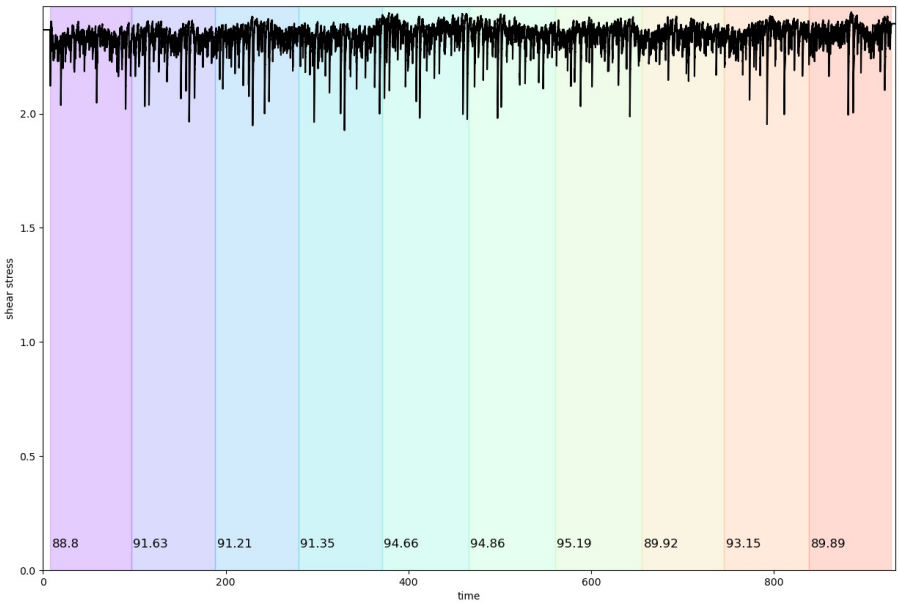

Figure 47: Glass beads experiment with 10% of the recorded acoustic emission data per colored column for velocity 0.004 rpm.

9.1.6 Experiment r353

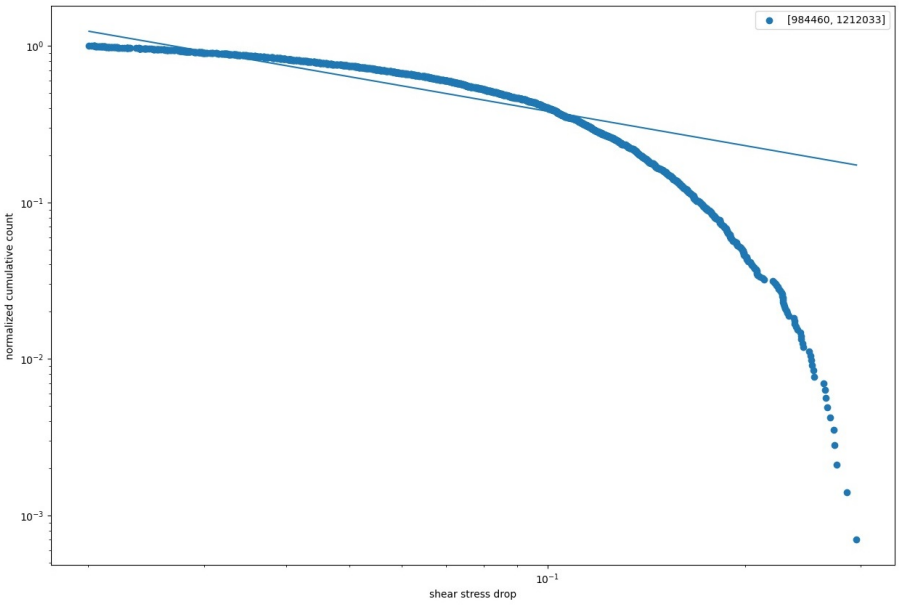

Figure 48: Glass beads experiment with b-value determined for shear stress drop data for velocity 0.064 rpm.

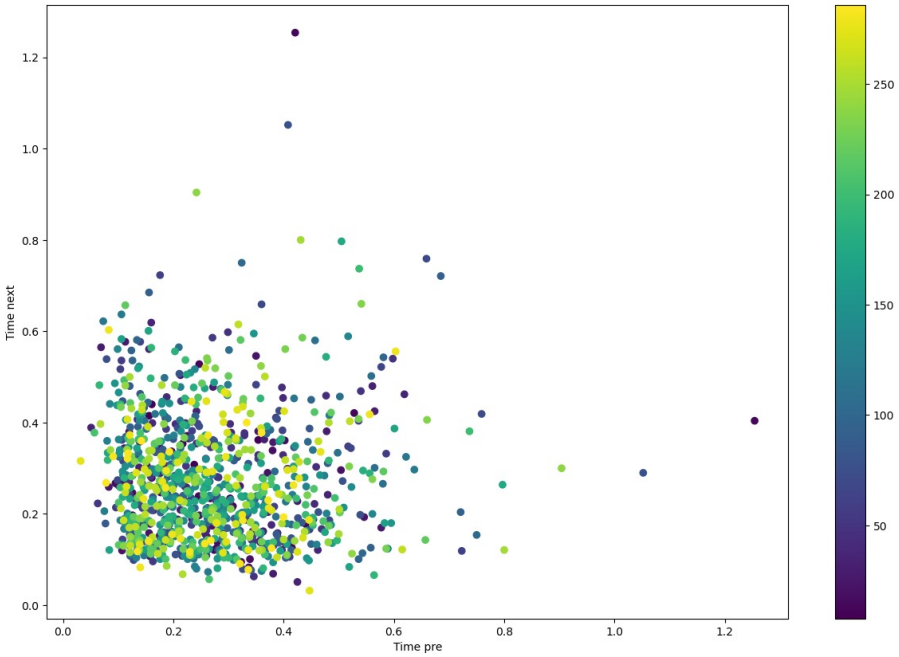

Figure 49: Glass beads experiment with time of pre- and next shear stress drop for velocity 0.032 rpm.

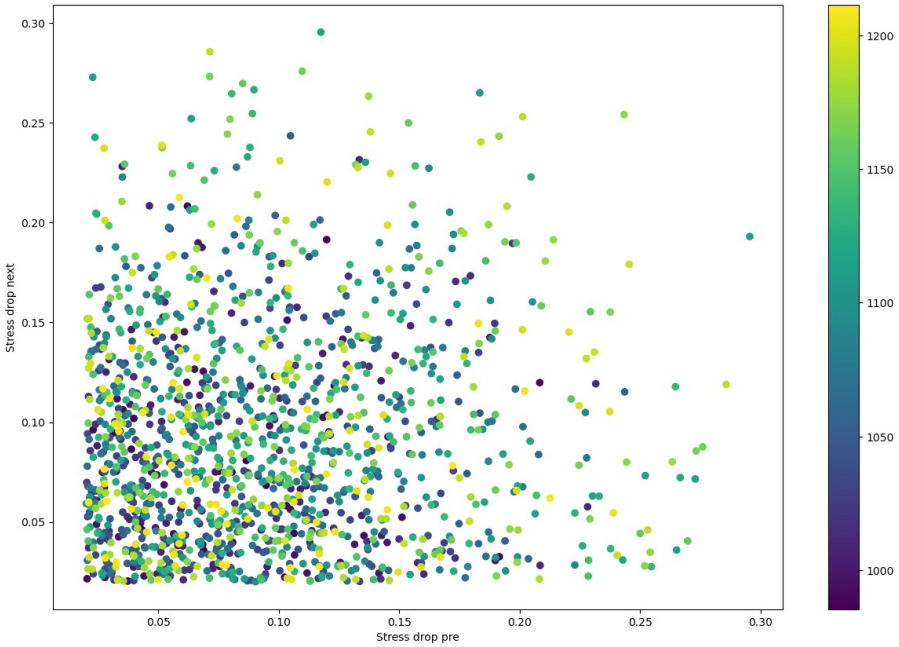

Figure 50: Glass beads experiment with pre- and next shear stress drop for velocity 0.064 rpm.

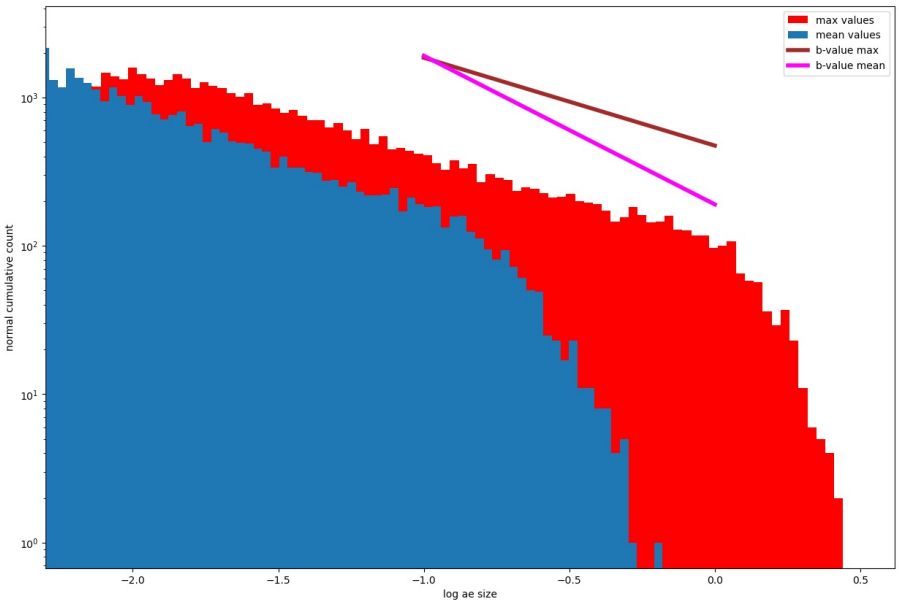

Figure 51: Glass beads experiment with b-value determined for AE data for velocity 0.064 rpm.

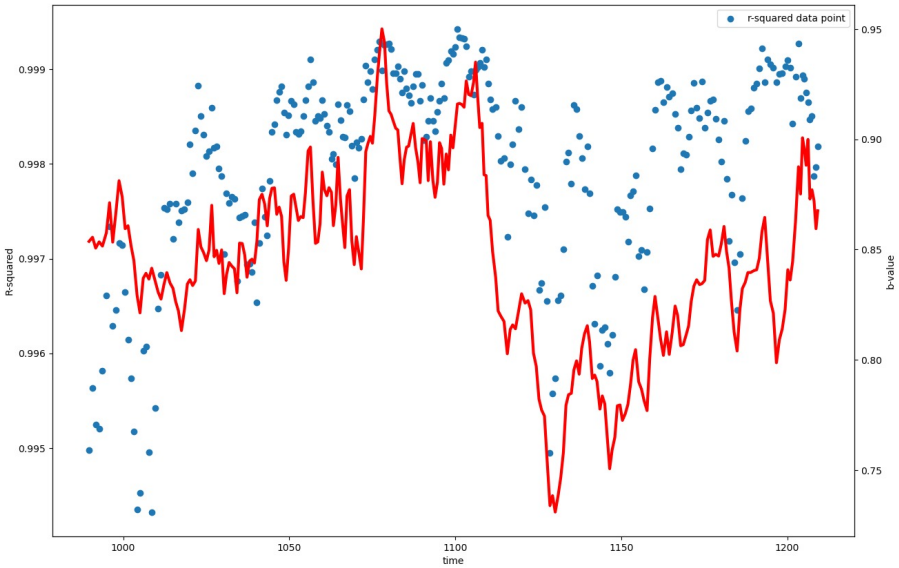

Figure 52: Glass beads experiment with median b-value through time along with R^2 for velocity 0.064 rpm.

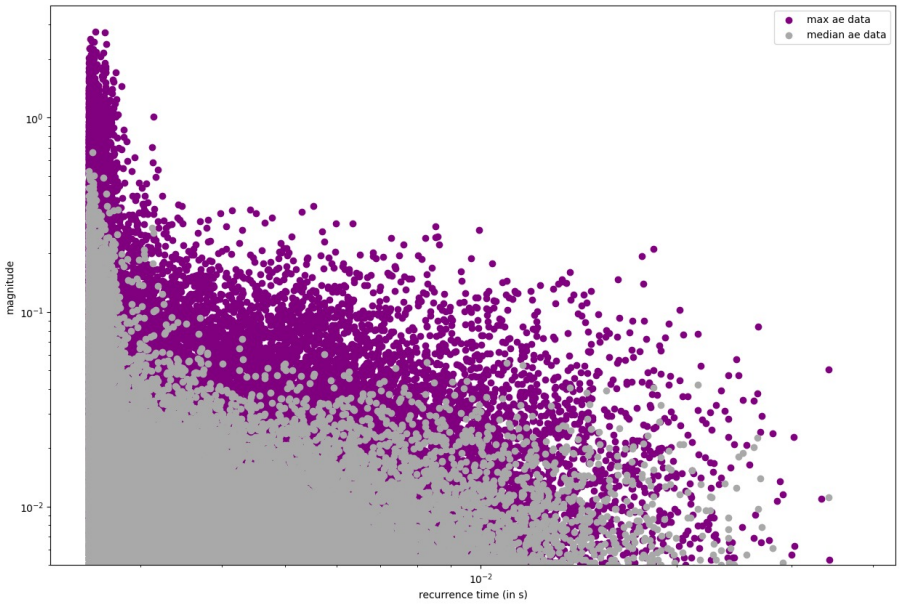

Figure 53: Glass beads experiment with recurrence time of median and maximum AE data for velocity 0.064 rpm.

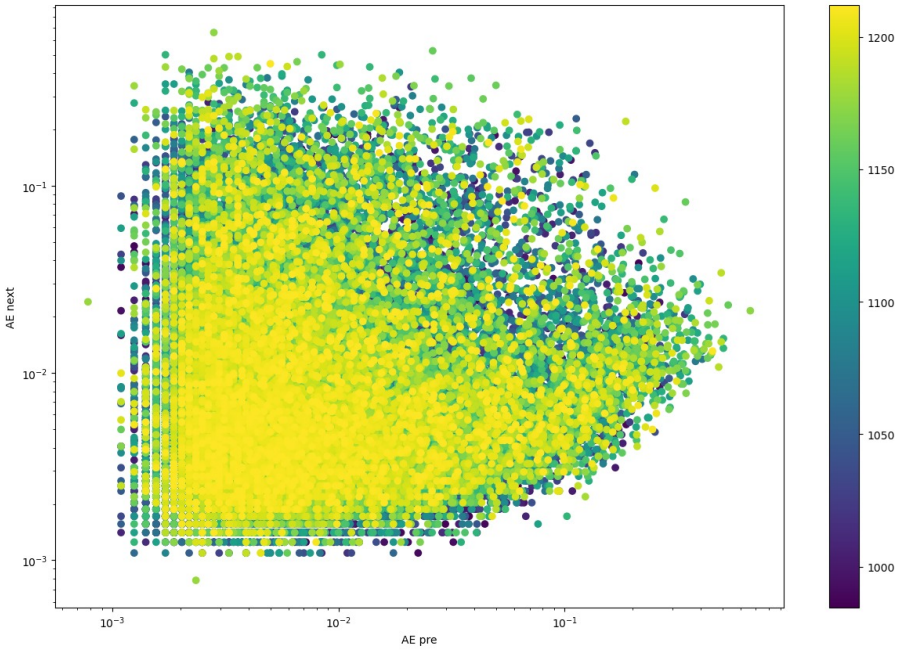

Figure 54: Glass beads experiment with pre- and next acoustic emissions for velocity 0.064 rpm.

9.2 Figures gypsum

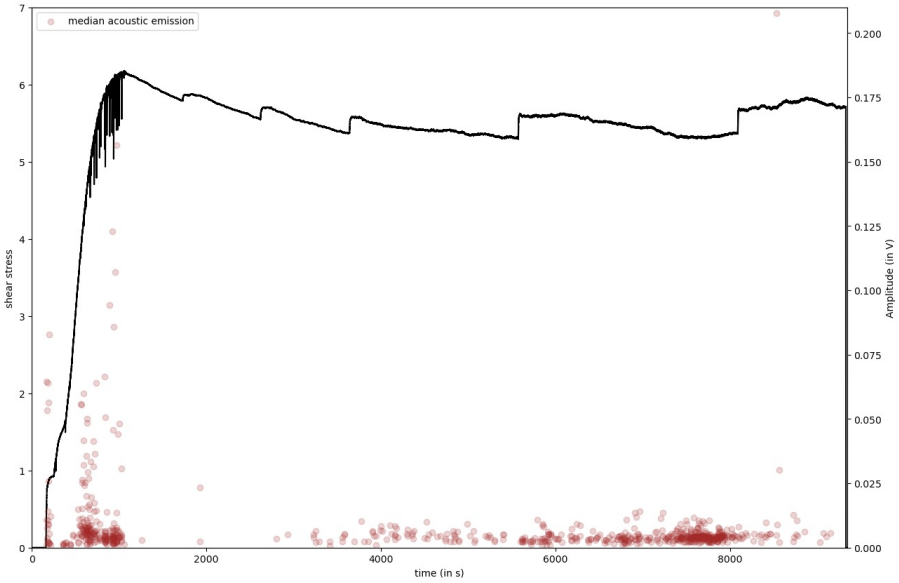

Figure 55: Gypsum experiment with acoustic emissions.

9.3 Figures KCl

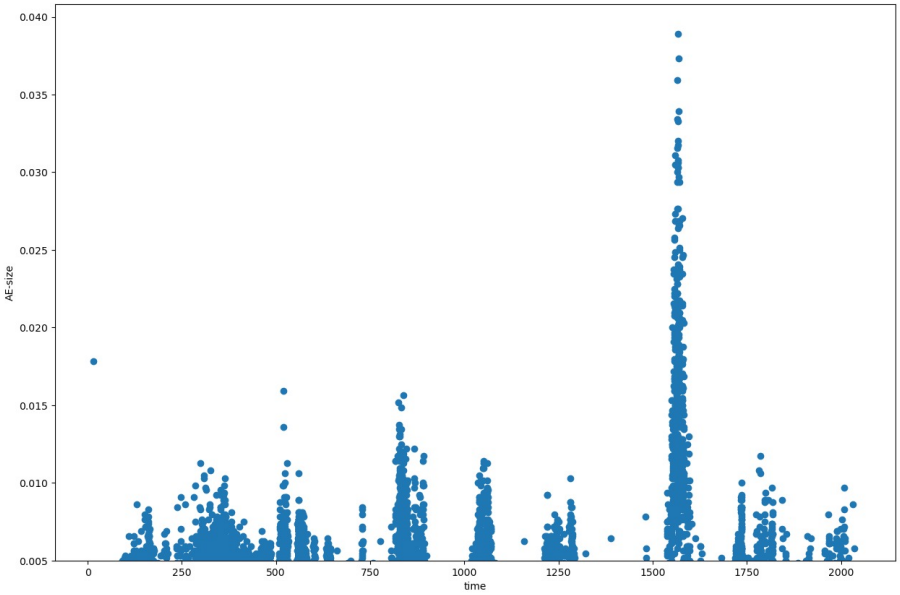

Figure 56: KCl experiment with acoustic emissions for velocity 0.016 rpm.

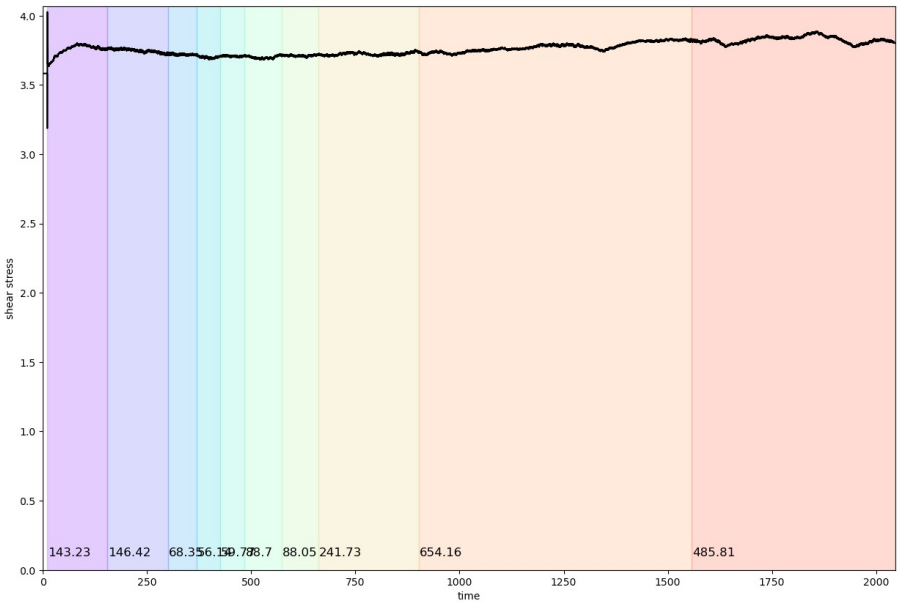

Figure 57: KCl experiment with 10% of the recorded acoustic emission data per colored column for velocity 0.016 rpm.

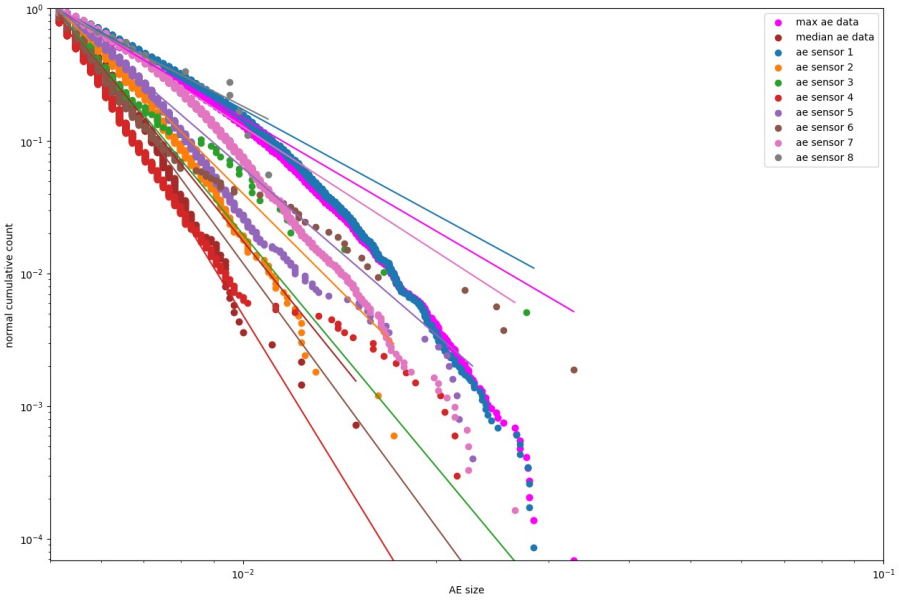

Figure 58: KCl experiment with b-value determined for AE data for velocity 0.032 rpm.

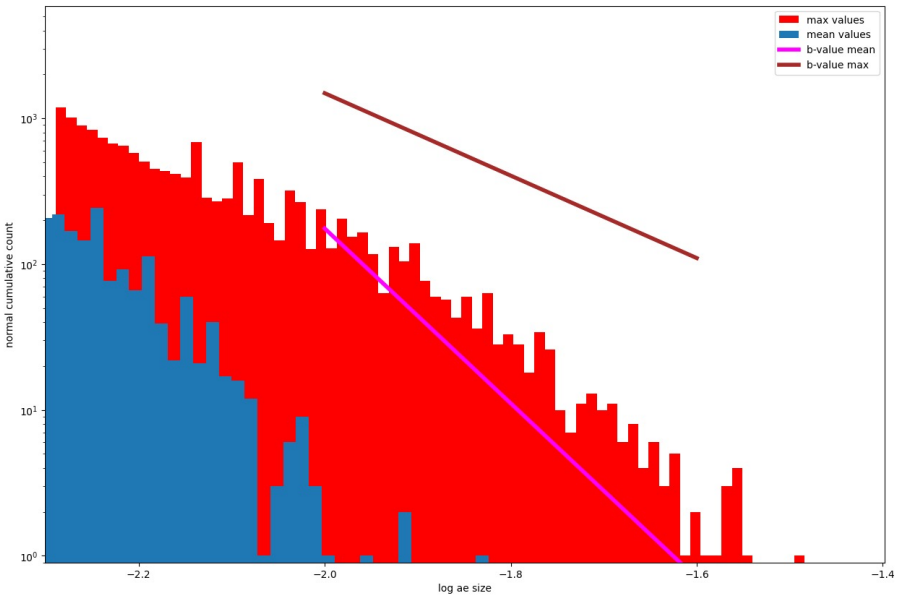

Figure 59: KCl experiment with b-value determined for AE data plotted in histogram for velocity 0.032 rpm.

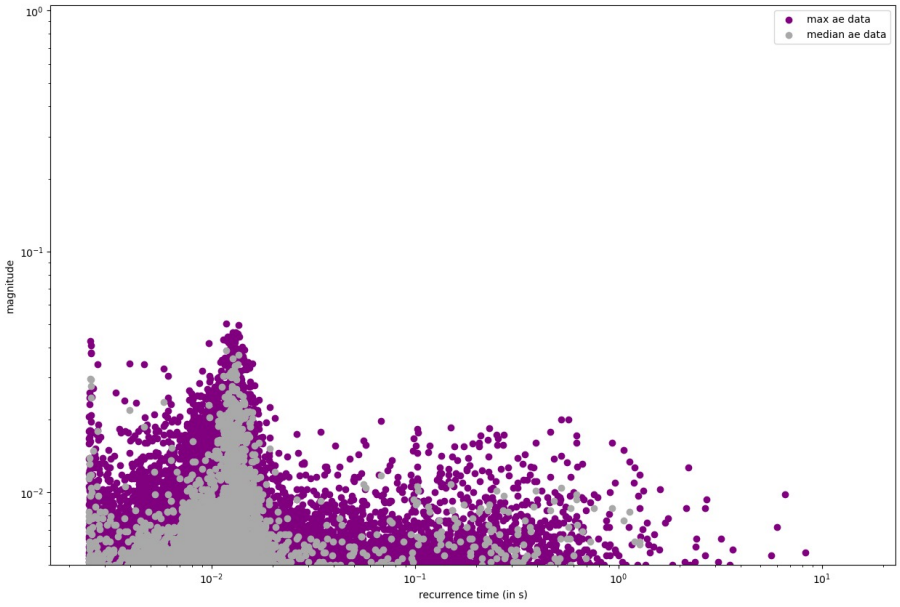

Figure 60: KCl experiment with recurrence time of median and maximum AE data for velocity 0.016 rpm.

9.4 NaCl

9.4.1 Experiment r363

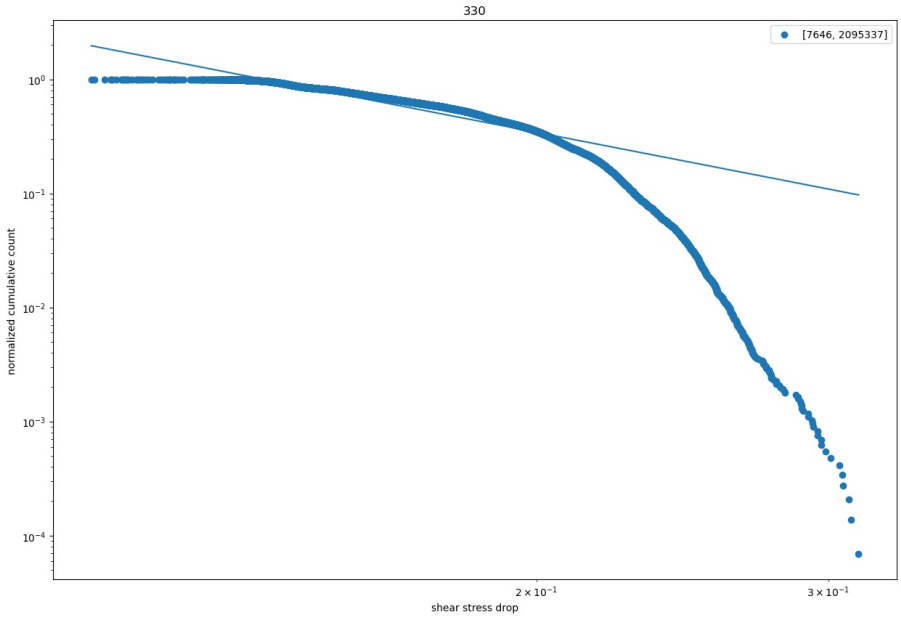

Figure 61: NaCl experiment with b-value determined for shear stress drop data for velocity 0.002 rpm.

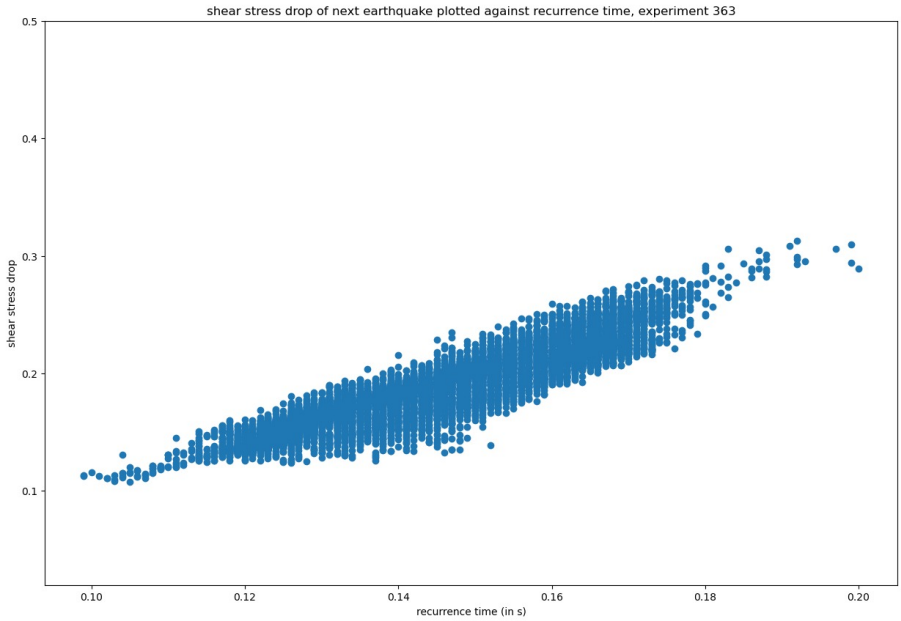

Figure 62: NaCl experiment with recurrence time of shear stress drop data for velocity 0.008 rpm.

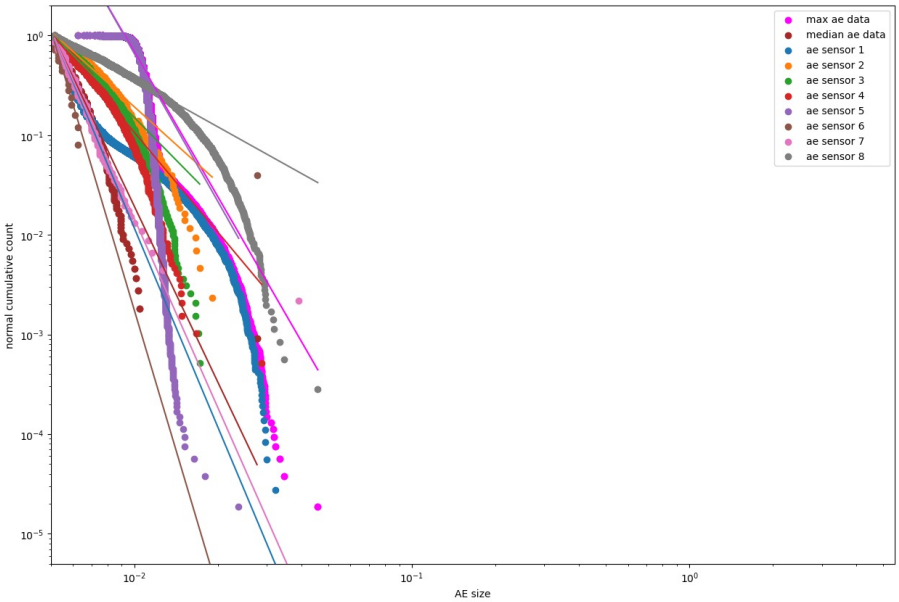

Figure 63: NaCl experiment with b-value determined for acoustic emission data for velocity 0.064 rpm.

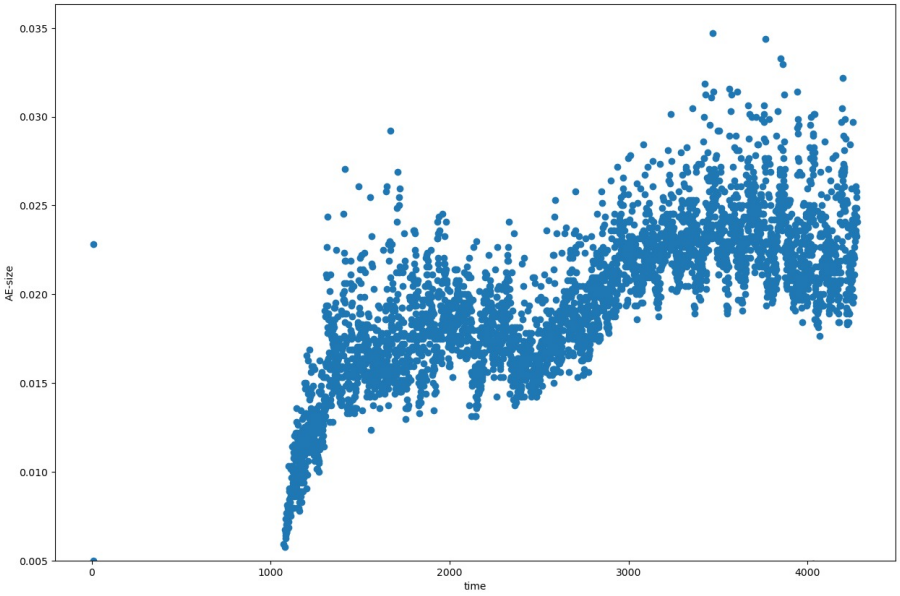

Figure 64: NaCl experiment with median acoustic emissions for velocity 0.004 rpm.

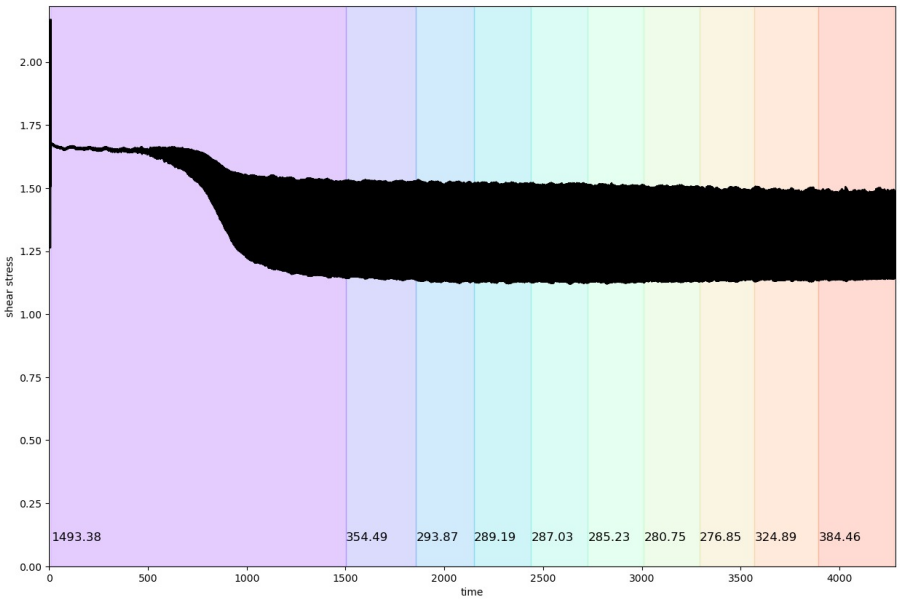

Figure 65: NaCl experiment with 10% of the recorded acoustic emission data per colored column for velocity 0.004 rpm.

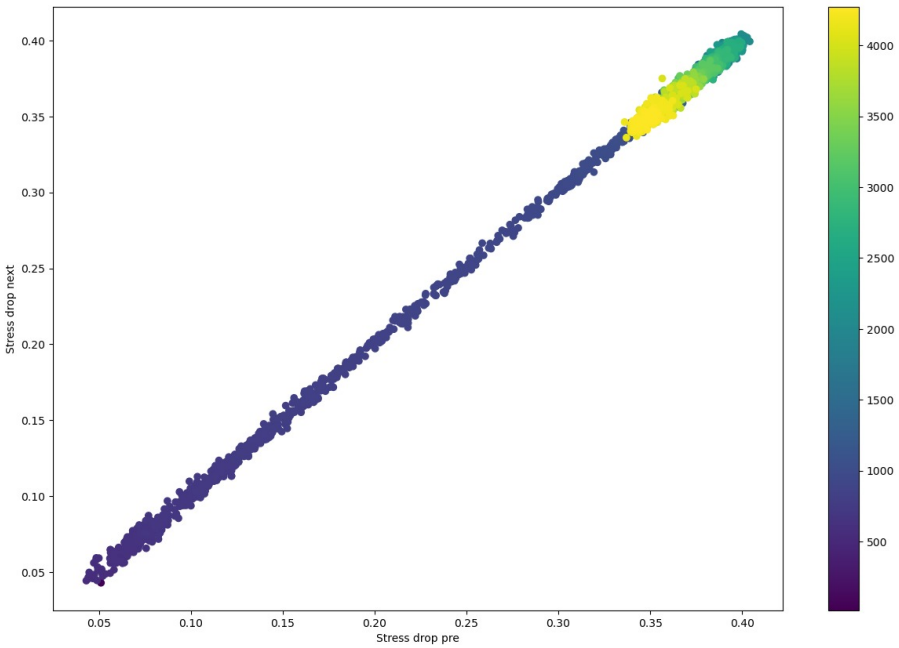

Figure 66: NaCl experiment with pre- and next shear stress drop for velocity 0.064 rpm.

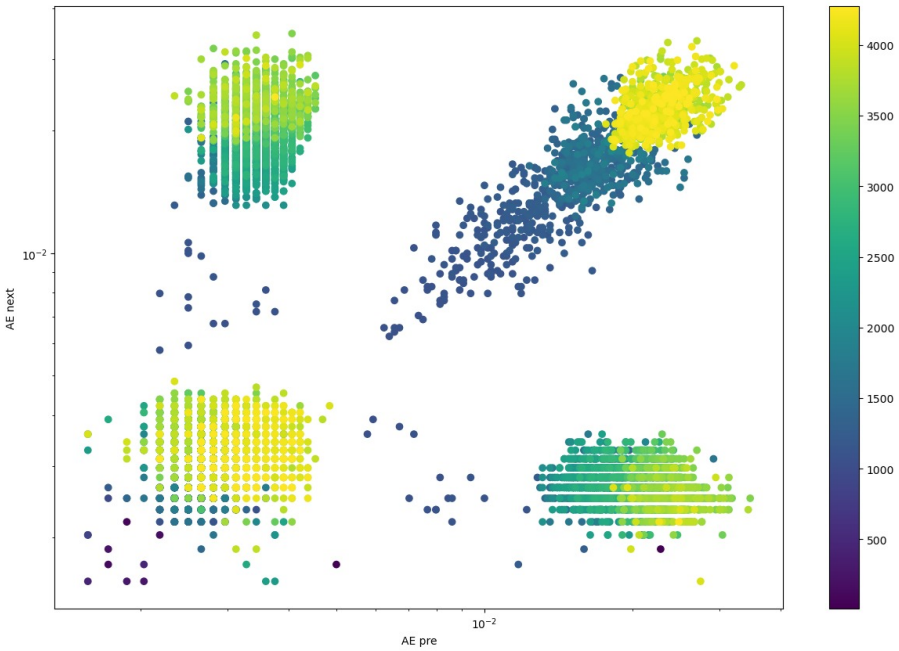

Figure 67: NaCl experiment with pre- and next acoustic emissions for velocity 0.064 rpm.

9.4.2 Experiment r365

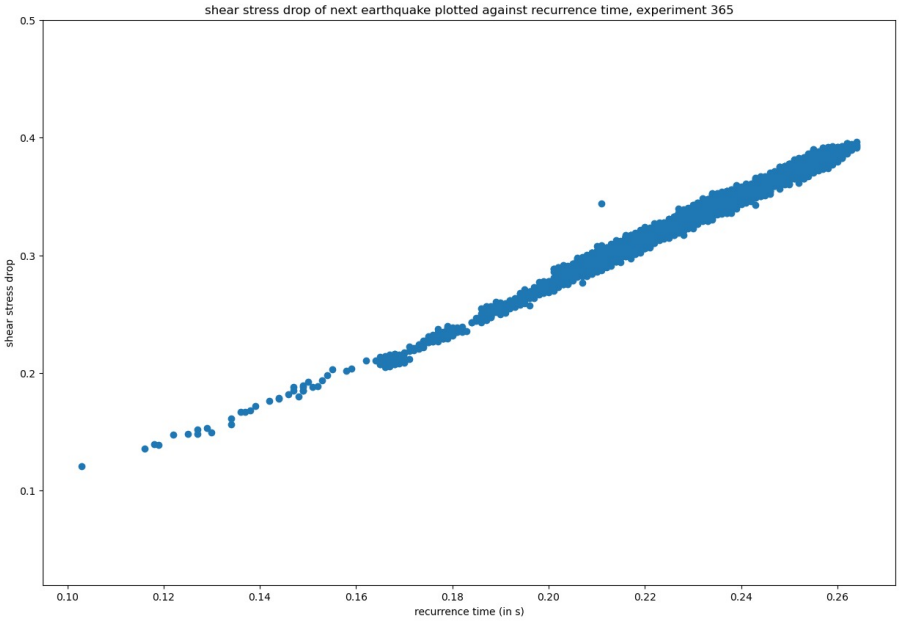

Figure 68: NaCl experiment with recurrence time of shear stress drop data for velocity for velocity 0.008 rpm.

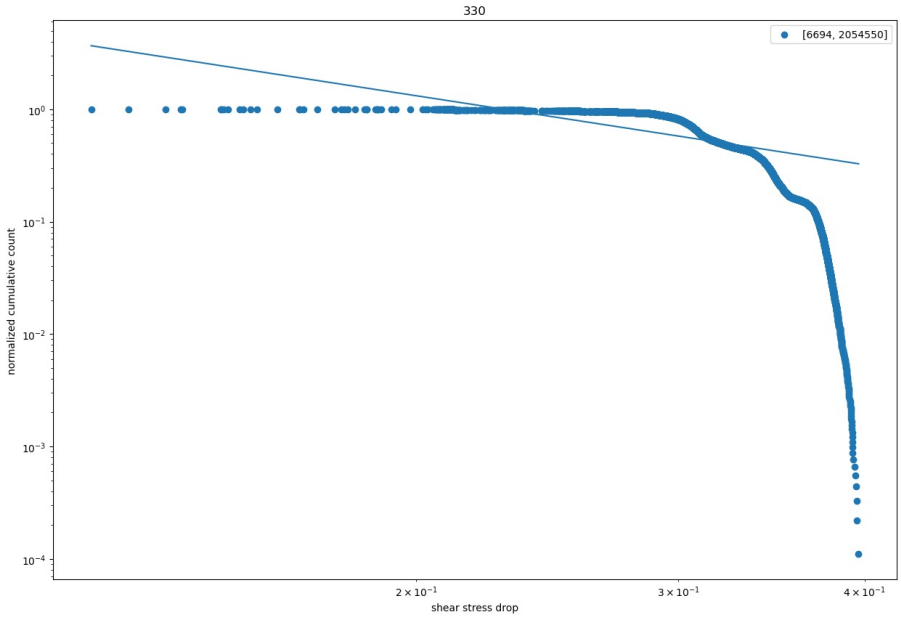

Figure 69: NaCl experiment with b-value determined for shear stress drop data for velocity 0.008 rpm.

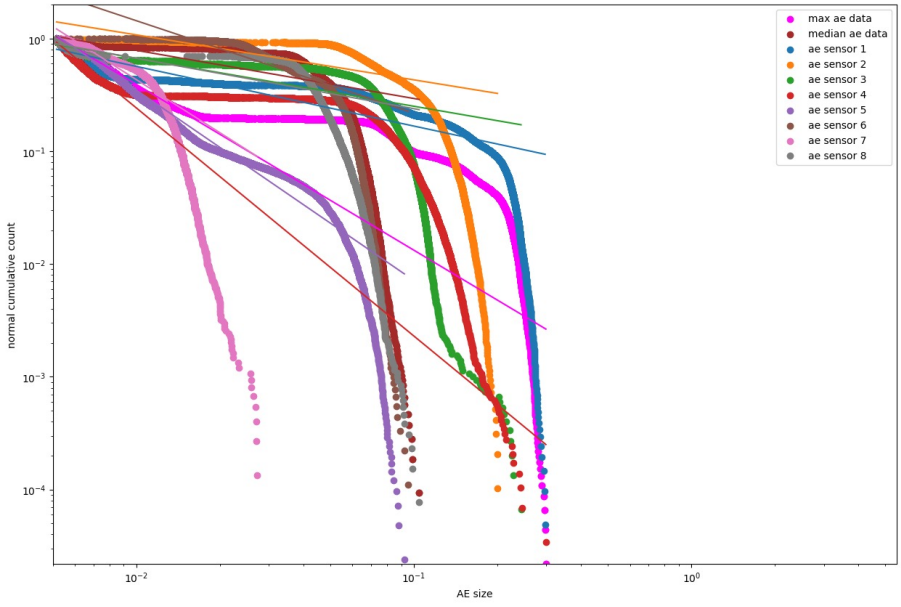

Figure 70: NaCl experiment with b-value determined for acoustic emission data for velocity 0.008 rpm.

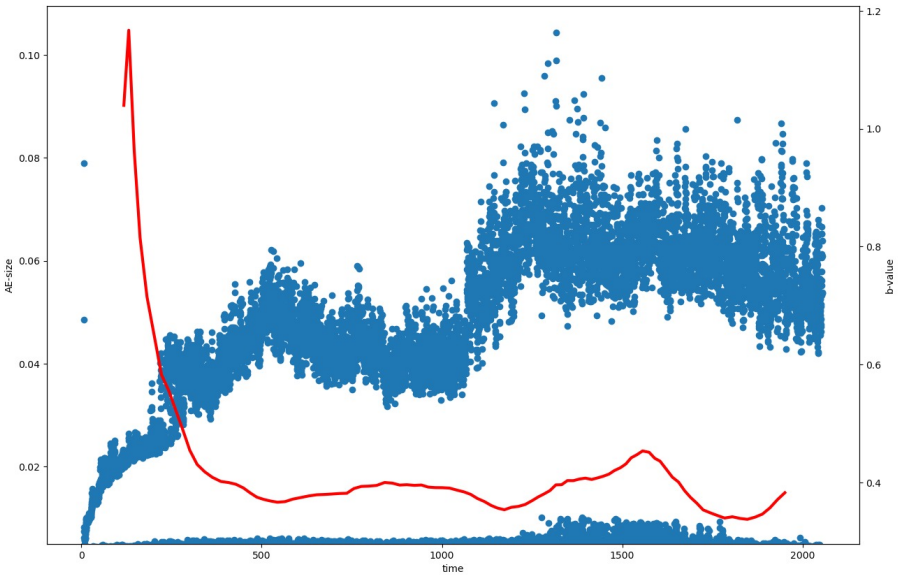

Figure 71: NaCl experiment with median b-value through time along with median acoustic emissions for velocity 0.016 rpm.

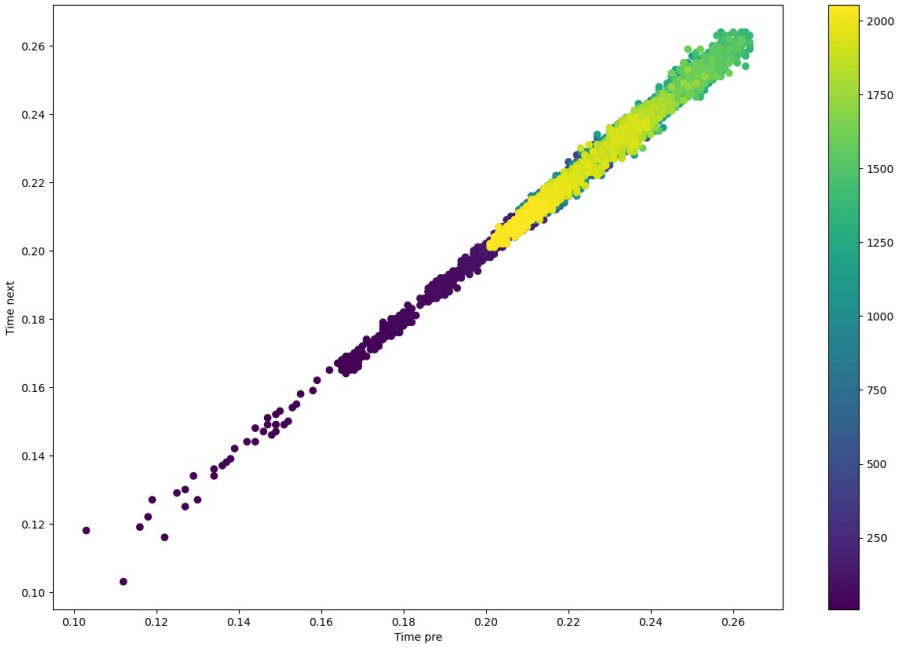

Figure 72: NaCl experiment with pre- and next shear stress drop for velocity 0.008 rpm.

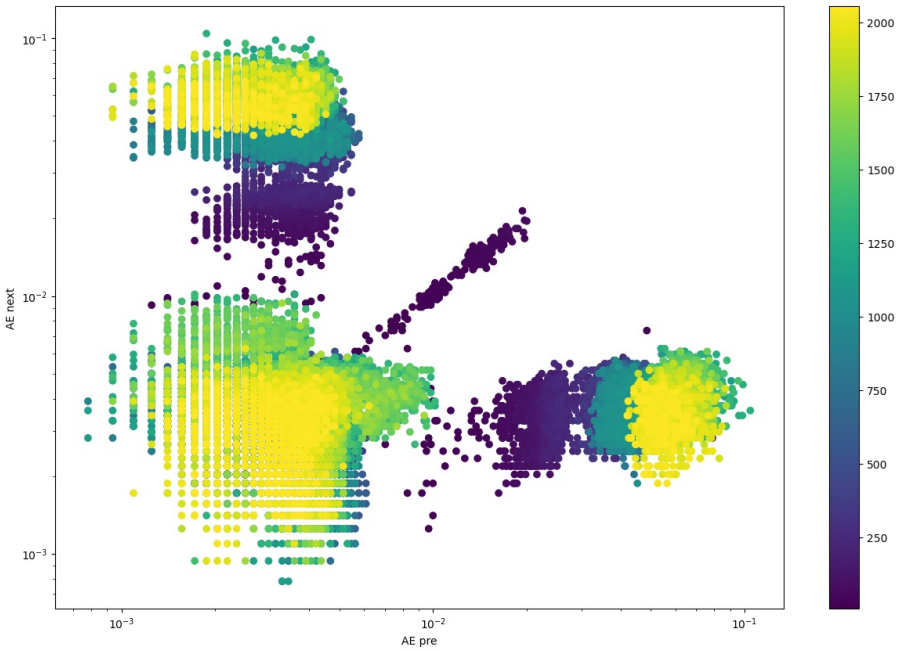

Figure 73: NaCl experiment with pre- and next acoustic emission for velocity 0.008 rpm.